# FABRICATION, CHARACTERIZATION, AND APPLICATION OF MULTIFUNCTIONAL MICROCANTILEVER HEATERS

A Dissertation
Presented to
The Academic Faculty

by

Jungchul Lee

In Partial Fulfillment
of the Requirements for the Degree
of Doctor of Philosophy in the
George W. Woodruff School of Mechanical Engineering

Georgia Institute of Technology
May 2007

# FABRICATION, CHARACTERIZATION, AND APPLICATION OF MULTIFUNCTIONAL MICROCANTILEVER HEATERS

Approved by:


Dr. William P. King, Advisor
George W. Woodruff School of Mechanical Engineering
*Georgia Institute of Technology*

Dr. Mark G. Allen
School of Electrical & Computer Engineering
*Georgia Institute of Technology*

Dr. Yogendra Joshi
George W. Woodruff School of Mechanical Engineering
*Georgia Institute of Technology*

Dr. Oliver Brand
School of Electrical & Computer Engineering
*Georgia Institute of Technology*

Dr. Ari Glezer
George W. Woodruff School of Mechanical Engineering
*Georgia Institute of Technology*


Date Approved: March 28, 2007

# ACKNOWLEDGEMENTS

First of all, I would like to thank my advisor Prof. Bill King for inspiring and encouraging me throughout my PhD studies. Without his support and advice, I would never have been able to have a chance to write this page now. Under his guidance, I could participate in various interesting research projects and was able to meet and collaborate with smart, diligent, and nice people. I would like to thank Prof. Marchenkov at GT Physics for helping me finish microcantilever measurements in vacuum. I am also very grateful to Dr. Graham for his help on Raman spectroscopy. They were very supportive to my work and let me have access to their laboratory day and night. I would like to thank to Dr. Thundat at ORNL for giving an idea to make a new type of microcantilever hotplate. When Bill and I visited ORNL, we had fruitful discussions which turned into a chapter of my thesis. Last fall, Bill arranged a meeting with Dr. Chui who has done early work on microcantilever heater devices. It was such a great chance to meet him since my research has been influenced by him and his collaborator at CSEM, Switzerland.

I am also very grateful to all committee members who have kindly accepted to review my dissertation. Prof. Glezer has been supportive for micro/nanojet research, Prof. Joshi and Prof. Allen always tried to give me an insight to look and think deeper, and Prof. Brand went through all of my manuscripts carefully. I was truly blessed to interact with the best academic committee. I wish to express my sincere thanks to Linda Perry, Terri Keita, and Glenda Johnson who have done great administrative work to support all ME students at GT.

My special thanks go to present and past NTPL group members: Brent, Joe, Harry, Fabian, Marcus, Andrew Cannon, Shubham, Jessica, Andrew Garner, Fuzheng, KJ, Keunhan, and Tanya. They have always supported my work and life here at GT, made the atmosphere enjoyable at all times, treated me like family. My gratitude also goes to all Korean student association ME members at GT. Especially, Dr. Shin always helped me regarding any fabrication issues in the MiRC cleanroom. Keunhan and BJ were eager to discuss any interesting question. Dr. Sangil Lee, Dr. Hyunjin Lee, Hoy, Namsu, and Minseok were nice and kind to share their valuable time to relax our tired bodies and minds. Additional thanks go to Hanif, John, Nisarga and Kianoush. I have got great help from them for the nanojet project.

Finally, my best thanks and appreciation go to my family. My father, mother, sister have never stopped praying for my academic success and health. I am truly blessed by them. I wish to express my sincere thanks to my wife, JuHee. She has been sacrificing her health, time and career to support my PhD degree. During my PhD studies, we have been blessed by two babies, Kevin and Ryan. JuHee also took best care of them while supporting me. Her sacrifice may not be tangible but I could feel and see on every page in my dissertation. All my family has been supporting me with kindness and patience throughout my PhD studies. Now it is my turn to support and take care of my wife, my sons, and my parents.

# TABLE OF CONTENTS

# LIST OF TABLES

**Page**

# LIST OF FIGURES

**Page**

# LIST OF SYMBOLS

| | |
|---|---|
| $A_{jet}$ | cross-sectional area of the jet. |
| $B$ | coefficient for temperature dependent elastic modulus |
| $C_i$ | intrinsic vacancy density |
| $C_m$ | mass correction factor for resonance frequency calculation |
| $C_V$ | vacancy density |
| $c_{piezo}$ | bridge voltage offset at $T_c$ |
| $D$ | diffusion coefficient or diffusivity |
| $D_N$ | extrinsic diffusivity of n-type dopant |
| $D_P$ | extrinsic diffusivity of p-type dopant |
| $D^0$ | neutral component in extrinsic diffusion |
| $D^-$ | negative component in extrinsic diffusion |
| $D^+$ | positive component in extrinsic diffusion |
| $D^{--}$ | double-negative component in extrinsic diffusion |
| $D^{++}$ | double-positive component in extrinsic diffusion |
| $d$ | distance from the clamped base to the center of the jet |
| $d_g$ | effective diameter of the gas molecule |
| $d_{separation}$ | separation distance between the cantilever and the nozzle |
| $E$ | elastic modulus |
| $E_0$ | elastic modulus at 0 K |
| $E_a$ | activation energy |
| $E_i$ | intrinsic Fermi level |
| $E_F$ | Fermi level |
| $F$ | diffusive flux |
| $F_{jet}$ | jet thrust |
| $f_c$ | resonant frequency of a clean cantilever |

| | |
|---|---|
| $f_m$ | resonant frequency of a cantilever with adsorbed mass |
| $f_n (n = 0,1,2,\cdots)$ | fundamental resonance frequency and higher overtone |
| $k$ | spring constant |
| $k_B$ | Boltzmann's constant |
| $L$ | cantilever length |
| $l$ | characteristic length |
| $m$ | total mass of the cantilever |
| $m_{eff}$ | effective mass of a microcantilever for a simple harmonic oscillator model |
| $N$ | electron concentration |
| $N_d$ | dopant distribution |
| $N_{max}$ | maximum local doping concentration |
| $P$ | hole concentration |
| $P_{crit}$ | critical power |
| $P_g$ | gas pressure |
| $Q$ | implanted dose |
| $Q_n (n = 0,1,2,\cdots)$ | quality factors corresponding to resonance frequencies |
| $R$ | electrical resistance |
| $R_p$ | average implant depth |
| $R_{Peak}$ | peak electrical resistance of the doped silicon microcantilever |
| $R_s$ | steady resistance |
| $r_{jet}$ | radius of effective flow field of the jet |
| $r_{nozzle}$ | radius of the microfabricated nozzle |
| $S_T$ | temperature sensitivity |
| $S_\delta$ | deflection sensitivity |
| $T$ | diffusion temperature |
| $T_0$ | ambient temperature |

| | |
|---|---|
| $T_c$ | temperature at $\partial V_{piezo}/\partial T=0$ |
| $T_{cant}$ | cantilever temperature |
| $T_{crit}$ | critical temperature |
| $T_{FWHM}$ | temperature from Raman spectroscopy based on FWHM |
| $T_g$ | gas temperature |
| $T_H$ | cantilever heater temperature |
| $T_{max}$ | maximum temperature |
| $T_{Peak}$ | temperature from Raman spectroscopy based on Stokes peak |
| $T_s$ | temperature of the heater surface |
| $T_{sat}$ | saturation temperature |
| $T_{sur}$ | effective temperature of surroundings |
| $\overline{T}$ | integral-average temperature based on the bending stress |
| $t$ | cantilever thickness |
| V | cantilever volume |
| $V_{high}$ | high voltage level for the transient |
| $V_{jet}$ | jet velocity |
| $V_{low}$ | low voltage level of the applied square pulse |
| $V_{Peak}$ | voltage corresponding to the peak resistance |
| $V_{piezo}$ | voltage from the Wheatstone bridge with a piezoresistive cantilever |
| $V_{sense}$ | voltage drop across the sense resistor |
| $V_{total}$ | voltage input to the half bridge for the heated cantilever |
| $X$ | reactance |
| $\langle x^2 \rangle$ | mean square deflection of the cantilever |
| | |
| $\alpha$ | thermal diffusivity |
| $\beta$ | change of the Stokes peak position as a function of temperature |

| | |
|---|---|
| $\gamma$ | slope of the calibrated Stokes peak position as a function of stress |
| $\delta$ | cantilever deflection |
| $\delta m$ | absorbed / desorbed mass |
| $\Delta R$ | resistance oscillation amplitude |
| $\Delta R_p$ | average variation in implant depth |
| $\Delta T$ | excess temperature |
| $\theta_{spray}$ | the spray angle of the gaseous nitrogen jet |
| $\Lambda$ | energy carrier mean free path |
| $\mu_b$ | bulk mobility |
| $\rho$ | mass density |
| $\rho_{jet}$ | density of the jet |
| $\sigma$ | stress |
| $\tau$ | thermal time constant |
| $\tau_c$ | cooling time constant |
| $\tau_h$ | heating time constant |
| $\omega$ | frequency |
| $\varpi$ | resonant frequency of an unloaded rectangular beam |

| | |
|---|---|
| AC | alternating current |
| AFM | atomic force microscopy (microscope) |
| ATM | atmospheric pressure |
| CCD | charge-coupled device |
| CD-ROM | compact disc read-only memory |
| CHF | critical heat flux |
| CMOS | complementary metal oxide semiconductor |
| CNTs | carbon nanotubes |

| | |
|---|---|
| CVD | chemical vapor deposition |
| DC | direct current |
| DNA | deoxyribonucleic acid |
| DPN | dip-pen nanolithography |
| DVD | digital versatile disc |
| FCs | fluorocarbons |
| FPN | fountain pen nanolithography |
| FWHM | full width at half maximum |
| HFEs | hydrofluoroethers |
| HWA | hot-wire anemometry |
| ICP | inductively coupled plasma |
| IR | infrared |
| *Kn* | Knudsen number |
| MEMS | microeletromechanical systems |
| NADIS | nanoscale dispensing |
| ND:YAG | Neodymium-doped Yttrium Aluminum Garnet ($Nd:Y_3Al_5O_{12}$) |
| PCB | printed circuit board |
| PECVD | plasma enhanced chemical vapor deposition |
| PID | proportional-integral-differential |
| PIV | particle image velocimetry |
| PSD | power spectrum density |
| PVDF | Polyvinylidene Fluoride |
| PZT | Lead Zirconate Titanate |

| | |
|---|---|
| *Re* | Reynolds number |
| RF | radio frequency |
| RTP | rapid thermal processing |
| SEM | scanning electron microscope (micrograph) |
| SNR | signal to noise ratio |
| SOI | silicon-on-insulator |
| SPL | scanning probe lithography |
| SPM | scanning probe microscopy |
| TCR | temperature coefficient of electrical resistance |
| tDPN | thermal dip pen nanolithography |
| UHV | ultra high vacuum |
| VCSELs | vertical cavity surface emitting lasers |
| ZnO | Zinc oxide |

# SUMMARY

This research aims to fabricate and characterize microcantilever sensors with integrated heaters and construct novel metrology tools using the optimized and well-characterized microcantilevers. This research focuses on fabrication and characterization of multifunctional microcantilever heaters to realize possible applications such as micro hotplates, bio/chemical sensor platforms, and parallel nanoscale lithography and scanning tools.

The first objective seeks to understand thermal, electrical, and mechanical characteristics of microcantilever heaters in various conditions. Experiments investigate thermal, mechanical, and coupled behaviors of the microcantilever heaters under DC, AC, and transient electrical heating. Raman spectroscopy measures local temperature and qualitative intrinsic stress with high spatial resolution. Based on the thorough understanding from device characterization, cantilever type micro hotplates and small array of microcantilever heaters with integrated piezoresistive sensors are fabricated and characterized.

The second objective is to construct novel metrology tools using fabricated and well characterized microcantilever sensors. Heated microcantilevers are suggested to study sub-continuum heat transfer from micro heater to ambient gas environment in a wide range of pressure. Microcantilever sensors are introduced to the free microjets generated from microfabricated nozzles. Piezoresistive microcantilevers measure jet thrust, velocity, and break-up distance of the liquid microjets and microcantilevers heaters investigate heat transfer characteristics and phase change phenomena during microjet impingement.

Overall, this research seeks to impact the engineering community working on microcantilever sensor/metrology by suggesting new characterization techniques and applications.

# CHAPTER 1

# INTRODUCTION

## 1.1 Microcantilever Sensors

The microcantilever is perhaps the most widely used microelectromechanical systems (MEMS) device. Scanning Probe Microscopy (SPM) uses a microcantilever as a stylus to scan a surface with sub-nm resolution. One of the famous families of SPM is Atomic Force Microscopy (AFM) [1]. To obtain surface topography using a microcantilever with an atomically sharp tip, a vertical piezoelectric actuator under the substrate keeps constant contact force between the cantilever and the substrate (Contact mode) or oscillating amplitude of the cantilever (Tapping mode) using an appropriate feedback mechanism. Cantilever deflection used as a set point for the feedback loop can be obtained using various sensing mechanisms such as optical sensing [2,3], piezoresistive sensing [4,5], capacitive sensing [6], and thermal sensing [7,8]. A number of microscopy systems shown in Figure 1.1 have been developed based on AFM.

Besides SPM applications, microfabricated cantilevers have been employed for acceleration sensing [9], radio frequency (RF) MEMS switches [10], bio/chemical detection [11-14], thermomechanical data storage [7,8], nanomaterial synthesis [15], and nanoscale lithography tools [16,17]. To incorporate special functionality into a microfabricated cantilever, some modifications are required during or after fabrication. Well known examples include cantilevers having resistive heaters [18], cantilevers

having a piezoresistive strain gauge [4], and cantilevers having a piezoelectric actuator [19].

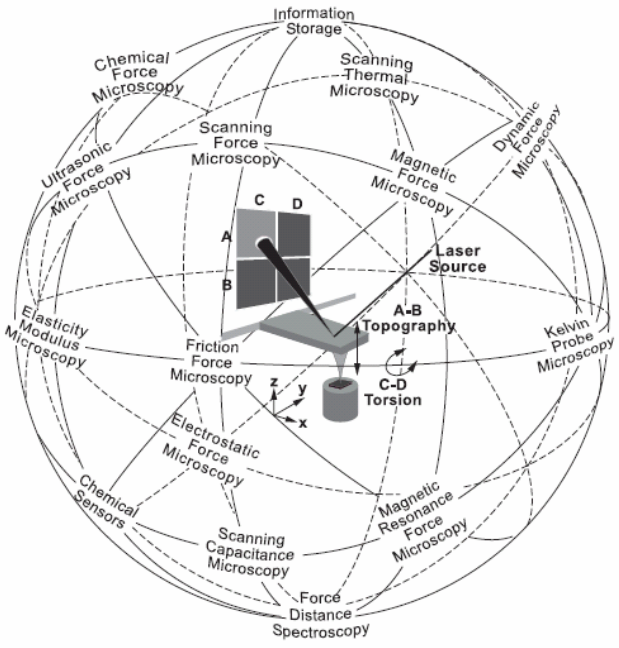


Figure 1.1 The universe of AFM-based microscopy and local sensor techniques [20].

For thermomechanical data storage, a microcantilever was introduced to make nanoscale indents on a recordable media using laser to heat the cantilever tip [21]. This thermomechanical data bit formation was a slow process by nature (order of ~ 1μs) such that thermomechanical data storage needed to be arrayed to compete with their counterparts such as magnetic or optical data storages. Heated cantilevers were fabricated [18] having a solid-state heater near the tip which can inject thermal energy into a polymer substrate. The integrated heater can also act as a resistive thermometer to sense previously written indents [22]. Recently, these heated cantilevers have shown additional usefulness beyond thermomechanical data storage such as nanoscale manufacturing [17] and metrology tools [23].

AFM cantilevers with integrated piezoresistive elements have been developed to replace the optical deflection sensing which uses laser and position sensitive diodes [4]. Implanted piezoresistive elements show the resistance changes while the cantilever experiences mechanical strain. The beauty of these cantilevers is their compactness and readiness to be easily arrayed, and interfaced with harsh or unusual environments such as high temperature and low pressure where optical sensing is not readily accessible. They are also suggested as a sensor platform for applications such as gas flow sensors [24], acceleration sensors [25], and bio/chemical sensors [26].

Microcantilevers with piezoelectric actuators were proposed to actuate the microcantilever instead of using the bulky piezotube. High speed imaging was realized using a piezoelectric microcantilever since the microfabricated cantilever has much higher resonance frequency / wider imaging bandwidth than the piezotube [19]. Piezoelectric microcantilevers are also parallelized and introduced in a probe based data storage application [27]. Piezoelectric devices are characterized by low power consumption and both actuation and sensing capability such that piezoelectric cantilevers are applicable in a variety of fields. Unfortunately, silicon is not a piezoelectric material and there are only a few piezoelectric materials such as lead zirconate titanate (PZT), zinc oxide (ZnO), and polyvinylidene fluoride (PVDF). Moreover, applicable piezoelectric materials are not complementary metal-oxide-semiconductor (CMOS) compatible and fabrication processes are also complicated.

## 1.2 Microcantilever Applications

### 1.2.1 Thermomechanical data storage

Parallel to the development of information technologies, there has been strict demand for the performance and capacity of data storage devices. There is the well-known super-paramagnetic limit [28] in magnetic data storage. Optical data storages such as CD-ROM and DVD have the minimum data bit size limited by the wavelength of the laser employed. One of the promising alternative data storage concepts are probe based data storage systems.

In the early 1990s, researchers at IBM pioneered a new AFM based data storage using microcantilevers with integrated solid-state heaters [21]. Using a single AFM cantilever and polymer substrate, data writing and reading were demonstrated [7,8]. Localized heating in conjunction with mechanical pressure made nanoscale indents on the polymer coated substrate and written data bits were detected with the same heated cantilever tip by the thermal impedance change associated with the cantilever electrical resistance and temperature change.

A shortcoming of thermomechanical data storage was that the data rates are limited by the thermal time constant of the cantilever. Significant efforts have been made to increase data rates by parallelizing a number of microcantilevers and minimizing the integrated heater size. A 2 D array of the heated cantilever was proposed and this is the well known "Millipede" concept. 5 × 5 heated cantilever arrays in 5 mm × 5 mm showed the first possibility [29] and parallel operation of a 32 × 32 cantilever array defined in 3 mm × 3 mm was demonstrated and could achieve data areal density of 100 – 200 Gb/in$^2$ [22]. Recently, a 64 × 64 cantilever array was successfully fabricated and packaged in a

portable flash memory form factor to achieve a data density beyond 1Tb/in$^2$ [30] (see Figure 1.2). In conjunction with the array construction, there were efforts to minimize heater dimensions using electron beam lithography and the thermal time constants could also be improved [31].

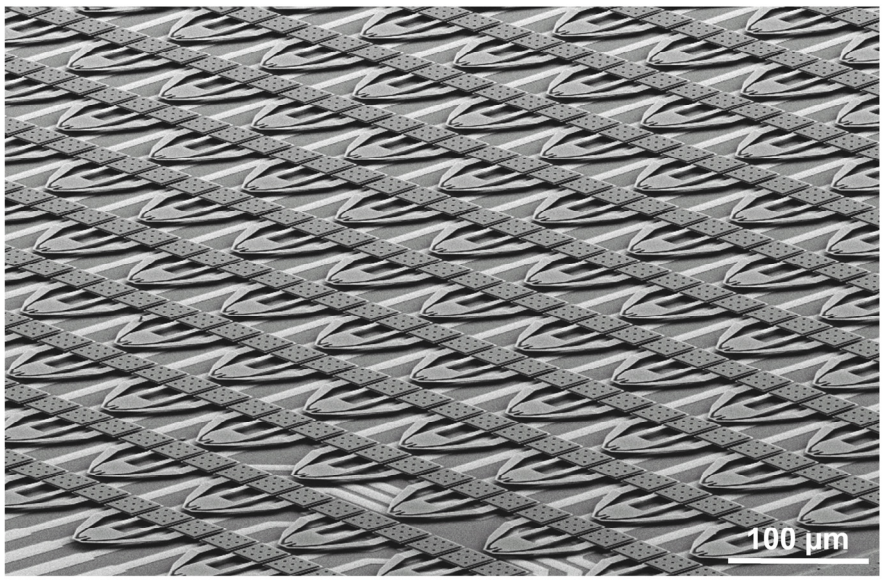


Figure 1.2 Scanning electron micrograph of 64 × 64 array of microcantilever heaters from IBM [32].

### 1.2.2 Scanning probe lithography

Dip-Pen Nanolithography (DPN) [33] is a scanning probe nanopatterning technique in which an AFM tip is used to deliver molecules from the tip to a surface (see Figure 1.3(a)). This direct writing technique offers high-resolution patterning capabilities for a number of molecular and biomolecular 'inks' on a variety of substrate types such as metals, semiconductors, and monolayer functionalized surfaces. Since DPN molecular transfer occurs through a water meniscus, there is molecular ink transfer whenever the probe tip makes contact with the substrate and this technique is not vacuum compatible.

DPN utilizing heated microcantilever probes was studied [16]. In this new technique called thermal dip pen nanolithography (tDPN), the probe is used much like a

soldering iron. A material is first coated onto the probe tip, and then the material is melted off the tip and onto another substrate in a controlled pattern only when the cantilever tip is heated above the melting temperature of the material coated (see Figure 1.3(b)). Material transfer can be actively controlled and does not require a water meniscus. So far, the technique has been used to deposit metals, semiconducting polymers, and functionalizable organics [16,17,34].

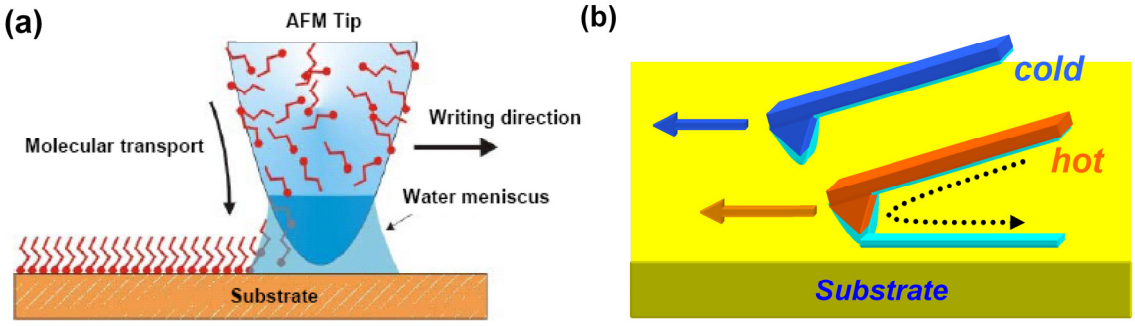


Figure 1.3 Principles of (a) Dip pen nanolithography [33] and (b) Thermal dip pen nanolithography [17].

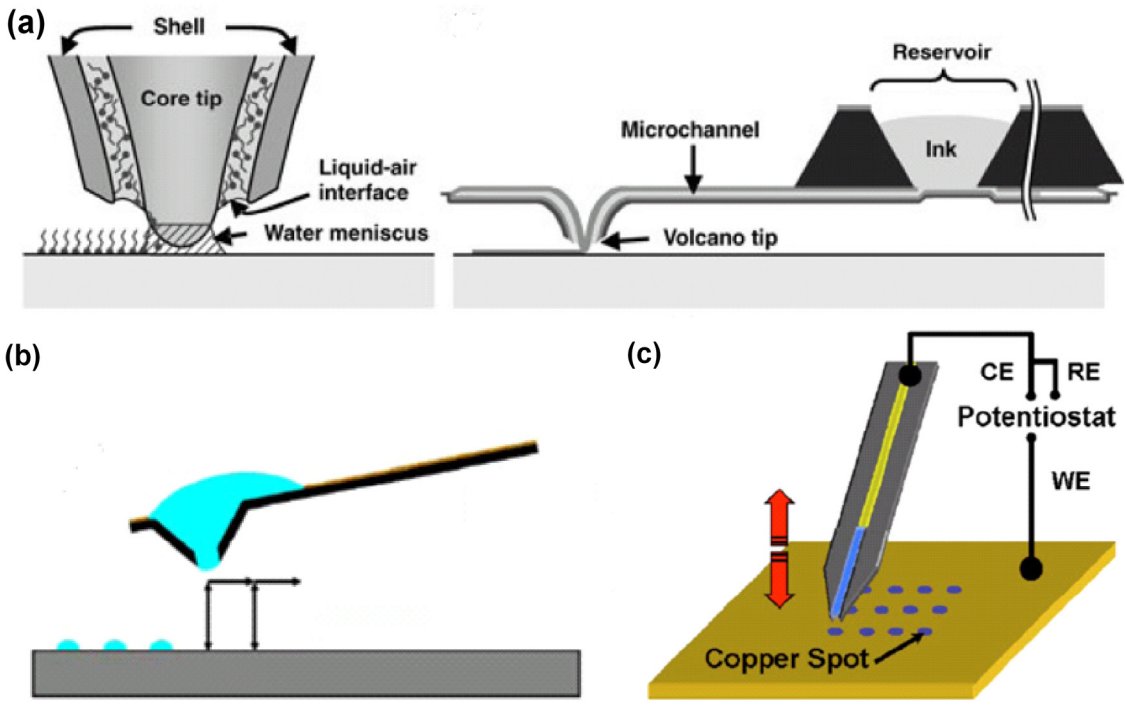


Figure 1.4 Principles of (a) Fountain pen nanolithography [35], (b) NADIS (nanoscale dispensing) [36], and (c) Eletrodeposition [37].

Since both DPN and tDPN have a common weakness in terms of 'ink' supply, there have been approaches to make continuous ink dispensing possible. Recently, fountain pen nanolithography (FPN) shown in Figure 1.4(a) was developed by integrating a microfludic channel and a fluid reservoir near a microcantilever [35]. NADIS (nanoscale dispensing) [38] has a similar advantage over the original DPN technique since there is a large liquid reservoir made around a hollow tip so that continuous nanopatterning becomes possible without frequent material reloading (see Figure 1.4(b)). Electrodeposition [37] and electrowetting actuation [39] using microcantilevers having a slit as a channel and a liquid reservoir were also advantageous due to the precise control of liquid loading and deposition.

The aforementioned techniques are all additive lithography methods because they are used to deposit materials from a microcantilever probe to a substrate. Subtractive maskless lithography based on microcantilever probes was proposed and demonstrated using a heated microcantilever. Heated microcantilevers fully decomposed an energetic material and made lithographic marks without a pileup or residue when the micro heater near the tip was heated above a threshold temperature [40].

### 1.2.3 Metrology using microcantilevers

#### 1.2.3.1 Nanostructure synthesis (Micro CVD)

Carbon nanotubes (CNTs) are famous nanostructures with extraordinary electronic, mechanical, and thermal properties [41,42]. One of the well-known CNT synthesis methods is thermal chemical vapor deposition, which requires thermal cycles including heating, dwell, and cooling of the entire synthesis furnace. Since this method

requires high temperature up to 900 °C, it is not possible to synthesize CNTs directly on MEMS or CMOS devices. However, it is often desirable to synthesize CNTs directly on functional mechanical or electronics system. A novel method for selectively synthesizing CNTs directly onto the heated AFM cantilever via chemical vapor deposition was reported [15]. By electrically heating the cantilever coated with a catalyst, CNTs could be synthesized selectively only where the local temperature was sufficiently high. After the CNT fabrication, the grown CNTs' mass was measured quantitatively by monitoring the cantilever's resonance frequency. Moreover, synthesized CNTs could be removed by electrically heating the cantilever to about 500 °C in oxygen environment.

1.2.3.2 Properties measurement

Microcantilevers have been heavily used for local measurements of mechanical, thermal, and electrical properties of the sample substrate. Elastic properties of surfaces, thin films, and nanostructures [43] and elastic modulus of polysilicon [44], polymer [45], polymer nanotubes [46] and a single peptide molecule [47] were measured using a modified AFM. Local elastic constants of a piezoelectric ceramic were measured using atomic force acoustic microscopy [48] and viscoelasticity of bio-molecules was studied on a single molecule level using force spectroscopy based on AFM [49]. Surface potential measurements were made through dissipative tip-sample interaction using non contact AFM combined with Kelvin-probe force microscopy [50]. In addition to solid samples, AFM was employed to measure the viscosity of an aqueous solution [51].

Non-contact AFM measured thermal transitions of polymers characterized by glass transition and melting temperature by monitoring resonance frequency of the polymers [52]. The glass transition temperature of polystyrene was measured using a

heated cantilever with nanometer spatial resolution by measuring tip penetration depth into the sample substrate [23] and a similar local thermal analysis was made on an energetic material [40]. Besides mechanical and thermal properties measurements, electrical conductivity / resistivity measurements were made using microcantilever four-point probes [53]. Most reported works herein are based on modified AFM metrologies or modified microcantilevers.

#### 1.2.3.3 Bio/chemical sensing

Piezoresistive cantilevers are widely used in bio/chemical sensing such as DNA hybridization [54,55], virus [56], explosives [57], and hazardous gas [58] detection among various MEMS structures. Often, cantilevers are prepared with a selective coating which is sensitive to a specific analyte. The analyte absorption induces static deflection by building surface stress and shifts resonance frequency due to the added mass. These cantilever mechanical responses can be measured by either static deflection or dynamic resonance. Along with the mechanical responses, thermal responses exist during bio/chemical adsorption or desorption processes that are usually accompanied by thermal energy changes. Both mechanical and thermal responses are characteristic such that functionalized microcantilevers can identify a specific bio/chemical sample without labeling.

## 1.3 Objectives of the Proposed Research

State-of-the-art microcantilever applications reviewed in the previous section strongly demand novel metrology development and multi-functional microcantilever fabrication. The main objective of the work in this thesis is to fabricate and characterize

microcantilever sensors and construct novel metrology tools based on microcantilevers. The research focuses on fabrication, characterization, and application of microcantilevers having integrated heaters and/or piezoresistors. In the first half, detailed characterization techniques and fabrication of novel microcantilever sensors will be discussed. In the second half, scientific and engineering applications relying on microcantilever sensors will be reported. Specifically, this thesis contains the following 8 chapters.

- This chapter (chapter 1) explains relevant work, gives a brief literature review, and motivation for this work.
- Chapter 2 describes detailed characterization of microcantilever heaters in electrical, thermal, and mechanical domains. The characterization techniques introduced will be used in later chapters.
- Chapter 3 focuses on fabrication of cantilever type micro hotplates which are specifically designed for chemical sensing.
- Chapter 4 focuses on fabrication and characterization of small 1 D arrays of microcantilever heaters with integrated piezoresistors. Possible applications of the fabricated device are discussed.
- Chapter 5 introduces a measurement of microcantilever heaters in partial vacuum. Sub-continuum heat transfer characteristics between a microfabricated heater and its gaseous environment will be discussed.
- Chapter 6 introduces a novel microcantilever metrology on micro / nanojet flows. Piezoresistive microcantilevers investigate jet velocity and thrust. Microcantilever heaters interrogate heat transfer characteristics upon micro /nanojet impingement.

- Chapter 7 describes advancement of microcantilever metrology for micro / nanojets appropriate for measuring breakup distance and boiling phenomena.
- Chapter 8 concludes this thesis with a summary and future work.

## 1.4 References


[1] G. Binnig, C. F. Quate, and C. Gerber, "Atomic force microscope," *Physical Review Letters*, vol. 56, pp. 930-933, 1986.

[2] G. Meyer and N. M. Amer, "Novel optical approach to atomic force microscopy," *Applied Physics Letters*, vol. 53, pp. 1045-1047, 1988.

[3] S. Alexander, L. Hellemans, O. Marti, J. Schneir, and V. Elings, "An atomic-resolution atomic-force microscope implemented using an optical lever," *Journal of Applied Physics*, vol. 65, pp. 164-167, 1989.

[4] M. Tortonese, R. Barrett, and C. Quate, "Atomic resolution with an atomic force microscope using piezoresistive detection," *Applied Physics Letters*, vol. 62, pp. 834-836, 1993.

[5] B. W. Chui, T. W. Kenny, H. J. Mamin, B. D. Terris, and D. Rugar, "Independent detection of vertical and lateral forces with a sidewall-implanted dual-axis piezoresistive cantilever," *Applied Physics Letters*, vol. 72, pp. 1388-1390, 1998.

[6] M. Napoli, B. Bamieh, and K. Turner, "A capacitive microcantilever: Modeling, validation, and estimation using current measurements," *Journal of Dynamic Systems, Measurement, and Control*, vol. 126, pp. 319-326, 2004.

[7] G. Binnig, M. Despont, U. Drechsler, W. Häberle, M. Lutwyche, P. Vettiger, H. J. Mamin, B. W. Chui, and T. W. Kenny, "Ultrahigh-density atomic force microscopy data storage with erase capability," *Applied Physics Letters*, vol. 76, pp. 1329-1331, 1999.

[8] W. P. King, T. W. Kenny, K. E. Goodson, G. L. W. Cross, M. Despont, U. Dürig, H. Rothuizen, G. Binnig, and P. Vettiger, "Atomic force microscope cantilevers for combined thermomechanical data writing and reading," *Applied Physics Letters*, vol. 78, pp. 1300-1302, 2001.

[9] J. Fricke and E. Obermeier, "Cantilever beam accelerometer based on surface micromachining technology," *Journal of Micromechanics and Microengineering*, vol. 3, pp. 190-192, 1993.

[10] H.-C. Lee, J.-H. Park, J.-Y. Park, H.-J. Nam, and J.-U. Bu, "Design, fabrication and RF performances of two different types of piezoelectrically actuated ohmic MEMS switches," *Journal of Micromechanics and Microengineering*, vol. 15, pp. 2098-2104, 2005.

[11] T. Thundat, G. Y. Chen, R. J. Warmack, D. P. Allison, and E. A. Wachter, "Vapor detection using resonating microcantilevers," *Analytical Chemistry*, vol. 67, pp. 519-521, 1995.

[12] D. Lange, C. Hagleitner, A. Hierlemann, O. Brand, and H. Baltes, "Complementary metal oxide semiconductor cantilever arrays on a single chip: Mass-sensitive detection of volatile organic compounds," *Analytical Chemistry*, vol. 74, pp. 3084-3095, 2002.

[13] L. A. Pinnaduwage, A. Gehl, D. L. Hedden, G. Muralidharan, T. Thundat, R. T. Lareau, T. Sulchek, L. Manning, B. Rogers, M. Jones, and J. D. Adams, "A microsensor for trinitrotoluene vapour," *Nature*, vol. 425, pp. 474, 2003.

[14] M. Su, S. Li, and V. P. Dravid, "Microcantilever resonance-based DNA detection with nanoparticle probes," *Applied Physics Letters*, vol. 82, pp. 3562-3564, 2003.

[15] E. O. Sunden, T. L. Wright, J. Lee, S. A. Graham, and W. P. King, "Room temperature chemical vapor deposition and mass detection on a heated atomic force microscope cantilever," *Applied Physics Letters*, vol. 88, pp. 033107, 2006.

[16] P. E. Sheehan, L. J. Whitman, W. P. King, and B. A. Nelson, "Nanoscale deposition of solid inks via thermal dip pen nanolithography," *Applied Physics Letters*, vol. 85, pp. 1589-1591, 2004.

[17] B. A. Nelson, W. P. King, A. Laracuente, P. E. Sheehan, and L. J. Whitman, "Direct deposition of continuous metal nanostructures by thermal dip-pen nanolithography," *Applied Physics Letters*, vol. 88, pp. 033104, 2006.

[18] B. W. Chui, T. D. Stowe, Y. S. Ju, K. E. Goodson, T. W. Kenny, H. J. Mamin, B. D. Terris, and R. P. Ried, "Low-stiffness silicon cantilever with integrated heaters and piezoresistive sensors for high-density data storage," *Journal of Microelectromechanical Systems*, vol. 7, pp. 69-78, 1998.

[19] S. R. Manalis, S. C. Minne, and C. F. Quate, "Atomic force microscopy for high speed imaging using cantilevers with an integrated actuator and sensor," *Applied Physics Letters*, vol. 68, pp. 871-873, 1996.

[20] H. P. Lang, M. Hegner, E. Meyer, and C. Gerber, "Nanomechanics from atomic resolution to molecular recognition based on atomic force microscopy technology," *Nanotechnology*, vol. 13, pp. R29-R36, 2002.

[21] H. J. Mamin and D. Rugar, "Thermomechanical writing with an atomic force microscope tip," *Applied Physics Letters*, vol. 61, pp. 1003-1005, 1992.

[22] P. Vettiger, G. Cross, M. Despont, U. Drechsler, U. Duerig, B. Gotsmann, W. Häberle, M. Lantz, H. Rothuizen, R. Stutz, and G. Binnig, "The "Millipede"-nanotechnology entering data storage," *IEEE Transactions on Nanotechnology*, vol. 1, pp. 39-64, 2002.

[23] B. A. Nelson and W. P. King, "Measuring material softening with nanoscale spatial resolution using heated silicon probes," *Review of Scientific Instruments*, in press.

[24] Y. Su, A. G. R. Evans, A. Brunnschweiler, and G. Ensell, "Characterization of a highly sensitive ultra-thin piezoresistive silicon cantilever probe and its application in gas flow velocity sensing," *Journal of Micromechanics and Microengineering*, vol. 12, pp. 780-785, 2002.

[25] L. M. Roylance and J. B. Angell, "A batch fabricated silicon accelerometer," *IEEE Transactions on Electron Devices*, vol. 26, pp. 1911-1917, 1979.

[26] J. Thaysen, R. Marie, and A. Boisen, "Cantilever-based bio-chemical sensor integrated in a microliquid handling system " *IEEE MEMS*, pp. 401-404, 2001.

[27] Y. S. Kim, C. S. Lee, W. H. Jin, S. Jang, H. J. Nam, and J. U. Bu, "100 × 100 thermo-piezoelectric cantilever array for SPM nano-data-storage application," *Sensors and Materials*, vol. 17, pp. 57-63, 2005.

[28] D. Weller and A. Moser, "Thermal effect limits in ultrahigh-density magnetic recording," *IEEE Transactions on Magnetics*, vol. 35, pp. 4423-4439, 1999.

[29] M. Lutwyche, C. Andreoli, G. Binnig, J. Brugger, U. Drechsler, W. Häberle, H. Rohrer, H. Rothuizen, P. Vettiger, G. Yaralioglu, and C. Quate, "5 × 5 2D AFM cantilever arrays a first step towards a Terabit storage device," *Sensors and Actuators, A*, vol. 73, pp. 89-94, 1999.

[30] M. Despont, T. Altebaeumer, P. Bächtold, G. K. Binnig, G. Cherubini, U. Drechsler, U. Dürig, E. Eleftheriou, B. Gotsmann, W. Häberle, C. Hableitner, D. Jubin, A. Knoll, M. A. Lantz, A. Pantazi, H. Pozidis, H. Rothuizen, A. Sebastian, R. Stutz, P. Vettiger, D. Wiesmann, and J. Windeln, "A highly parallel probe-based storage system," *Digest of Papers - Microprocess and Nanotechnology 2004*, pp. 4-5, 2004.

[31] U. Brechsler, N. Burer, M. Despont, U. Dürig, B. Gotsmann, F. Robin, and P. Vettiger, "Cantilevers with nano-heaters for thermomechanical storage application," *Microelectronic Engineering*, vol. 67-68, pp. 397-404, 2003.

[32] http://www.zurich.ibm.com/imagegallery/millipede/#.

[33] R. D. Piner, J. Zhu, F. Xu, S. Hong, and C. A. Mirkin, ""Dip-pen" nanolithography," *Science*, vol. 283, pp. 661-663, 1999.

[34] M. Su, X. G. Liu, S. Y. Li, V. P. Dravid, and C. A. Mirkin, "Moving beyond molecules: Patterning solid-state features via dip-pen nanolithography with sol-based inks," *Journal of the American Chemical Society*, vol. 124, pp. 1560-1561, 2002.

[35] K. H. Kim, N. Moldovan, and H. D. Espinosa, "A nanofountain probe with sub-100 nm molecular writing resolution," *Small*, vol. 1, pp. 632-635, 2005.

[36] A. Meister, S. Krishnamoorthy, C. Hinderling, R. Pugin, and H. Heinzelmann, "Local modification of micellar layers using nanoscale dispensing," *Microelectronic Engineering*, vol. 83, pp. 1509-1512, 2006.

[37] T. Leichle, L. Nicu, E. Descamps, B. Corso, P. Mailley, T. Livache, and C. Bergaud, "Copper electrodeposition localized in picoliter droplets using microcantilever arrays," *Applied Physics Letters*, vol. 88, pp. 254108, 2006.

[38] A. Meister, S. Jeney, M. Liley, T. Akiyama, U. Staufer, N. F. de Rooij, and H. Heinzelmann, "Nanoscale dispensing of liquids through cantilevered probes," *Microelectronic Engineering*, vol. 67-8, pp. 644-650, 2003.

[39] T. Leichle, D. Saya, J. B. Pourciel, F. Mathieu, L. Nicu, and C. Bergaud, "Liquid loading of silicon-based cantilevers using electrowetting actuation for microspotting applications," *Sensors and Actuators A*, vol. 132, pp. 590-596, 2006.

[40] W. P. King, S. Saxena, B. A. Nelson, B. L. Weeks, and R. Pitchimani, "Nanoscale thermal analysis of an energetic material," *Nano Letters*, vol. 6, pp. 2145-2149, 2006.

[41] W. A. deHeer, W. S. Bacsa, A. Chatelain, T. Gerfin, R. Humphrey-Baker, L. Forro, and D. Ugarte, "Aligned carbon nanotube films: production and optical and electronic properties," *Science*, vol. 268, pp. 845-847, 1995.

[42] M. M. J. Treacy, T. W. Ebbesen, and J. M. Gibson, "Exceptionally high Young's modulus observed for individual carbon nanotubes," *Nature*, vol. 381, pp. 678-680, 1996.

[43] D. C. Hurley, M. Kopycinska-Muller, A. B. Kos, and R. H. Geiss, "Nanoscale elastic-property measurements and mapping using atomic force acoustic microscopy methods," *Measurement Science & Technology*, vol. 16, pp. 2167-2172, 2005.

[44] C. Serre, P. Gorostiza, A. Perez-Rodriguez, F. Sanz, and J. R. Morante, "Measurement of micromechanical properties of polysilicon microstructures with an atomic force microscope," *Sensors and Actuators A*, vol. 67, pp. 215-219, 1998.

[45] H. Y. Nie, M. Motomatsu, W. Mizutani, and H. Tokumoto, "Local elasticity measurement on polymers using atomic force microscopy," *Thin Solid Films*, vol. 273, pp. 143-148, 1996.

[46] S. Cuenot, C. Fretigny, S. Demoustier-Champagne, and B. Nysten, "Measurement of elastic modulus of nanotubes by resonant contact atomic force microscopy," *Journal of Applied Physics*, vol. 93, pp. 5650-5655, 2003.

[47] A. Ptak, S. Takeda, C. Nakamura, J. Miyake, M. Kageshima, S. P. Jarvis, and H. Tokumoto, "Modified atomic force microscope applied to the measurement of elastic modulus for a single peptide molecule," *Journal of Applied Physics*, vol. 90, pp. 3095-3099, 2001.

[48] U. Rabe, S. Amelio, M. Kopycinska, S. Hirsekorn, M. Kempf, M. Goken, and W. Arnold, "Imaging and measurement of local mechanical material properties by atomic force acoustic microscopy," *Surface and Interface Analysis*, vol. 33, pp. 65-70, 2002.

[49] C. A. Bippes, A. D. L. Humphris, M. Stark, D. Muller, and H. Janovjak, "Direct measurement of single-molecule visco-elasticity in atomic force microscope force-extension experiments," *European Biophysics Journal with Biophysics Letters*, vol. 35, pp. 287-292, 2006.

[50] T. Fukuma, K. Kobayashi, H. Yamada, and K. Matsushige, "Surface potential measurements by the dissipative force modulation method," *Review of Scientific Instruments*, vol. 75, pp. 4589-4594, 2004.

[51] N. Ahmed, D. F. Nino, and V. T. Moy, "Measurement of solution viscosity by atomic force microscopy," *Review of Scientific Instruments*, vol. 72, pp. 2731-2734, 2001.

[52] M. Meincken, L. J. Balk, and R. D. Sanderson, "Measurement of thermal parameters and mechanical properties of polymers by atomic force microscopy," *Surface and Interface Analysis*, vol. 35, pp. 1034-1040, 2003.

[53] C. L. Petersen, T. M. Hansen, P. Boggild, A. Boisen, O. Hansen, T. Hassenkam, and F. Grey, "Scanning microscopic four-point conductivity probes," *Sensors and Actuators A*, vol. 96, pp. 53-58, 2002.

[54] R. C. W. Marie, C. B. V. Christensen, and A. Boisen, "DNA hybridization detected by cantilever-based sensor with integrated piezoresistive read-out," presented at Proceedings of MicroTAS 2004, 2004.

[55] R. L. Gunter, R. Zhine, W. G. Delinger, K. Manygoats, A. Kooser, and T. L. Porter, "Investigation of DNA sensing using piezoresistive microcantilever probes," *IEEE Sensors Journal*, vol. 4, pp. 430-433, 2004.

[56] R. L. Gunter, W. G. Delinger, K. Manygoats, A. Kooser, and T. L. Porter, "Viral detection using an embedded piezoresistive microcantilever sensor," *Sensors and Actuators A*, vol. 107, pp. 219-224, 2003.

[57] L. A. Pinnaduwage, A. Wig, D. L. Hedden, A. Gehl, D. Yi, T. Thundat, and R. T. Lareau, "Detection of trinitrotoluene via deflagration on a microcantilever," *Journal of Applied Physics*, vol. 95, pp. 5871-5875, 2004.

[58] A. Kooser, R. L. Gunter, W. D. Delinger, T. L. Porter, and M. P. Eastman, "Gas sensing using embedded piezoresistive microcantilever sensors," *Sensors and Actuators B*, vol. 99, 2003.

# CHAPTER 2

# ELECTRICAL, THERMAL, AND MECHANICAL CHARACTERIZATION OF SILICON MICROCANTILEVER-HEATERS

## 2.1 Introduction

AFM cantilevers having integrated solid-state heating elements were originally designed for data storage [1,2] and have enabled progress on highly parallel AFM and compact data storage [3]. Despite significant effort on engineering heated AFM cantilevers [4-7], most previous research has focused on designing the cantilever for data storage applications and integration into large arrays to accommodate parallelization. Only little work has been done on characterization and precision calibration of these cantilevers, and that work exclusively focused on requirements for data storage [1,8,9]. However, emerging applications of heated AFM cantilevers such as nanometer-scale manufacturing [10-12], metrology [13,14] and thermophysical property measurements [15,16] all demand temperature calibration and mechanical characterization beyond what has been previously reported. Therefore, detailed characterization and calibration of heated AFM cantilevers are required for these emerging applications, with the aim of creating new opportunities for the use of heated AFM cantilevers.

A number of studies have investigated heat transfer in the heated AFM cantilever, the cantilever tip, and its surroundings. Finite element simulations that included the

temperature-dependence of the cantilever's electrical characteristics predicted power consumption and speed [1,8], reading sensitivity [13], and intrinsic carrier-based "thermal runaway" characteristics [17]. This thermal runaway has a well-behaved temperature-dependence and has therefore been used as a temperature reference for the heated cantilever [9,18]. This temperature calibration is typically done as follows: the electrical resistance at room temperature and zero heating power, as well as the power and temperature at thermal runaway are found, and then any point in between the two is interpolated [18]. Not only is this approximate calibration inaccurate, but it also can not be applied beyond the thermal runaway temperature, which is typically 500-600 °C.

Different applications of heated AFM cantilevers will each place unique demands on cantilever operation and characterization. For thermomechanical data writing, the heated AFM tip is required to maintain its temperature above the glass transition temperature of a substrate polymer in contact with the tip for a sufficiently long time to deform the polymer and to form nanoscale data bit indents [2,4]. In data-reading mode, the cantilever is heated to a temperature high enough for accurate sensing, but below the point at which the polymer media would get deformed. Small changes in the cantilever temperature can be detected from changes in the resistance as the tip scans over written indents, which allows for reading [4]. While the cantilever temperature is important for the design of the writing and reading processes, it is not an important parameter to monitor during the actual device operation, and thus precise temperature calibration of the heated AFM cantilever has not been emphasized for data storage. In contrast, new applications such as local control of chemical vapor deposition processes [12] and nanoscale deposition of solid materials [10,11] demand precise measurements of

temperature and heat flux. Furthermore, if the heated cantilever is to be used for bio/chemical sensing [19-21], thermomechanical bending in the cantilever should be well understood.

The development of all-silicon heated AFM cantilevers was a significant advancement over previous work on heated AFM cantilevers, as silicon AFM cantilevers having integrated heaters could reach higher temperatures, could heat more quickly, and had reduced thermally-induced bending. However, detailed investigations showed that thermally-induced bending was not entirely suppressed [8,16]. Characterization of temperatures and stresses are important to assess the operational bounds of the heated AFM cantilevers while at the same time ensuring reliability. During the operation of these devices, temperature measurements are often performed without regard for simultaneous stress evolution due to the difficulty in performing such measurements concurrently. In general, the measurements of temperature and stress in these devices are not trivial due to their size scale and the temperature range over which they operate. Recently, micro-Raman spectroscopy has shown some distinct advantages over other techniques such as infrared microscopy and thermoreflectance since it can measure both temperature and stress simultaneously in silicon based MEMS devices [22-24]. Improvements in both temperature calibration and mechanical characterization would improve the operation of these cantilevers.

This chapter reports electrical, thermal, and mechanical characterization of heated AFM cantilevers. The heated cantilever was characterized in both time and frequency domains using direct current (DC), square pulse, and alternating current (AC) excitation. Raman spectroscopy was used to measure local temperature of the heated cantilevers

with electrical excitation and to measure thermally induced stresses. The spectrum of the cantilever's thermal vibration was used for mechanical characterization and the results were confirmed by finite element analysis.

## 2.2 Cantilever Instrumentation

The heated AFM cantilevers were made using a standard silicon-on-insulator (SOI) process generally following a documented fabrication process [8], which was modified to suit our fabrication facility [25] and is briefly summarized as follows. The fabrication process started with a SOI wafer of orientation <100>, and n-type doping at $2\times10^{14}$ $cm^{-3}$ having a resistivity of approximately 4 Ω-cm. The cantilever tip was formed using an oxidation sharpening process [26] and had a radius of curvature near 20 nm. The cantilever was made electrically active through two phosphorous doping steps: first, the two parallel cantilever legs were doped to $1\times10^{20}$ $cm^{-3}$ and then the heater region near the free end of the cantilever was doped to $1\times10^{17}$ $cm^{-3}$. Therefore, the heater region was more resistive than the rest of the cantilever. With the cantilever dimensions and temperature-dependent resistivities, the cantilever electrical resistance depends on the cantilever temperature solely in the heater region to within 10 % [8,27-29]. Figure 2.1 shows scanning electron microscope (SEM) and infrared (IR) microscope images of the fabricated heated cantilever, the latter of which indicating heating only near the free end of the cantilever.

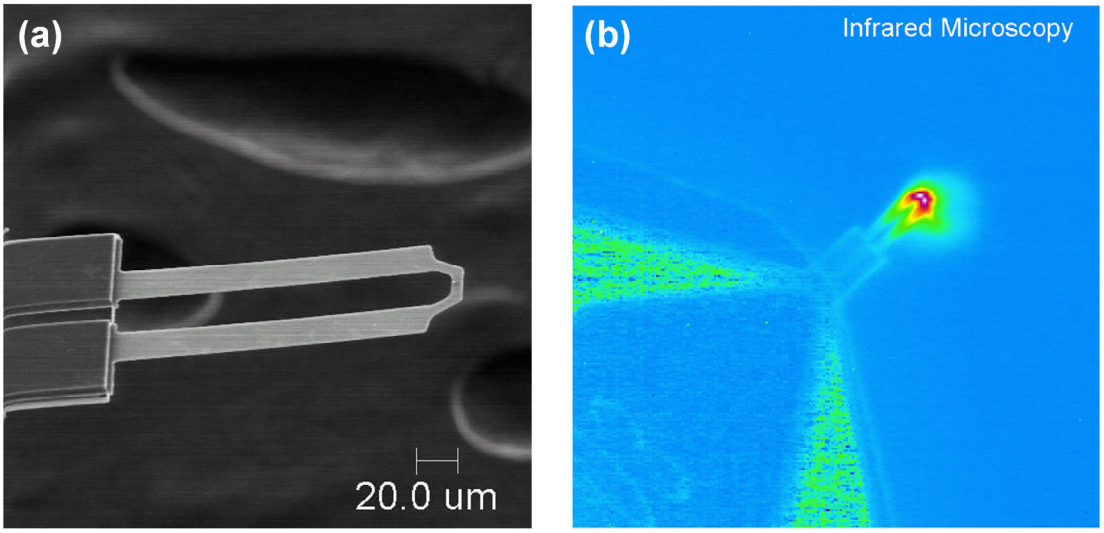


Figure 2.1 (a) Scanning electron microscope image of microcantilever heater (b) Infrared microscope image of the heater cantilever during steady electrical excitation. The IR image is approximately 0.5 mm square. The doped silicon cantilever is fabricated in a 'U' shape such that it forms a continuous electrical path. The region near the cantilever free end is a highly resistive heater and the legs have lower electrical resistance such that they carry electricity. The IR image confirms substantial heating only near the free end of the cantilever.

Figure 2.2 shows the electronic circuit used to operate and characterize the heated AFM cantilever throughout this chapter. The circuit has a simple bridge "sense" resistor connected in series to the cantilever to protect it by limiting the current at high power as well as to sense the current during pulse excitation. A high speed amplifier was configured when the cantilever was operated with a sense resistor having high resistance. In the following, $V_{total}$ refers to the bridge voltage after amplification that is applied to the series resistance of the cantilever and sense resistor. An Agilent 33450A function generator supplied DC, square pulse, and AC voltage excitation while an Agilent 34401A digital multimeter and an Agilent Infiniium 54831B oscilloscope measured the voltage drop across the sense resistor with DC and pulse/AC excitation, respectively. With this instrumentation, the cantilever's electrical resistance and power dissipation can be obtained.

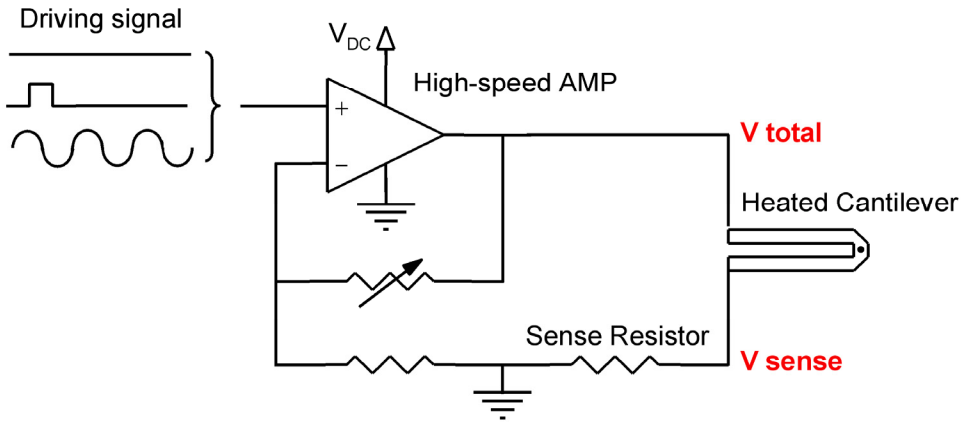


Figure 2.2 Testing circuit used to characterize the cantilever. There is a sense resistor connected to the cantilever in series to protect the cantilever at high power and to sense the current during pulse excitation. A high speed amplifier is configured when the cantilever is operated with a sense resistor having high resistance.

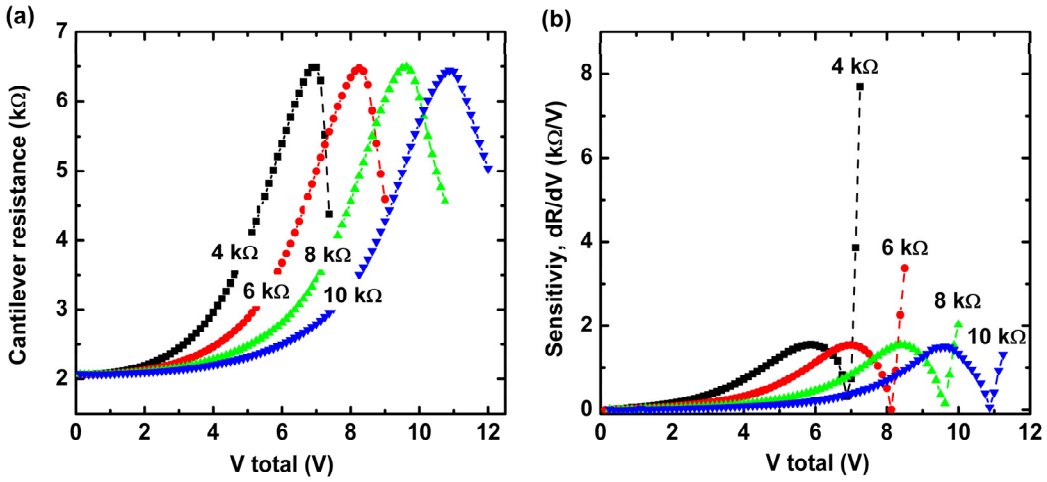


Figure 2.3 (a) Typical cantilever DC responses with various sensor resistors. As the resistance of the resistor decreases, more power will be dissipated in the cantilever with a given excitation voltage. (b) Resistance sensitivity – ratio of the cantilever resistance change to the input voltage change – as a function of the excitation voltage for different sense resistors. The resistance sensitivity increases as the resistance value decreases such that a resistor having high resistance is preferred to protect the cantilever.

Figure 2.3 shows the typical cantilever DC response in quiescent air. The cantilever's electrical resistivity is a highly nonlinear function of temperature. Overall the shape of the cantilever's electrical response depends upon the temperature-dependence of the cantilever's electrical properties, the circuit driving the cantilever, and

the thermal conductance from the cantilever. All of these parameters are described in more detail in the following sections.

Figure 2.3(a) shows the cantilever DC response for operation with various sense resistors. For lower resistance of the sense resistor, more power was dissipated in the cantilever for a given excitation voltage. The point at which the temperature coefficient of resistance (TCR) of the cantilever changes from positive to negative is the "thermal runaway" point and occurs at lower excitation voltage for smaller series resistances. Figure 2.3(b) shows the resistance sensitivity, which is the ratio of the cantilever resistance change to the input voltage change, as a function of the excitation voltage for different series resistors. For this cantilever, which has a room temperature resistance near 2 kΩ, the resistance sensitivity increases as the magnitude of the sense resistance decreases. A sense resistor with small resistance yields high resistance sensitivity when the cantilever has negative TCR such that a small voltage increase can change the cantilever temperature significantly. In general, a sense resistor having high resistance is preferred to protect the cantilever; however, using a higher resistance increases the required excitation voltage to raise the cantilever temperature because of the elevated power dissipation in the series resistor, thus requiring an amplifier that complicates the testing circuit. For the remainder of this chapter, a 10 kΩ resistor was chosen as a sense resistor after consideration of both resistance sensitivity and power dissipation. One conclusion that can be made from Figure 2.3 is that reports of cantilever electrical characteristics may be incomplete without also reporting the details of the bridge circuit used to operate the cantilever. The characteristics of the cantilever shown in Figure 2.3 were consistently observed over more than 300 cantilevers, although there were small

variations within each wafer and between wafers that can be attributed to nonuniformity in one or more of the fabrication steps.

## 2.3 Electrical Testing

Using the aforementioned testing setup, the cantilever electrical resistance was obtained by stepping through voltage from 0.125 to 12 V in 0.125 V increments while the duration of each voltage was 1 second. All measurements were made with enough time delay enough to ensure steady state conditions of the heated cantilever after the target voltage was set.

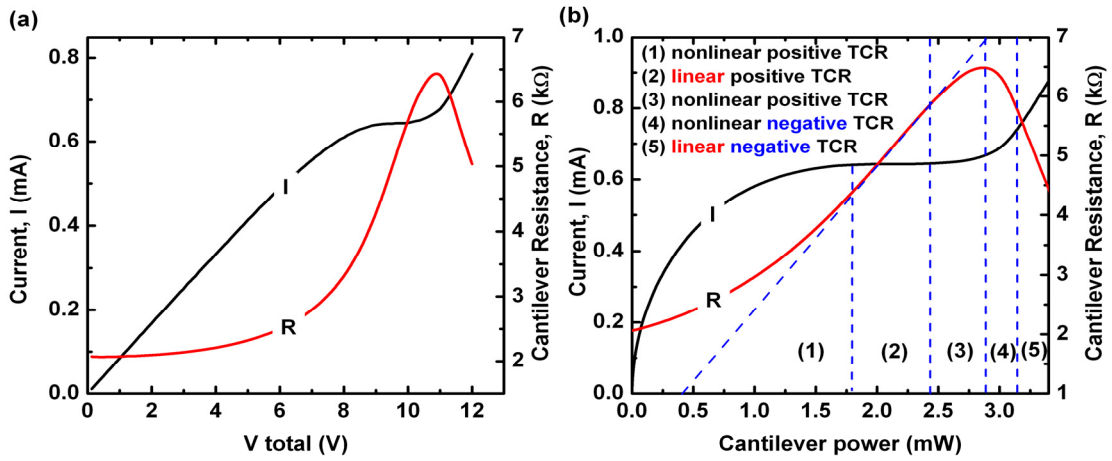


Figure 2.4 (a) Current and cantilever resistance as functions of DC excitation voltage showing temperature-dependent resistivities and thermal runaway of doped silicon. (b) Current and resistance as functions of cantilever power. The cantilever resistance is overall nonlinear but partially linear and TCR changes from positive to negative.

Figure 2.4(a) shows current and cantilever resistance as functions of DC excitation voltage for the cantilever mounted in quiescent air at 25 °C. Figure 2.4(b) shows current and resistance as functions of cantilever power and clearly displays five different regimes. Overall, the cantilever resistance was nonlinear with respect to cantilever power or heater temperature but had two distinct regions of linear response.

The TCR changed from positive to negative over the voltage range employed. When the cantilever power was higher than 3.2 mW, the heated cantilever had a negative linear TCR which was much higher than the positive linear TCR displayed between 1.6 and 2.4 mW. The range over which the cantilever TCR is linear or nearly linear is substantial, and offers opportunities to operate the cantilever as a thermal sensor.

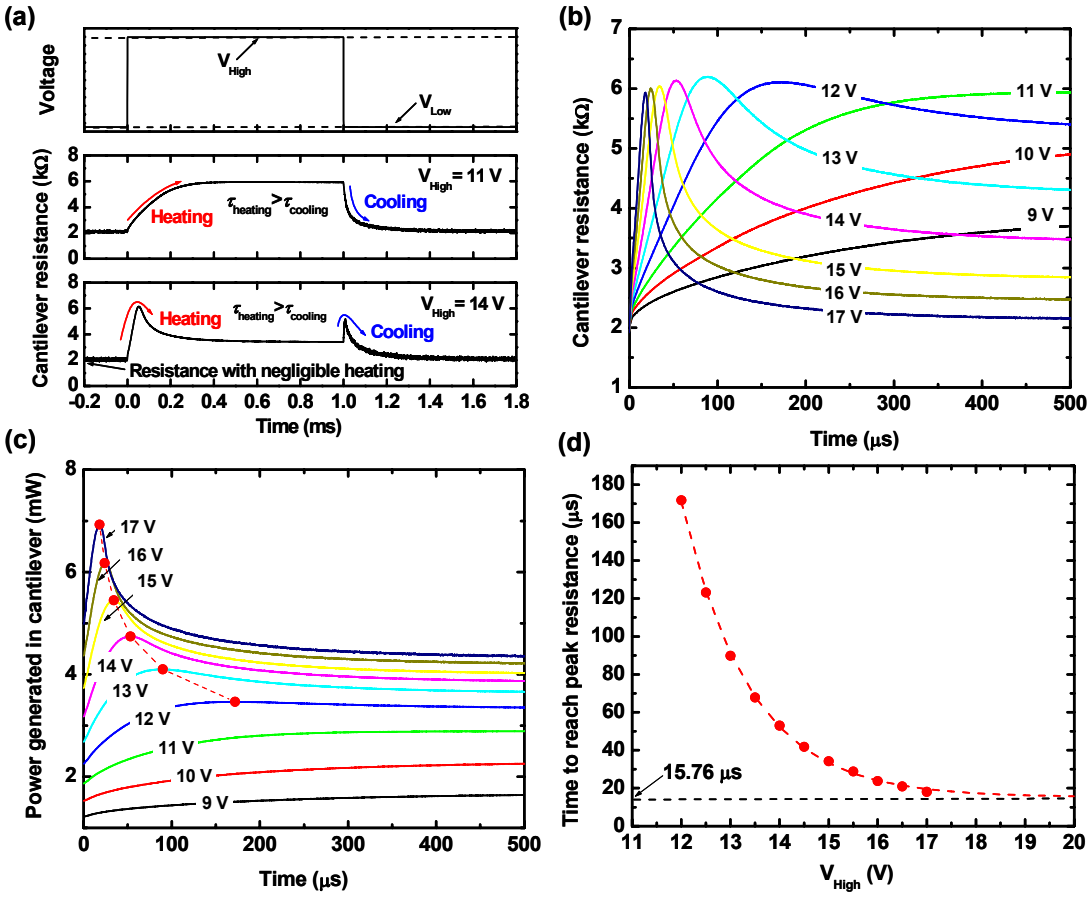


Figure 2.5 (a) Two distinct responses of the cantilever resistance depending upon the high voltage level, $V_{high}$ where square pulses of 1ms duration are applied to the cantilever with minimum voltage level of 0.5V. (b), (c) Cantilever resistance and generated power in the cantilever increase monotonically and reach steady state when $V_{high}$ is lower than $V_{Peak}$. With higher $V_{high}$, the cantilever resistance and generated power increase, reach the maximum, and then decrease until the cantilever reaches steady state (d) The heated cantilever can reach approximately 560 °C within 16 μs.

When a voltage pulse is applied to the cantilever, the cantilever temperature increases and if the pulse is sufficiently long, may eventually reach a steady value. After

the pulse has elapsed, the cantilever temperature drops and recovers the initial temperature exponentially. Square pulse excitation can provide insight into how the cantilever behaves and responds to electrical excitation in short time periods. Square pulses of 1 ms duration were applied to the cantilever with a 0.5 V DC offset to monitor the cantilever resistance before and after the square pulse.

Figure 2.5(a) shows two distinct responses of the cantilever resistance depending upon the high voltage level, $V_{high}$. When $V_{high}$ was below the voltage corresponding to the peak resistance, $R_{Peak}$, in DC response, $V_{Peak}$, the cantilever resistance increased and decreased monotonically during the heating and cooling cycles, respectively. When $V_{high}$ was above $V_{Peak}$, the cantilever resistance initially increased and then decreased during both the heating and the cooling cycle. The cooling was always faster than the heating regardless of $V_{high}$. For the heating times considered, cooling was more efficient than heating, as heating was highly localized around the heater while the cooling takes place at all points around the cantilever. The experiments were repeated with various levels of $V_{high}$, shown in Figure 2.5(b). Figure 2.5(c) shows that similar to the resistance evolution, the generated power in the cantilever increased monotonically and reached steady state when $V_{high}$ was lower than $V_{Peak}$. With increased $V_{high}$, the cantilever resistance and generated power increased, reached the maximum, and then decreased until the cantilever reached steady state.

From the pulse response, the time constant, $\tau$, observed to be on the order of 100 μs shows good agreement with theoretical estimations given by $\tau = L^2 / \alpha$ where $L$ is the length of the cantilever and $\alpha$ is the thermal diffusivity of the silicon cantilever. Thus,

the heated cantilever requires approximately 100 μs to reach a steady state temperature distribution throughout the entire cantilever structure. However, this does not limit the cantilever from operating on a faster time scale. The cantilever heater can reach sufficiently high temperatures for metrology and manufacturing applications within less than 20 μs by controlling $V_{high}$ and duty cycle. For example, the heated cantilever can reach about 560 °C corresponding to $R_{Peak}$ within 16 μs as shown in Figure 2.5(d).

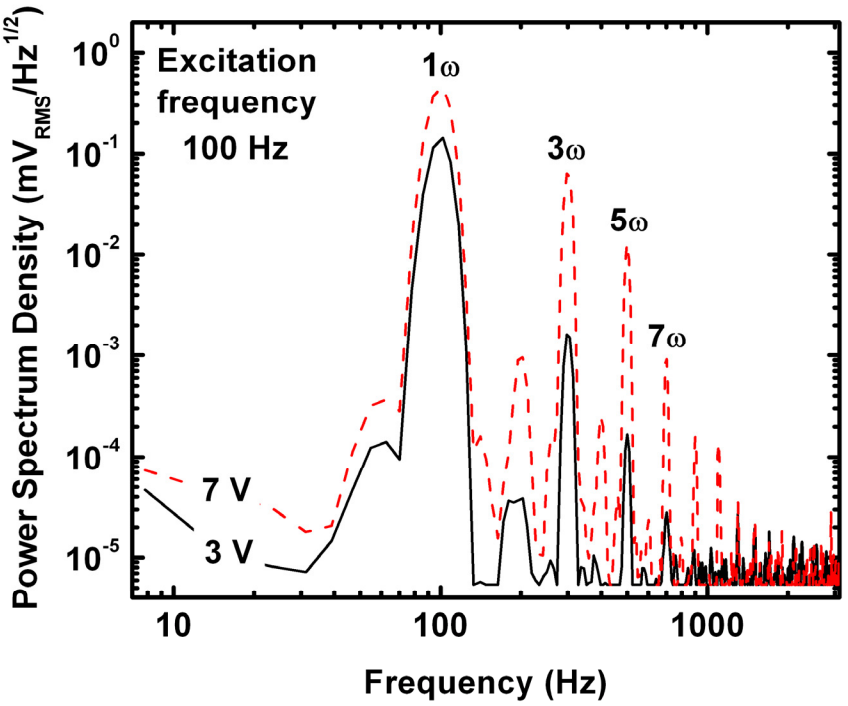


Figure 2.6 Power spectrum density of the heated cantilever with 100 Hz sinusoidal excitation. As AC voltage increases, more high order overtones are generated due to highly nonlinear cantilever resistance.

When any resistive element is operated with fully reversed oscillatory electrical excitation having frequency $\omega$, the power dissipation in the resistive load will oscillate at frequency $2\omega$ and the device temperature/resistance will follow the power oscillation. The generated $2\omega$ resistance oscillation will generate a $3\omega$ component to the voltage oscillation in conjunction with 1ω current input and higher overtones will be cascaded in

a similar fashion. Temperature fluctuations in the heated AFM cantilever can be examined using AC excitation at moderate frequencies. High order harmonics from the heated cantilever were examined with a fast Fourier transform spectrum analyzer when the heated cantilever was operated under periodic excitation. These higher order harmonics arise from the heterodyne mixing of voltage signals in the cantilever with successively higher harmonics having smaller amplitudes. Figure 2.6 shows the power spectrum density of the heated cantilever with 100 Hz AC excitation. As AC voltage increases, more high order overtones are detected as a result of the highly nonlinear temperature dependent resistance of the cantilever.

The cantilever AC responses were examined by frequency sweep of 5V-rms AC from 100 Hz to 3 MHz, shown in Figure 2.7. During AC operation, the heated cantilever experienced 2 thermal cycles – heating and cooling - in each periodic excitation. At a given frequency, steady resistance ($R_s$), resistance oscillation ($\Delta R$), and reactance ($X$) of the cantilever were obtained using experimental data and phasor analysis and the cantilever heater temperature was measured using Raman spectroscopy. It should be noted that Raman spectroscopy is limited for transient temperature measurements considering the required exposure time to acquire a high enough number of photons. However, the temperature oscillation not included herein can be extracted from $\Delta R$ and resistance – temperature calibration. There were two different regimes characterized by the oscillation amplitude of the cantilever resistance and the magnitude of the reactance. In the low frequency regime, the oscillation amplitude of the resistance was constant first and then started to decrease but the steady resistance was almost constant as the

frequency increased. The cantilever resistance oscillated around the steady resistance which was close to the cantilever initial resistance with the finite amplitude.

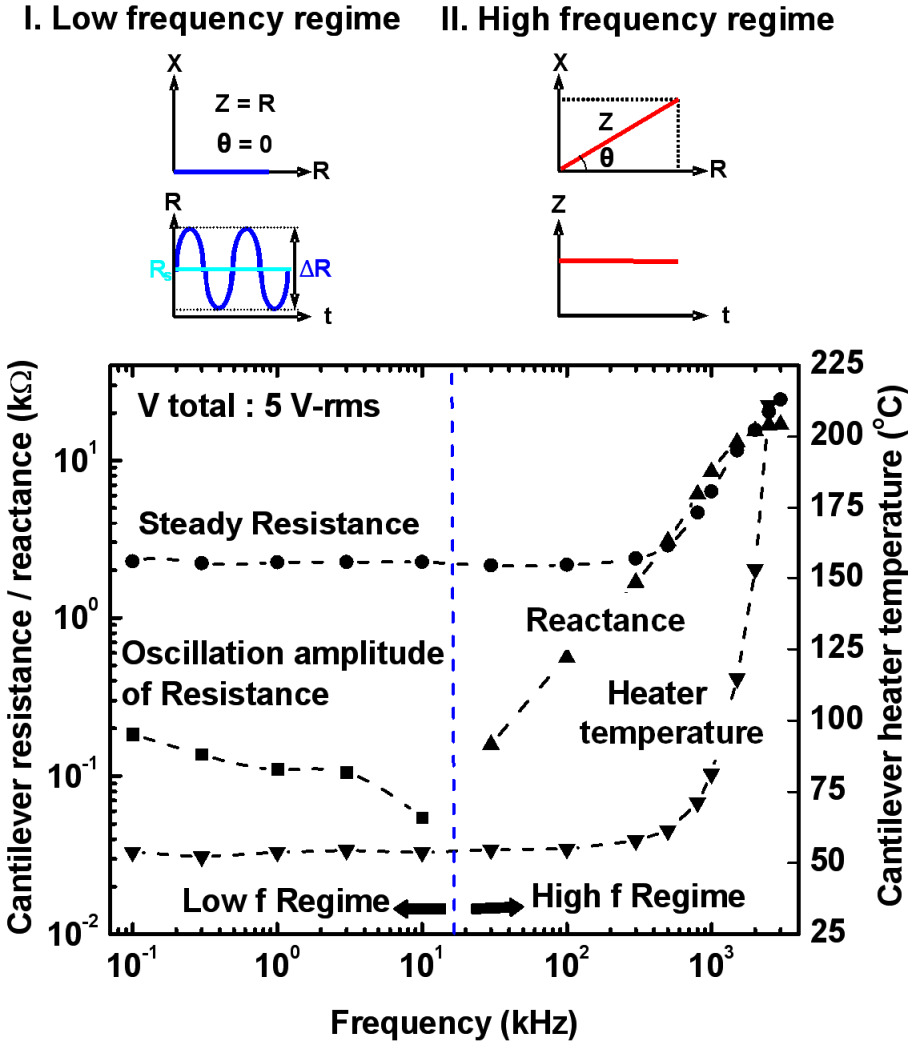


Figure 2.7 The cantilever AC responses are examined by frequency sweep of 5V-rms AC from 100 Hz to 3 MHz. At a given frequency, steady resistance ( $R_s$ ), resistance oscillation ( $\Delta R$ ), and reactance ( $X$ ) of the cantilever are obtained using experimental data and phasor analysis and cantilever heater temperature is measured using Raman spectroscopy. There are two different regimes characterized by oscillation amplitude of the cantilever resistance and reactance.

In the high frequency regime, the oscillation amplitude became negligible and the cantilever reactance was observed. There was a transition where the cantilever steady resistance and heater temperature begin to become frequency-dependent. Overall, the

heated cantilever can follow heating and cooling cycles well at low frequencies but its resistance and temperature oscillation dies out and thermal phase lag shows up at high frequencies. More detailed AC responses of the heated AFM cantilever were reported in [30].

## 2.4 Temperature Measurements

Raman spectroscopy is an optical measurement technique well suited for the temperature and stress measurements in MEMS devices, especially those made from silicon due to its strong scattering cross-section [22]. Raman Spectroscopy measures inelastic scattering of light from materials, resulting from changes in the polarizability of the atoms. Thus, any effect which may change the lattice spacing and polarizability of nonmetallic solids will result in changes in the Raman signature. Raman scattering has been used to determine temperature distribution with micron spatial resolution in diamond structures [31], silicon [32-34], III-V semiconductors [35-38], and polysilicon MEMS [39].

A Renishaw InVia Raman Microscope with 180º backscattering geometry was used to measure cantilever temperature with electrical excitation in quiescent air at 25 °C. The sample excitation utilized a 488 nm Ar+ laser while the collection was performed with a 0.25 m focal length spectrometer and a 3000 l/mm grating. The slit was set at 15 μm to maximize the spectral resolution. A 50× objective was used to collect the Raman signature of the devices which provided a focal spot of 1 μm. The laser power at the exit of the microscope objective was measured to be 45.4 μW. This power setting insured that there was no change in Raman spectra due to laser heating.

Raman collection times were chosen such that the peak height was at least 1500 photoelectron counts for all measurements. Several spectra were obtained at each location in order to reduce the uncertainty of the Stokes line width (FWHM : Full width at half maximum) and peak position found using a Voigt curve fitted to the acquired data. Cantilever characterization was performed by scanning the surface of the cantilever at several input powers, with a peak heater temperature of approximately 560°C. The Raman scan at zero input power was used as a reference. Measurements were taken across the surface of the cantilever from the tip to the base on both the top and bottom of the cantilever. After these testings, a second scan without power input was then taken to examine any changes which occurred due to cantilever operation.

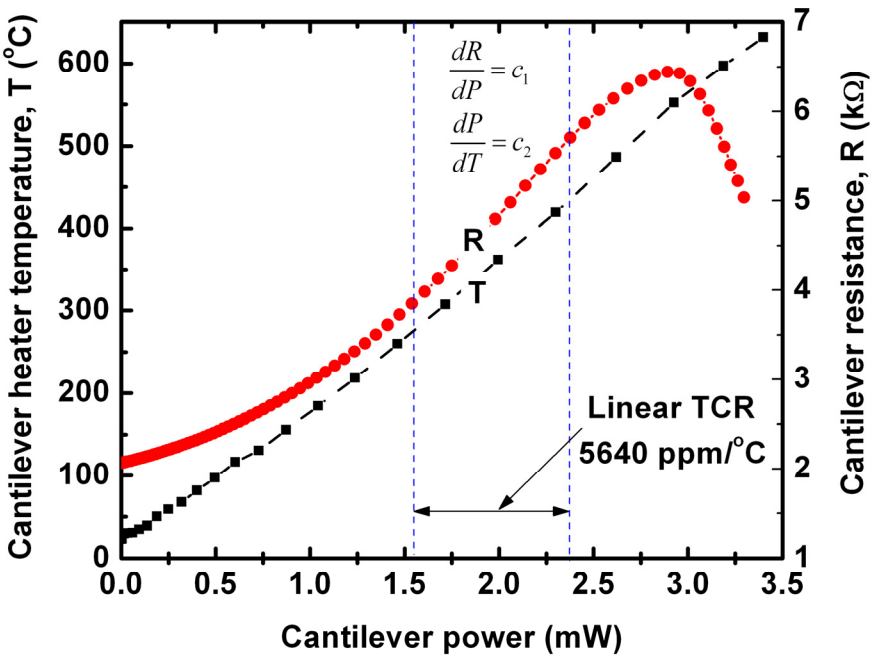


Figure 2.8 Cantilever resistance and heater temperature as functions of the cantilever power, measured using Raman Spectroscopy, where the temperature is based on Stokes peak position. Near room temperature, the cantilever resistance increases with temperature as carrier mobility decreases with increasing temperature. The cantilever electrical resistance drops steeply above 560 °C due to presence of thermally-generated intrinsic carriers. The heated cantilever has linear TCR of 5640 ppm/°C when the cantilever power is between 1.6 and 2.4 mW.

Using Raman spectroscopy, the cantilever heater temperature was calibrated with DC excitation. Figure 2.8 shows the cantilever resistance and heater temperature based on Stokes peak position as functions of the cantilever power. The tested cantilever was 100 μm long with two 10 μm wide legs and had an integrated heater of approximately 8 μm × 16 μm in size. The cantilever heater temperature increases almost linearly with the cantilever power as a result of a linear TCR of the cantilever in this regime. The heated cantilever has a linear TCR of 5640 ppm/°C when the cantilever power is between 1.6 and 2.4 mW. Near room temperature, the cantilever resistance increases with temperature, since the carrier mobility in the doped silicon cantilever decreases with temperature. However, the number of intrinsic carriers in the silicon increases with increasing temperature. At approximately 560 °C the thermally-generated intrinsic carriers become the dominant parameter affecting cantilever resistance and the resistance decreases sharply. This "thermal runaway" effect has been well studied for cantilever heating at steady-state [9]. Due to the thermal runaway at higher power levels, the heated cantilever can have the same electrical resistance at two different heater temperatures which precludes the use of resistance monitoring for temperature measurements. Therefore, using cantilever power as a measure of temperature has advantages over the resistance due to its one-to-one correspondence and linearity to the cantilever heater temperature.

Following cantilever heater temperature characterization, the temperature distribution from the cantilever heater along the legs was examined based on the Stokes peak position. Figure 2.9(a) compares temperatures at 6 specific locations with respect to the cantilever power. Each location shows linearity of the temperature to the cantilever

power. Figure 2.9(b) shows the temperature distribution which exponentially decays from the heater to the legs at different excitation voltages. The temperature gradient also increases as the voltage increases. The low doped heater shows more significant increases in both temperature and temperature gradient than the highly doped legs. However, it should be mentioned that temperatures measured from the Stokes peak position can contain stress information, resulting in added temperature uncertainty since the peak position is sensitive to both temperature and stress.

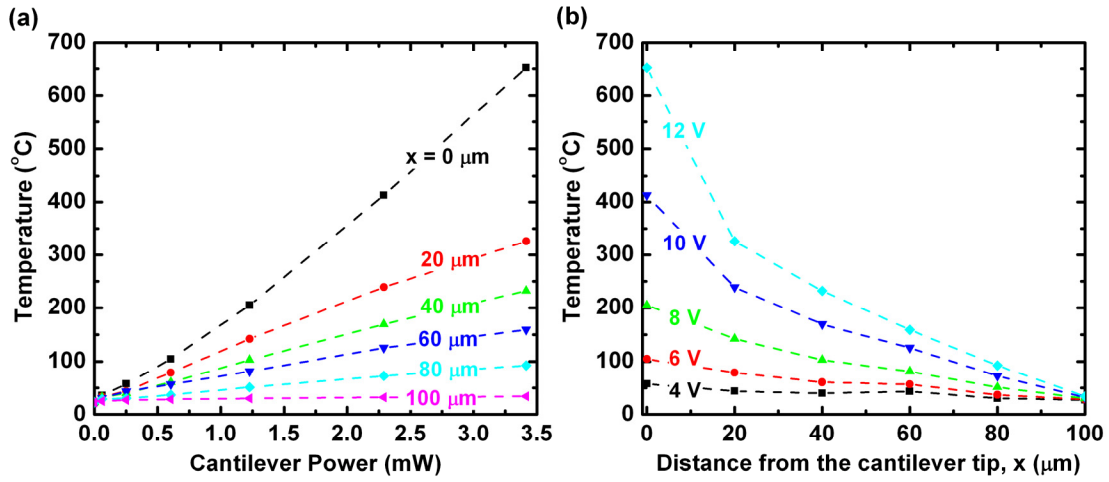


Figure 2.9 (a) Temperatures at 6 specific locations with respect to the cantilever power based on Stokes peak position. Each location shows linearity of the temperature to the cantilever power. (b) Temperature distribution which exponentially decays from the heater to the legs at different excitation voltages. Temperature gradient also increases as the driving voltage increases.

For all of the experiments described above, the electrical testing, the temperature of the substrate, upon where the heated cantilever was mounted, was kept constant at 300 K and at atmospheric pressure. However, the characterization results taken at these conditions are not universal. The heated cantilever needs to be characterized properly at every situation since changes in the environment such as pressure, temperature, and humidity can affect the cantilever response. Pressure effects have been studied to

determine the safe operating powers to prevent thermal damage [40]. Similarly, substrate temperature can change the heated cantilever responses dramatically.

A cryostat (SuperTran ST-200, Janis Research) was used to characterize the cantilever under various ambient temperatures. The cryostat used has a two-stage pumping mechanism including both a diaphragm fore pump and a turbo molecular pump. The temperature could be controlled between 80 and 700 K using liquid nitrogen and an electrical heater. The cantilever was mounted on a copper block and enclosed with a radiation shield before starting the two-stage pumping process. After the pressure reached the desired vacuum level ($10^{-4}$ mbar), a target temperature was set. Once the cantilever was in equilibrium with the substrate, various electrical testing could be performed.

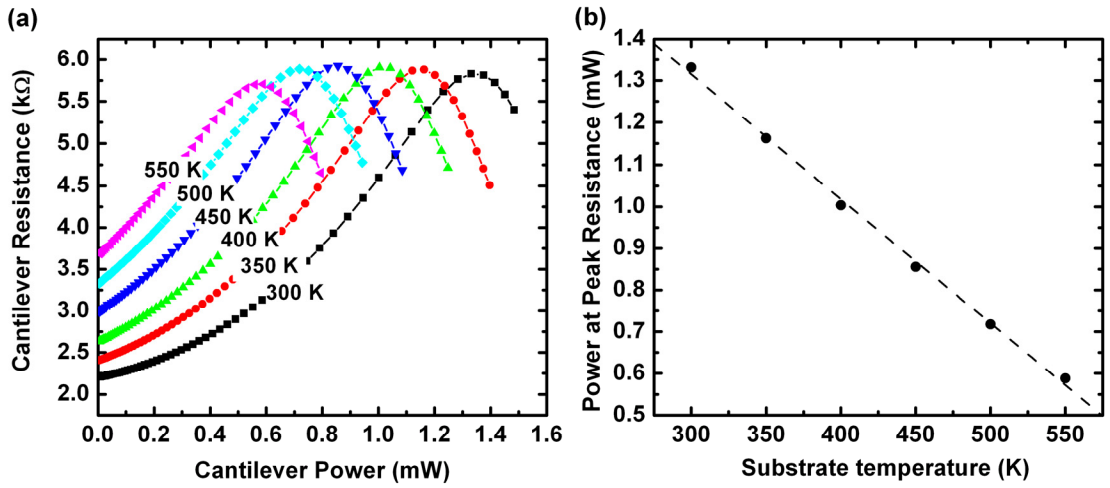


Figure 2.10 (a) Peak resistances are shifted to the lower power as the substrate temperature increases. (b) Linear relationship between the cantilever power at $R_{Peak}$ and the substrate temperature. Due to this linearity, the heated cantilever can act as a temperature sensor for the substrate.

First, the substrate was heated up to 550 K and DC characterization was performed. Then, same procedures were repeated at different substrate temperatures and the results were compared. Figure 2.10(a) shows that $R_{Peak}$ is shifted to lower power as

the substrate temperature increases. This is due to the reduced heat transfer potential between the cantilever and the substrate such that less power can be dissipated. In other words, reduced power is required to reach a specific heater temperature. Substrate cooling will shift the cantilever response in an opposite fashion but is not discussed here. Figure 2.10(b) shows the linear relationship between the cantilever power at $R_{Peak}$ and the substrate temperature. Due to this linearity, the heated cantilever can act as a temperature sensor for the substrate. Since conduction from the heated cantilever to the adjacent gas surroundings is negligible for the tested pressure, a linear temperature distribution from the heater along the legs can be approximated. The averaged thermal conductivity of the heated cantilever can be calculated from the measured power, cantilever geometry, and linear temperature distribution. The calculated conductivities are 127.3 and 107.8 W/mK when the substrate temperatures are 300 and 550 K, respectively. Although more fundamental approaches including boundary and impurity scatterings are required to obtain precise thermal conductivity of the heated cantilever, these estimations agree well with averaged conductivities of two thin doped silicon layers.

## 2.5 Mechanical Testing

In Raman spectroscopy, the position of the Stokes peak is sensitive to both temperature and stress but the line width of the Stokes peak depends only upon the temperature. Differences between the temperatures calculated by the Stokes peak position and the Stokes line width method can be used to simultaneously determine both temperature and stress ($\sigma$) given by

$$\sigma = \frac{\left(T_{Peak} - T_{FWHM}\right)\beta}{\gamma} \qquad (2.1)$$

where $\beta$ is the calibrated change of peak position with respect to temperature, $\gamma$ is the slope of the calibration of the peak position as a function of stress, and $T_{Peak}$ and $T_{FWHM}$ are temperatures based on Stokes peak position and Stokes line width, respectively. Based on white light interferometry measurements, bending stresses are believed to be the dominant mechanism inducing cantilever deformation. Thus, Raman stress calibrations from doped silicon bending tests were used to approximate the stress states in the cantilevers. These calibration experiments showed changes in the Stokes peak position of silicon corresponding to $\gamma = 0.00336$ cm$^{-1}$/MPa [22].

There are limitations in stress measurements using Raman spectroscopy for silicon based systems. Due to the degeneracy of the modes in a backscattering arrangement at its peak of 520.5 cm$^{-1}$ only limited information is available with regards to the stress tensor for any silicon material [41-43]. Consequently, it is necessary to make assumptions regarding the symmetrical nature of the present stress state (i.e. uniaxial, biaxial, hydrostatic) to quantitatively determine stress in silicon [44]. Therefore, pure quantitative data concerning the exact stress tensor is unobtainable with a 180° backscattering arrangement as employed here. Through comparison of the cantilever with an appropriate stress calibration, however, results can be gathered that are qualitatively correct while providing quantifiable data with a reasonable estimate of the actual stress.

Stress was measured along the length of the cantilever using both Stokes peak position and line width data with the method given by equation (2.1). Figure 2.11 shows

stress profiles for the top and bottom side of the heated cantilever, which displays a significant level of intrinsic tensile stress. Of note is the appreciably large magnitude of this stress on the top side of the device indicating a stress gradient through the thickness occurring most likely due to the ion implantation and annealing process. As power is applied, the stress gradient along the cantilever thickness reduces as on the top side tensile stress is reduced while the opposite trend occurs on the bottom side. In Figure 2.11(a) this is seen as under no load the top side of the cantilever exhibits 150 MPa of tensile stress at a location 150 μm away from the tip which is successively reduced with increasing levels of power until the stress is nearly 0 at 9V. Contrarily, in Figure 2.11(b) at a location 125 μm away from the tip, stress increases from nearly 0 at no applied load to almost 100 MPa at 9V.

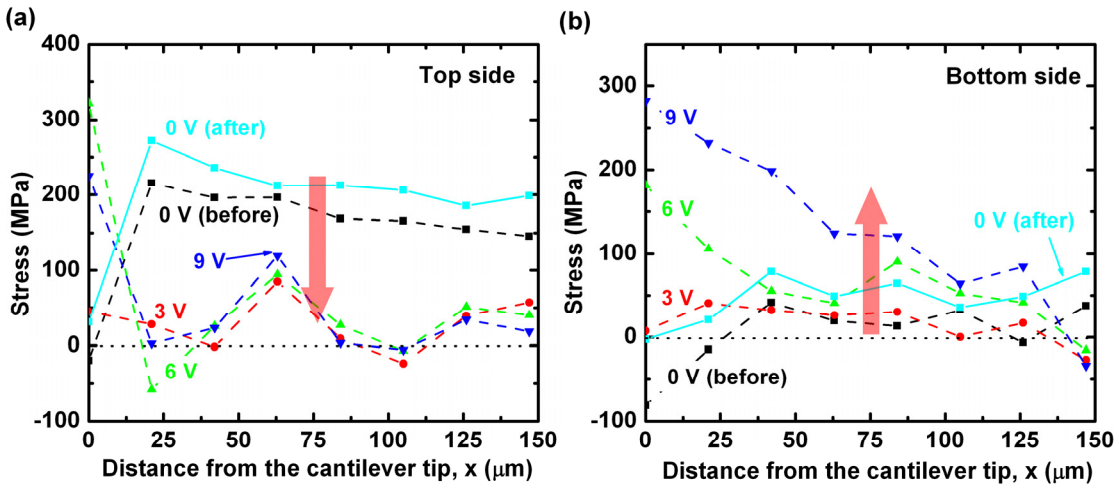


Figure 2.11 Stress profiles for (a) the top and (b) bottom side of the heated cantilever. A high level of intrinsic tensile stress is present in the system as seen under zero load. This tensile stress is then reduced with increasing voltage indicating compressive stresses that counteract this inherent portion. A contrary trend is seen on the bottom side of the cantilever as a much lower intrinsic tensile stress is seen.

The distinctly opposite trends in stress level on either side of the device indicate that a bending mechanism is at play during powered cantilever operation. This bending phenomenon implies that operation will cause a slight amount of curvature. This

curvature will be convex as viewed from the bottom of the device and must be accounted for in any force measurements, but also could be exploited in a sensor.

After these testings, both sides of the cantilever exhibited elevated levels of tensile stress under no load, indicating that the intrinsic stress in the cantilever changes with high heating. This suggests that operation of the cantilever results in irreversible changes in the device structure. The exact mechanism of these irreversibilities is unknown but most likely arises due to thermal annealing and diffusion of dopants. Measurements made directly on the tip of the cantilever may yield much different stress states than that observed in the cantilever legs due to both the extreme heating at this location and the complex stress states present at this location. Both of these effects severely enhance experimental uncertainty.

In AFM operation, the interaction between the cantilever tip and the underlying substrate is of great importance and requires precise measurement of mechanical properties of the cantilever such as spring constant and resonance frequency. The most common calibration technique is the thermal noise method, which exploits the equipartition theorem and relates thermal energy to the elastic potential energy of the cantilever [45]. In this technique, the spring constant is given by

$$k = \frac{k_B T_{cant}}{\langle x^2 \rangle} \tag{2.2}$$

where $k$ is the cantilever spring constant, $k_B$ is Boltzmann's constant, $T_{cant}$ is the cantilever temperature, and $\langle x^2 \rangle$ is the mean square deflection of the cantilever, which can be determined from integrating a simple harmonic oscillator model fit of the power spectrum of the cantilever thermal vibrations. We obtained the thermal noise spectrum using a

commercial AFM system (MFP-3D$^{TM}$, Asylum research). In order to convert the power spectrum from a photodiode voltage output to a physical displacement, the deflection sensitivity of the photodiode was obtained by taking a force-displacement curve on the AFM, and relating the measured displacement of the piezoelectric actuator to the measured deflection voltage from the photodiode. At room temperature, the measured resonant frequency was 157.6 kHz, as shown in the inset of Figure 2.12, and the spring constant was 1.9 N/m. Since the noise spectrum in Figure 2.12 is the power spectrum of the actual photodiode voltage, it includes anomalous spikes such as electrical noise and building vibration. With metal-coated commercial cantilevers, these effects are generally dominated by thermal vibration harmonics of the cantilever, but for our narrow silicon cantilevers, low photodiode sensitivity suppresses the thermal vibration resonant peak and inhibits detection of higher harmonics.

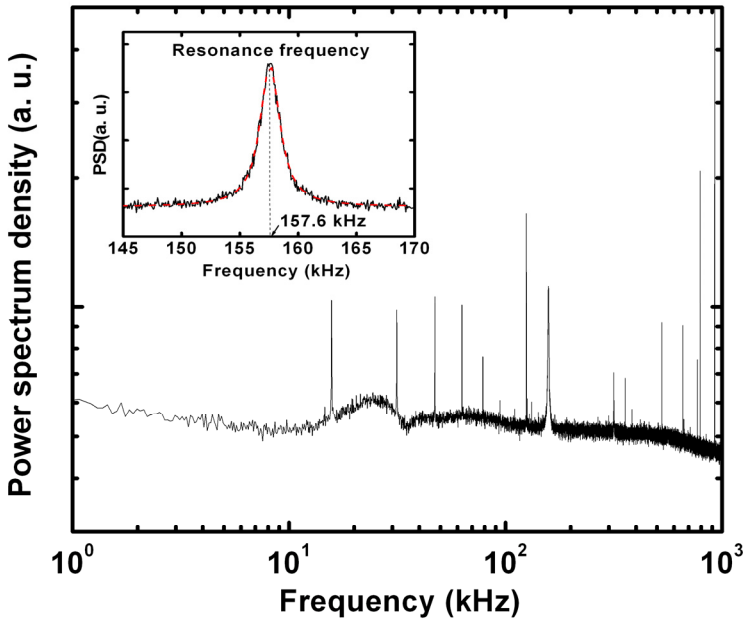


Figure 2.12 Thermal noise of the cantilever is measured and Fourier transformed to obtain a power spectrum. The power spectrum can be converted into an actual displacement of the cantilever by taking a force-displacement curve using AFM. The measured resonant frequency is 157.6 kHz at room temperature.

Finite element analysis was performed to compare the measured resonance frequency and spring constant with simulations and investigate high order vibration modes. The simulated resonance frequency and spring constant were 148.23 kHz and 1.43 N/m, respectively. The simulations give reasonable estimates of the measured values, but uncertainty in the cantilever's thickness and the low photodiode sensitivity limit the accuracy of the predictions and measurements. Additionally, the spring constant calculation only includes cantilever motion near the fundamental harmonic, neglecting vibrations at higher harmonics, which may cause this method to overpredict the spring constant.

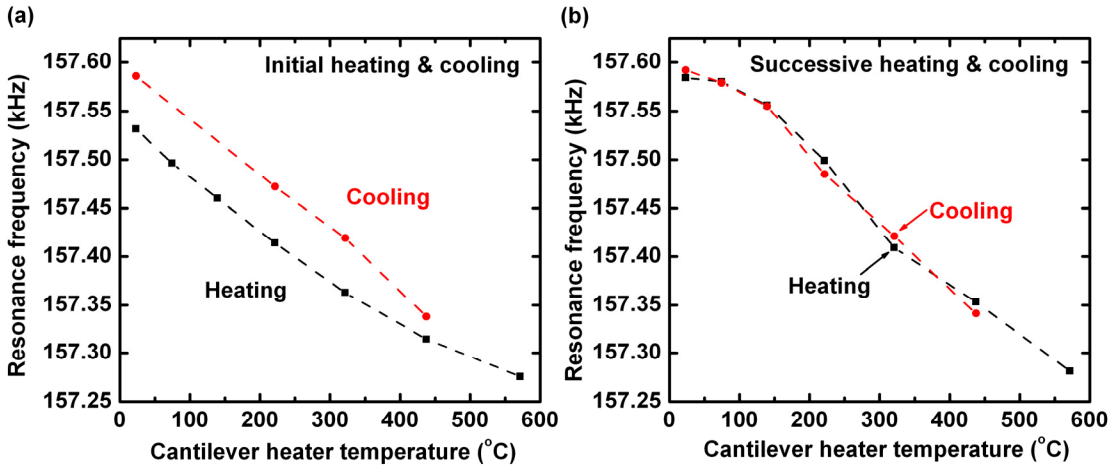


Figure 2.13 The elastic behavior of the heated cantilever is characterized as a function of temperature by measuring the thermal spectra of the cantilever during heating. (a) After initial heating, the resonant frequency increases during cooling. (b) Upon further heating, resonant frequency matches between heating and cooling curves.

Following mechanical characterization at room temperature, the elastic behavior of the heated cantilever was characterized as a function of temperature by measuring the thermal spectra of the cantilever during heating. As the cantilever temperature increased, the spectra demonstrated a monotonic decrease in cantilever resonant frequency. Significant hysteresis in the resonant frequency occurred during the first heating and

cooling cycle, shown in Figure 2.13(a). This hysteresis is likely due to desorption or decomposition of organic contaminants on the cantilever, resulting in a reduced cantilever mass and a higher resonant frequency. The desorbed mass can be estimated from

$$\left(\frac{1}{f_m^2}-\frac{1}{f_c^2}\right)\frac{k}{4\pi^2}=\delta m \qquad (2.3)$$

where $f_c$ is the resonant frequency of the clean cantilever, $k$ is the cantilever spring constant, $f_m$ is the resonant frequency of the cantilever with adsorbed mass, and $\delta m$ is the desorbed mass [46]. Equation (2.3) is for point mass desorption off the end of the cantilever, and although some desorption occurs off the cantilever legs as well, Figure 2.13(a) shows that below 450 °C, the difference in resonant frequency between heating and cooling curves is relatively constant at approximately 55 Hz. This implies that most of the desorption occurred when the cantilever temperature rose to 450 °C. Because the temperature decreases along the length of the cantilever legs, if a significant amount of mass were desorbing off the cantilever legs, the change in the resonant frequency should be gradual as the temperature required for desorption gradually moves farther down the length of the legs. Using the obtained spring constant at room temperature in combination with the room temperature values for resonant frequency, equation (2.3) estimates the desorbed mass as approximately 1.3 fg.

The resonant frequency of an unloaded rectangular vibrating beam is given by [47]

$$\varpi=\sqrt{\frac{k}{m_{eff}}}\approx 1.021\frac{t}{L^2}\sqrt{\frac{E}{\rho}} \qquad (2.4)$$

where $k = 0.25Ewt^3 / L^3$ is the spring constant of a rectangular beam, $m_{eff} = 0.24m$ is the effective mass of the cantilever, $t$ is the cantilever thickness, $L$ is its length, $E$ is the elastic modulus of the beam, and $\rho$ is the mass density. There are two primary mechanisms by which the resonant frequency of the cantilever might exhibit temperature-dependence. First, thermal expansion can induce changes in the physical dimensions of the cantilever, and second, heating can reduce the elastic modulus. For crystalline silicon, the effect of heating on the elastic modulus is the dominant effect. The elastic modulus of silicon is expected to decrease with temperature according to

$$E(T) = E_0 - BT \exp\left(-\frac{T_0}{T}\right) \qquad (2.5)$$

where $E_0$ is young's modulus at 0 K, and $B$ and $T_0$ are constants [48]. Because the temperature is not uniform along the legs of the cantilever, the elastic modulus is not uniform either. Thus, a quantitative comparison between equation (2.5) and the measured resonant frequency data is difficult. Qualitatively, since the resonant frequency is proportional to the square root of the elastic modulus, the frequency should decrease with the modulus as temperature increases, and this expected reduction occurs, as shown in Figure 2.13(b).

The non-uniform temperature distribution along the legs prevented estimate of the cantilever spring constant while heated. Figure 2.14 shows the measured value for $\langle x^2 \rangle$ during cantilever heating. As the cantilever temperature increased, the thermal energy increased and the elastic modulus decreased, both of which contributed to the observed increase in $\langle x^2 \rangle$. However, equation (2.2) could not be used to calculate the cantilever

spring constant because the nonuniform cantilever temperature makes $T$ unable to be defined.

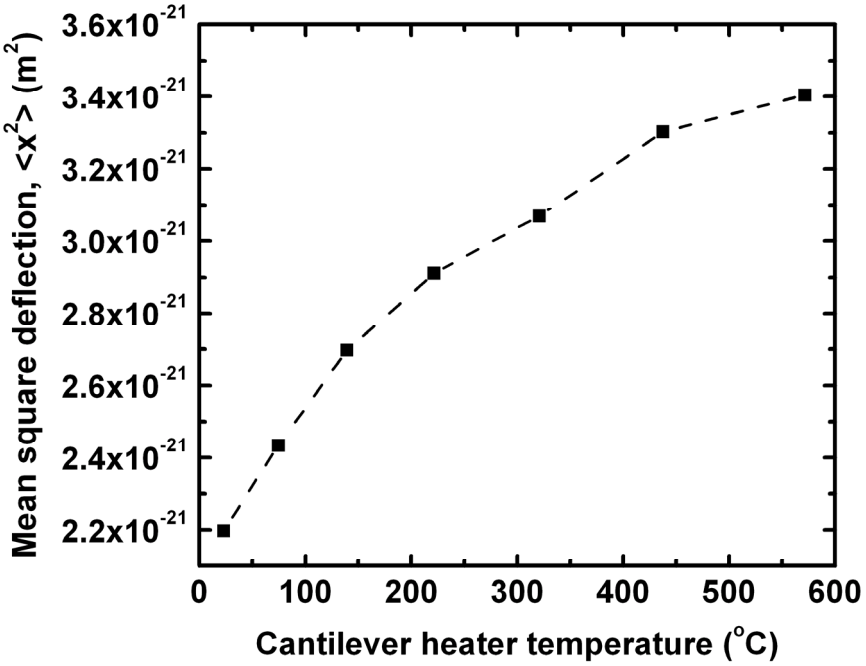


Figure 2.14 As the cantilever temperature increases, the average harmonic displacement also increases, in accordance with both increasing thermal energy and decreasing spring constant.

Figure 2.15 shows the effect of various estimates of the thermal energy, $k_BT$ for use in calculating the cantilever spring constant according to equation (2.2). Since the spring constant should decrease as the elastic modulus decreases at increasing temperature, Figure 2.15 shows that estimates close to ambient are the only estimates that yield the expected spring constant reduction. We conclude that the thermal energy in the cantilever was much closer to that of ambient thermal energy, $k_BT_0$ than the thermal energy calculated using the heater temperature, $k_BT_H$. This phenomenon can be understood by considering that the mechanical energy in the oscillating cantilever is proportional to the square of the bending stress, and the bending stress is maximal at the base of the cantilever where the temperature was close to ambient.

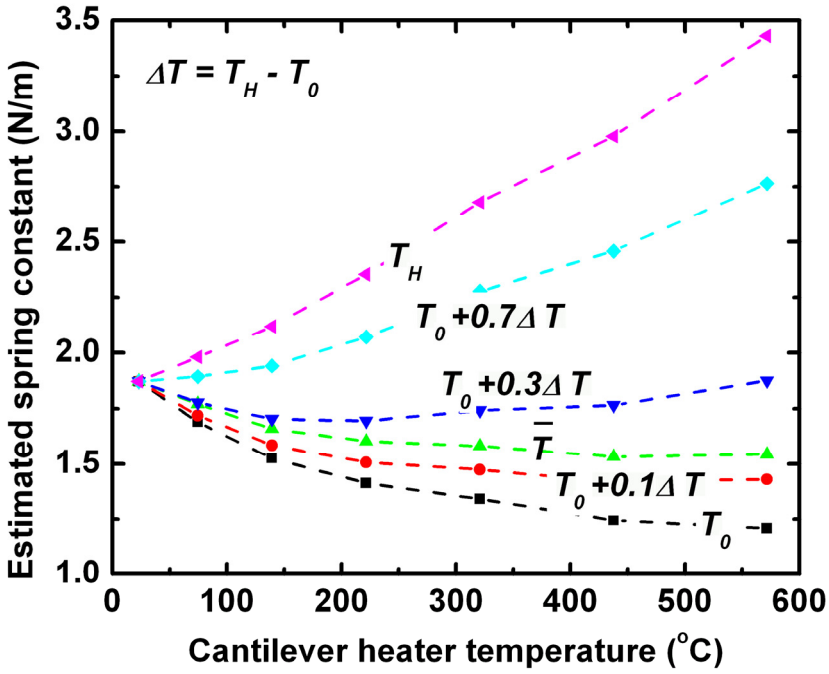


Figure 2.15 Spring constant calculated using various estimates for the temperature in the thermal energy. The temperatures $T_H$ , $T_0$ , and $\bar{T}$ correspond to the cantilever heater temperature, the ambient temperature, and the stress integral average temperature, respectively. The only estimates of the thermal energy of the cantilever that yield the expected reduction in spring constant with increasing temperature are those using a temperature much closer to room temperature than to the heater temperature, including the stress integral average temperature.

To improve the estimate for thermal energy, an integral-average temperature based on the bending stress can be defined by

$$\bar{T} = \frac{\int_V T(x)\sigma(x,y)d\mathrm{V}}{\int_V \sigma(x,y)d\mathrm{V}} = \frac{3}{L^3}\int_0^L T(x)x^2 dx \qquad (2.6)$$

where the integration is over the volume of the cantilever V, $x$ is measured from the heater end of the cantilever, $L$ is the length of the cantilever, $T(x)$ is the temperature distribution along the legs of the cantilever and is taken from the data in Figure 2.9, and $\sigma(x,y)$ is the bending stress profile in the cantilever with point loading at the end of the cantilever assumed, in accordance with the simple harmonic oscillator behavior assumed

in equation (2.2). Figure 2.15 shows that when this average temperature is used for determining the spring constant with equation (2.2), the expected reduction in the cantilever spring constant emerges. Thus, equation (2.6) presents a method of estimating the cantilever spring constant during operation at elevated temperature.

## 2.6 Summary and Conclusions

This chapter reports electrical, thermal, and mechanical characterization of heated AFM cantilevers to extend their functionality beyond thermomechanical data storage. These measurements examine the complex temperature-dependent electrical characteristics of the heated cantilever and suggest how to operate them with DC, pulse, and AC excitation. Using Raman spectroscopy, localized temperature and stress were simultaneously examined with 1 μm resolution. The temperature calibration allows measurement of heat flux from the heated cantilever to the nearby environment. Thermally induced stresses were qualitatively examined from differences in temperature measured by Stokes peak position and Stokes line width methods. Mechanical characterization was performed using thermal noise spectrum and the elastic behavior of the heated cantilever was characterized as a function of temperature by measuring the resonant frequency of the cantilever during heating. Results reported in this chapter facilitate new applications of the heated cantilever such as nano-calorimetry, mass detection, and nanolithography.

## 2.7 References


[1] W. P. King, T. W. Kenny, K. E. Goodson, G. L. W. Cross, M. Despont, U. T. Dürig, H. Rothuizen, G. Binnig, and P. Vettiger, "Design of atomic force microscope cantilevers for combined thermomechanical writing and thermal reading in array operation," *Journal of Microelectromechanical Systems*, vol. 11, pp. 765-774, 2002.

[2] P. Vettiger, G. Cross, M. Despont, U. Drechsler, U. Dürig, B. Gotsmann, W. Häberle, M. Lantz, H. Rothuizen, R. Stutz, and G. Binnig, "The "Millipede"-nanotechnology entering data storage," *IEEE Transactions on Nanotechnology*, vol. 1, pp. 39-64, 2002.

[3] P. Vettiger and G. Binnig, "The nanodrive project," *Scientific American*, vol. 288, pp. 46-53, 2003.

[4] G. Binnig, M. Despont, U. Drechsler, W. Häberle, M. Lutwyche, P. Vettiger, H. J. Mamin, B. W. Chui, and T. W. Kenny, "Ultrahigh-density atomic force microscopy data storage with erase capability," *Applied Physics Letters*, vol. 76, pp. 1329-1331, 1999.

[5] P. Vettiger, J. Brugger, M. Despont, U. Drechsler, U. Dürig, W. Häberle, M. Lutwyche, H. Rothuizen, R. Stutz, R. Widmer, and G. Binnig, "Ultrahigh density, high-data-rate NEMS-based AFM data storage system," *Microelectronic Engineering*, vol. 46, pp. 11-17, 1999.

[6] M. Lutwyche, C. Andreoli, G. Binnig, J. Brugger, U. Drechsler, W. Häberle, H. Rohrer, H. Rothuizen, P. Vettiger, G. Yaralioglu, and C. Quate, "5 × 5 2D AFM cantilever arrays a first step towards a Terabit storage device," *Sensors and Actuators, A*, vol. 73, pp. 89-94, 1999.

[7] M. I. Lutwyche, M. Despont, U. Drechsler, U. Dürig, W. Hablerle, H. Rothuizen, R. Stutz, R. Widmer, G. K. Binnig, and P. Vettiger, "Highly parallel data storage system based on scanning probe arrays," *Applied Physics Letters*, vol. 77, pp. 3299-3301, 2000.

[8] B. W. Chui, T. D. Stowe, Y. S. Ju, K. E. Goodson, T. W. Kenny, H. J. Mamin, B. D. Terris, and R. P. Ried, "Low-stiffness silicon cantilever with integrated heaters and piezoresistive sensors for high-density data storage," *Journal of Microelectromechanical Systems*, vol. 7, pp. 69-78, 1998.

[9] M. Despont, J. Brugger, U. Drechsler, U. Dürig, W. Häberle, M. Lutwyche, H. Rothuizen, R. Stutz, R. Widmer, H. Rohrer, G. K. Binnig, and P. Vettiger, "VLSI-NEMS chip for parallel AFM data storage," *Sensors and Actuators, A*, vol. 80, pp. 100-107, 2000.

[10] P. E. Sheehan, L. J. Whitman, W. P. King, and B. A. Nelson, "Nanoscale deposition of solid inks via thermal dip pen nanolithography," *Applied Physics Letters*, vol. 85, pp. 1589-1591, 2004.

[11] B. A. Nelson, W. P. King, A. Laracuente, P. E. Sheehan, and L. J. Whitman, "Direct deposition of continuous metal nanostructures by thermal dip-pen nanolithography," *Applied Physics Letters*, vol. 88, pp. 033104, 2006.

[12] E. O. Sunden, T. L. Wright, J. Lee, S. A. Graham, and W. P. King, "Room temperature chemical vapor deposition and mass detection on a heated atomic force microscope cantilever," *Applied Physics Letters*, vol. 88, 033107, 2006.

[13] W. P. King, T. W. Kenny, and K. E. Goodson, "Comparison of thermal and piezoresistive sensing approaches for atomic force microscopy topography measurements," *Applied Physics Letters*, vol. 85, pp. 2086-2088, 2004.

[14] W. P. King, "Design analysis of heated atomic force microscope cantilevers for nanotopography measurements," *Journal of Micromechanics and Microengineering*, vol. 15, pp. 2441-2448, 2005.

[15] B. Gotsmann and U. Dürig, "Thermally activated nanowear modes of a polymer surface induced by a heated tip," *Langmuir*, vol. 20, pp. 1495-1500, 2004.

[16] B. Gotsmann and U. Dürig, "Experimental observation of attractive and repulsive thermal forces on microcantilevers," *Applied Physics Letters*, vol. 87, pp. 194102, 2005.

[17] B. W. Chui, M. Asheghi, Y. S. Ju, K. E. Goodson, T. W. Kenny, and H. J. Mamin, "Intrinsic-carrier thermal runaway in silicon microcantilevers," *Microscale Thermophysical Engineering*, vol. 3, pp. 217-228, 1999.

[18] M. A. Lantz, G. K. Binnig, M. Despont, and U. Drechsler, "A micromechanical thermal displacement sensor with nanometre resolution," *Nanotechnology*, vol. 16, pp. 1089-1094, 2005.

[19] T. Thundat, G. Y. Chen, R. J. Warmack, D. P. Allison, and E. A. Wachter, "Vapor detection using resonating microcantilevers," *Analytical Chemistry*, vol. 67, pp. 519-521, 1995.

[20] L. A. Pinnaduwage, A. Gehl, D. L. Hedden, G. Muralidharan, T. Thundat, R. T. Lareau, T. Sulchek, L. Manning, B. Rogers, M. Jones, and J. D. Adams, "A microsensor for trinitrotoluene vapour," *Nature*, vol. 425, pp. 474, 2003.

[21] L. A. Pinnaduwage, A. Wig, D. L. Hedden, A. Gehl, D. Yi, T. Thundat, and R. T. Lareau, "Detection of trinitrotoluene via deflagration on a microcantilever," *Journal of Applied Physics*, vol. 95, pp. 5871-5875, 2004.

[22] M. R. Abel, "Thermal metrology of polysilicon MEMS using Raman spectroscopy," M. S. Thesis, Woodruff school of Mech. Eng., Georgia Inst. of Tech., Atlanta, GA, 2005.

[23] S. P. Kearney, L. M. Phinney, and M. S. Baker, "Spatially resolved temperature mapping of electro-thermal actuators by surface Raman scattering," *Journal of Microelectromechanical Systems*, vol. 15, pp. 314-321, 2006.

[24] M. R. Abel, T. L. Wright, W. P. King, and S. Graham, "Thermal metrology of silicon micro-structures using Raman spectroscopy," *IEEE Transactions on Component and Packaging Technologies*, in press.

[25] T. L. Wright, "Design and fabrication of heated atomic force microscope cantilevers," M. S. Thesis, Woodruff school of Mech. Eng., Georgia Inst. of Tech., Atlanta, GA, 2005.

[26] T. S. Ravi, R. B. Marcus, and D. Liu, "Oxidation sharpening of silicon tips," *Journal of Vacuum Science and Technology B*, vol. 9, pp. 2733-2737, 1991.

[27] W. P. King, T. W. Kenny, K. E. Goodson, G. Cross, M. Despont, U. Dürig, H. Rothuizen, G. K. Binnig, and P. Vettiger, "Atomic force microscope cantilevers for combined thermomechanical data writing and reading," *Applied Physics Letters*, vol. 78, pp. 1300-1302, 2001.

[28] W. P. King, T. W. Kenny, K. E. Goodson, G. L. W. Cross, M. Despont, U. Dürig, H. Rothuizen, G. Binnig, and P. Vettiger, "Design of atomic force microscope cantilevers for combined thermomechanical writing and thermal reading in array operation," *Journal of Microelectromechanical Systems*, vol. 11, pp. 765-774, 2002.

[29] N. Masters, W. Ye, and W. P. King, "The Impact of sub-continuum gas conduction on the sensitivity of heated Atomic force microscope cantilevers," *Physics of Fluids*, vol. 17, 100615, 2005.

[30] K. Park, J. Lee, Z. M. Zhang, and W. P. King, "Frequency-dependent electrical and thermal response of heated atomic force microscope cantilevers," *Journal of Microelectromechanical Systems*, in press.

[31] J. B. Cui, K. Amtmann, J. Ristein, and L. Ley, "Noncontact temperature measurements of diamond by Raman scattering spectroscopy," *Journal of Applied Physics*, vol. 83, pp. 7929-7933, 1998.

[32] R. Ostermeir, K. Brunner, G. Abstreiter, and W. Weber, "Temperature distribution in Si-MOSFET's studied by Micro Raman spectroscopy," *IEEE Transactions on Electron Devices*, vol. 39, pp. 858-863, 1992.

[33] S. Perichon, V. Lysenko, B. Remakki, D. Barbier, and B. Champagnon, "Measurement of porous silicon thermal conductivity by Micro-Raman scattering," *Journal of Applied Physics*, vol. 86, pp. 4700-4702, 1999.

[34] G. Viera, S. Huet, and L. Boufendi, "Crystal size and temperature measurements in nanostructured silicon using Raman spectroscopy," *Journal of Applied Physics*, vol. 90, pp. 4175-4183, 2001.

[35] H. Brugger and P. W. Epperlein, "Mapping of local temperatures on mirrors of GaAS/AlGaAs laser diode," *Applied Physics Letters*, vol. 56, pp. 1049-1051, 1990.

[36] P. W. Epperlein, G. L. Bona, and P. Roentgen, "Local mirror temperatures of red-emitting," *Applied Physics Letters*, vol. 60, pp. 680-682, 1992.

[37] A. Chitnis, J. Sun, V. Mandavilli, R. Pachipulusu, S. Wu, M. Gaevski, V. Adivarahan, J. Zhang, M. A. Khan, A. Sarua, and M. Kuball, "Self-heating effects at high pump currents in deep ultraviolet light-emitting diodes at 324 nm," *Applied Physics Letters*, vol. 81, pp. 3491-3493, 2002.

[38] M. Kuball, S. Rajasingam, A. Sarua, M. Uren, T. Martin, B. T. Hughes, K. Hilton, and R. Balmer, "Measurement of temperature distribution in multifinger AlGaN/GaN heterostructure field-effect transistors using micro-Raman spectroscopy," *Applied Physics Letters*, vol. 82, pp. 124-126, 2003.

[39] M. Bowden and D. Gardiner, "High resolution Raman shift and bandwidth images of stressed silicon," *Internet Journal of Vibrational Spectroscopy*, vol. 2(section 6), 1998.

[40] J. Lee, T. L. Wright, M. R. Abel, E. O. Sunden, A. Marchenkov, S. Graham, and W. P. King, "Thermal conduction from microcantilever heaters in partial vacuum," *Journal of Applied Physics*, vol. 101, pp. 014906, 2007.

[41] I. D. Wolf, H. E. Maes, and S. K. Jones, "Stress measurements in silicon devices through Raman spectroscopy: Bridging the gap between theory and experiment," *Journal of Applied Physics*, vol. 79, pp. 7148-7156, 1996.

[42] I. D. Wolf, "Micro-Raman spectroscopy to study local mechanical stress in silicon integrated circuits," *Semiconductor Science and Technology*, pp. 139, 1996.

[43] E. Bonera, M. Fanciulli, and D. N. Batchelder, "Raman spectroscopy for a micrometric and tensional analysis of stress in silicon," *Applied Physics Letters*, vol. 81, pp. 3377-3379, 2002.

[44] E. Bonera, M. Fanciulli, and D. N. Batchelder, "Combining high resolution and tensional analysis in Raman stress measurements of silicon," *Journal of Applied Physics*, vol. 94, pp. 2729-2740, 2003.

[45] J. L. Hutter and J. Bechhoefer, "Calibration of atomic-force microscope tips," *Review of Scientific Instruments*, vol. 64, pp. 1869-1873, 1993.

[46] R. Berger, H. P. Lang, C. Gerber, J. K. Gimzewski, J. H. Fabian, L. Scandella, E. Meyer, and H.-J. Guntherodt, "Micromechanical thermogravimetry," *Chemical Physics Letters*, vol. 294, pp. 363-369, 1998.

[47] D. Sarid, *Scanning force microscopy*, Rev. ed.: Oxford University Press, 1994.

[48] U. Gysin, S. Rast, P. Ruff, E. Meyer, D. W. Lee, P. Vettiger, and C. Gerber, "Temperature dependence of the force sensitivity of silicon cantilevers," *Physical Review B*, vol. 69, 045403, 2004.

# CHAPTER 3

# MICROCANTILEVER HOTPLATES: DESIGN, FABRICATION, AND CHARACTERIZATION

## 3.1 Introduction

Microcantilevers offer outstanding opportunities for bio/chemical sensors, as they can be highly sensitive to specific bio/chemical analytes [1,2], are relatively easy to fabricate and use, and can interface with existing laboratory equipments and integrated microfluidic handling systems. In addition, microhotplates have been shown to be extremely useful for calorimetry [3,4] and chemical sensing [5]. While several studies have shown that microcantilevers can be fabricated with internal resistive heaters [6,7], little work has been done to converge microcantilevers with microhotplates for sensing applications. This chapter describes microcantilever-heaters for microhotplate applications having well-characterized temperature uniformity and sub-ms response time.

Microfabricated hotplates have previously been used for various sensing applications, including a Pirani gauge [8], a gas sensor [9], and a flow-rate sensor [10]. In some cases, the methods or materials of microsensor fabrication limited its performance. The main design considerations for micro hotplates are thermal isolation and temperature uniformity that can be achieved through free standing heatable microstructures, which are either bridges or cantilevers. To further minimize heat conduction through mechanical links, porous silicon has been introduced for low power

micro hotplate arrays [11]. Micro hotplates made from thin-film platinum heater-thermometers [12] could not be integrated with on-chip circuitry since platinum is not compatible to conventional silicon microelectronics fabrication. Micro hotplates made from polysilicon [13] have poor long term stability at high temperatures since the grain boundaries of polysilicon are highly reactive. Microcantilever heaters made from doped single-crystal silicon overcome these drawbacks, as integrated electronics could be produced in the same silicon layer, and because they can be cycled many times to temperatures above 800 ºC [14]. Remarkably, microcantilever heaters made from doped single-crystal silicon have a TCR that can exceed that of platinum by a factor of 2 [14], and so their temperature sensitivity can exceed that of platinum thermometers.

Microcantilevers with internal heaters have been extensively studied for their applications to thermomechanical data storage [15,16], nanomanufacturing [17,18], and fundamental thermophysical measurements [19,20]. Silicon cantilevers are capable of achieving temperatures that exceed 1000 ºC [14] and heating times on the order of 10 – 50 μs [6,14]. Silicon cantilevers capable of high temperature heating have been shown to control the local growth of carbon nanostructures [21] and enable new thermal analysis measurements on novel materials [22]. However, the cantilevers have not significantly matured beyond their original design for data storage. In particular, the spatial and temporal temperature characteristics of these cantilevers have been specifically tailored for data storage and have not been optimized for any other application.

The capability to heat microcantilevers is useful for cantilever-based sensors. When heated with an external laser, microcantilever arrays used for biochemical sensing yielded useful information about temperature-dependant molecular binding events [23].

Recently, heatable microcantilevers have demonstrated explosives detection with part-per-trillion sensitivity [24]. The cantilever heating caused deflagration of the chemical adsorbed to the cantilever, which in turn induced measurable cantilever deflection. For these experiments, commercial piezoresisitve cantilevers were used to provide heating and laser and photodiode were used to detect induced deflection. However, the piezoresistive cantilever was not designed to provide a highly uniform temperature to the analyte, nor was it designed for fast response time, with temperature rise near 1 ms. While there has been considerable progress on microcantilevers with integrated heaters, and a demonstrated need for microcantilever sensors with integrated heating elements, no work has been published that has designed cantilever hotplates specifically for cantilever-based sensing.

This chapter describes the design, fabrication, and detailed characterization of microcantilever hotplates intended for bio/chemical sensing applications. Six different cantilever designs have integrated heaters of various shapes. The cantilevers have a time constant in the sub-ms range and can reach temperatures that exceed 1000 ºC with high temperature uniformity.

## 3.2 Design and Fabrication

The microcantilever hotplates were made of doped silicon and have an integrated solid-state heater, similar to cantilevers designed for data storage [6]. The major design requirements for the microcantilever hotplates were temperature uniformity within 20 % of the average temperature in the cantilever and a thermal response time < 1 ms. Furthermore, the target requirements for the microcantilever hotplates were to have

electrical resistance < 1 kΩ, power consumption < 100 mW, and mechanical resonance frequency 10 – 50 kHz. These design requirements summarized in Table 3.1 were chosen to allow simple interface with conventional laboratory electronics and commercial AFM systems.

Table 3.1 Electrical, thermal, and mechanical design requirements.

| | |
|---|---|
| Electrical resistance | $R < 1$ kΩ |
| Power consumption | $P < 100$ mW |
| Resonance frequency | $f$ : 10 – 50 kHz |
| Spring constant | $k$ : 0.1 N/m |
| Time constant | $\tau$ < 1ms |
| Max. temperature | $T_{max} \sim 1000$ °C |

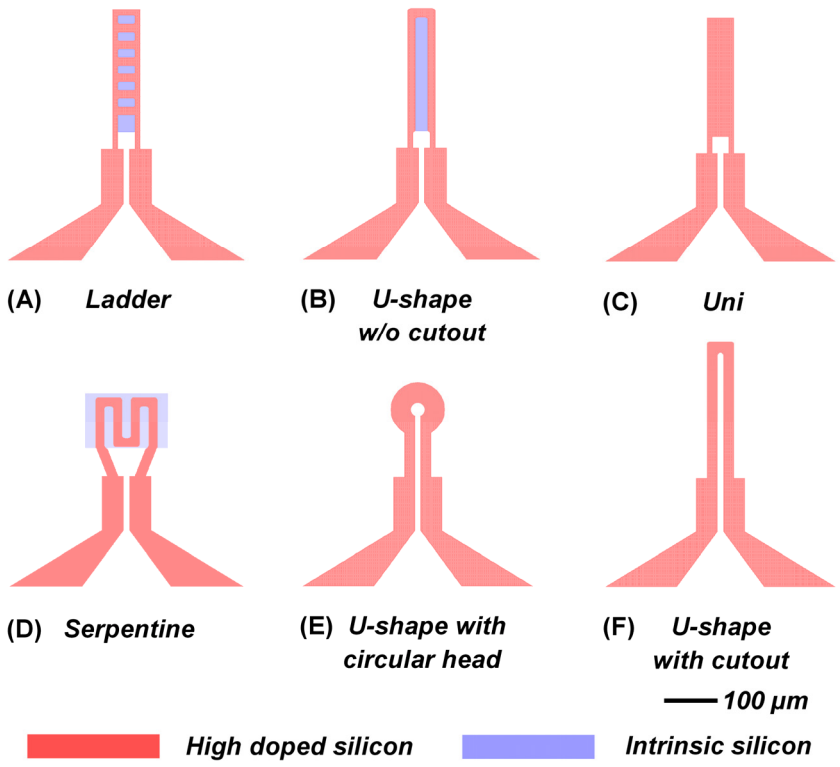


Figure 3.1 Six different designs for the cantilever type micro hotplate. Each type has different shape and different doping area. The two regions of phosphorous doped silicon are intrinsic silicon and doped silicon.

Figure 3.1 shows six different designs for the microcantilever hotplates. Each type has a different shape or different doping area to test the different temperature profiles that could be achieved within the cantilever. Cantilever physical dimensions were selected to meet the requirements for electrical resistance and resonance frequency. The nominal cantilever dimensions were 250 μm length, 50 μm width, and 1 μm thickness. The cantilevers were made from single-crystal silicon, where the silicon was patterned and phosphorous doped in some regions to make it electrically active. Figure 3.1 shows the cantilever designs including the regions of phosphorous doping and the regions of intrinsic silicon. Type A is the "Ladder" structure, where there are several doped silicon resistors in parallel to achieve distributed heating in the cantilever with a low electrical resistance. Type B is "U-shape without cutout" which has a "U" shaped electrical path but is mechanically a solid rectangle. Type C is called "Uni" since it has one rectangular heater. Type D has a serpentine electrical path to achieve uniform temperature in the rectangular heater platform. Type E and F are "U-shaped" but type E has a circular head to increase the effective sensing area. F is mechanically "U" shaped with the silicon removed between the two legs.

Figure 3.2 shows the major fabrication steps to produce the microcantilever hotplates. The fabrication process started with an SOI wafer of orientation <100>, where the buried oxide layer was 1 μm thick and the silicon device layer was 5 μm thick. The silicon device layer had a native doping of phosphorous at $1\times10^{15}cm^{-3}$ with a resistivity of approximately 4 Ω-cm. The first step was to etch 1 μm of the device layer without a mask layer to reduce the overall device layer thickness. Then, photolithography

patterned positive photoresist (Shipley 1827) to define anchor structures that connect the cantilever to the silicon handle.

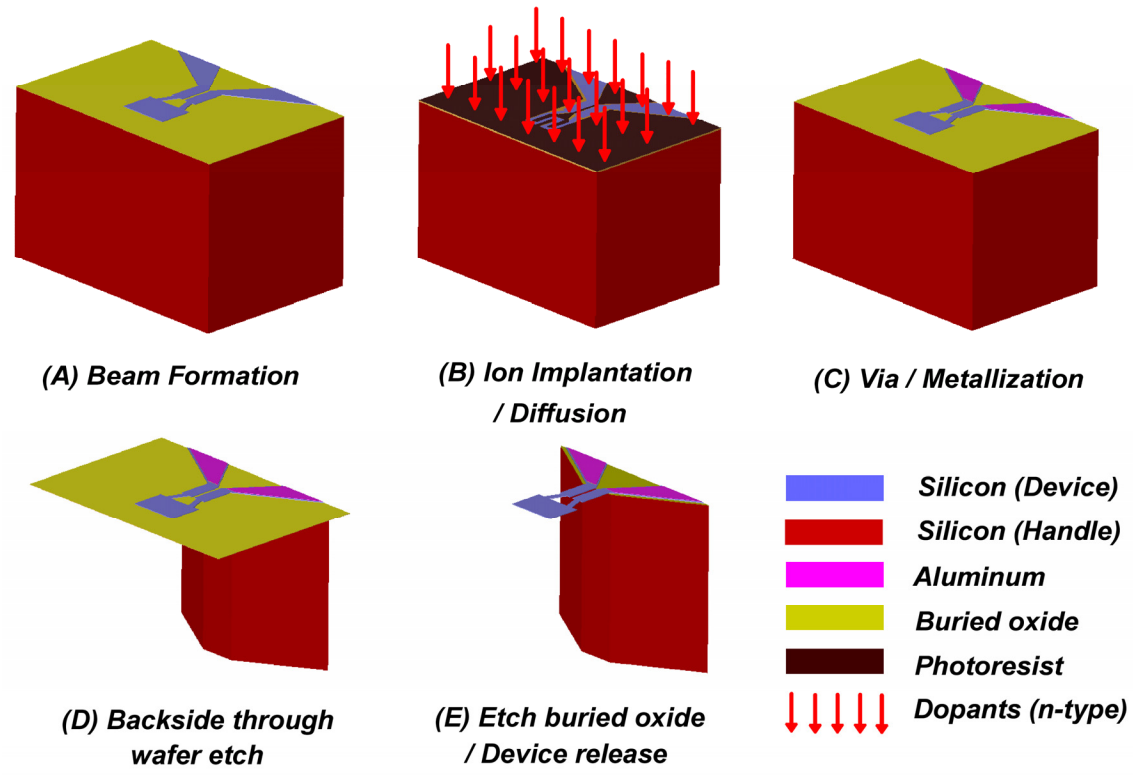


Figure 3.2 Five major fabrication steps to produce the microcantilever hotplates.

The processed wafer was etched 3 μm using a fluorine-based Bosch process in an inductively coupled plasma (ICP) etcher. The local etch rate and etch uniformity were characterized using a stylus profilometer (KLA P-15, Tencor). At wafer level, the etch depth was uniform to within 4 %, which is not significant compared to the device layer thickness tolerance of ± 0.5 μm. The same photolithographic and etching processes were repeated to define cantilever beam structures until the buried thermal oxide layer was fully exposed in the areas without photoresist coverage. Next, photolithography defined photoresist (Shipley 1827) as a mask for ion implantation. The exposed device layer regions were doped to $2.51\times10^{16}$ $cm^{-2}$ during ion implantation at 200 keV. A high-

temperature diffusion step was performed for 6 hours at 1000 ºC in order to distribute the implanted dopant more evenly within the device layer. Diffusion simulations predicted that the resulting doping concentration in the silicon cantilever was $10^{20}$ $cm^{-3}$. After metallization and lift-off to define aluminum contacts, the backside of the handle wafer was etched by the ICP etcher until the buried oxide layer was exposed. The cantilevers were finally released by a 15 s dip in 49% hydrofluoric acid. More detailed fabrication processes can be found in Appendix A.

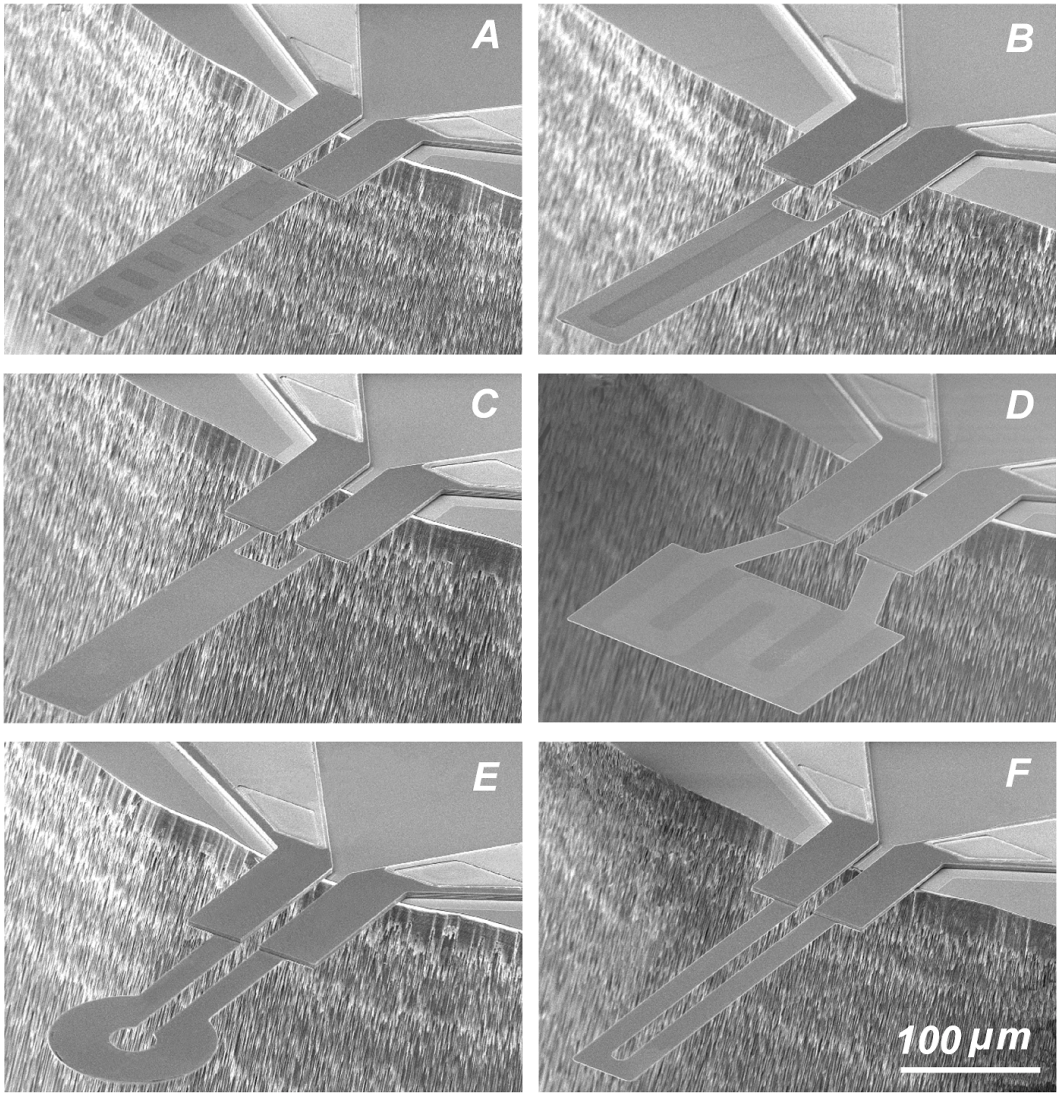


Figure 3.3 SEM images of the fabricated devices. The cantilevers were generally flat, indicating low intrinsic stress in the silicon device layer after processing. The traces of doped silicon can be seen in some of the SEMs.

Figure 3.3 shows SEM images of the fabricated devices. The cantilevers were generally flat, indicating low intrinsic stress in the silicon device layer after processing. The traces of doped silicon can be seen in some of the SEM images.

### 3.3 Cantilever Characterization

After the fabrication, thermal, electrical, and mechanical characterizations were performed using previously developed techniques [14,25]. For the electrical testing, the cantilever was configured in series with a precision 1 kΩ power resistor, in a simple bridge circuit that served to protect the cantilever from thermal runaway [14,26]. The circuit was excited with DC voltage and short electrical pulses, in order to test the cantilever steady state and transient responses. Figure 3.4 shows the cantilever DC response, which is typical of heater-cantilevers [6,14,26,27]. Each device shows a nonlinear electrical resistance typical of doped silicon. The characteristic nonlinear resistance change with increasing excitation voltage is due to increased carrier scattering in the doped silicon as the cantilever temperature increases. The decrease of the cantilever resistance after a peak value at high power is due to intrinsic carrier generation and the characteristic thermal runaway of doped silicon. The critical power, $P_{crit}$ at which the TCR changes from positive to negative depends on the device type since each device has a different shape, which affects the heat transfer of the cantilever. Generally, cantilevers with larger surface area require higher excitation voltage, since they transport heat into the environment more efficiently than cantilevers with smaller surface area.

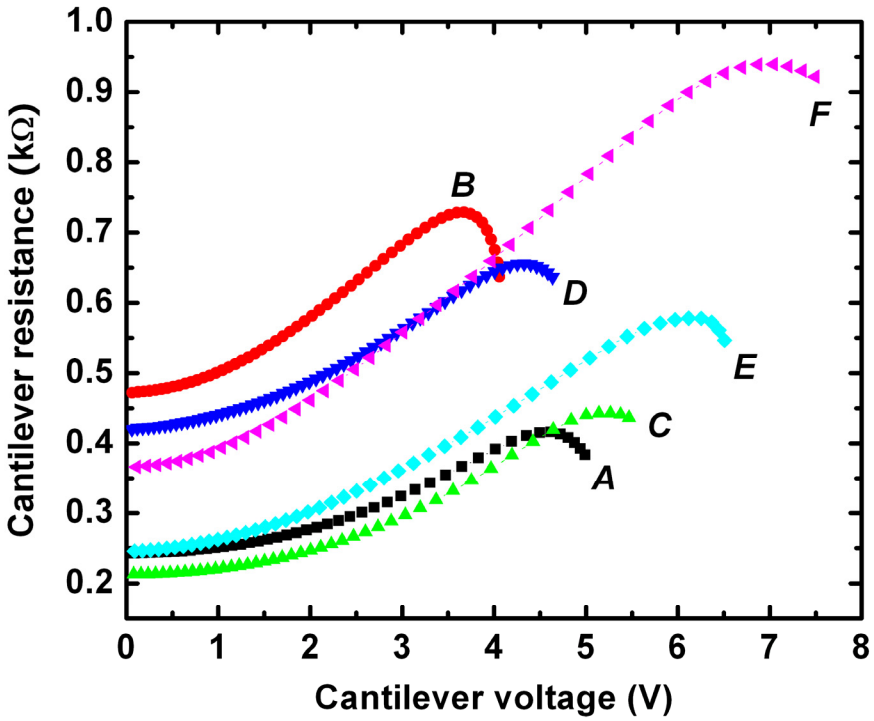


Figure 3.4 DC responses of microcantilever hotplates which are typical of heater-cantilevers.

Figure 3.5 shows transient electrical measurements that monitor the cantilever heating and cooling time constant. The cantilever circuit was excited with voltage pulses having 1V DC offset and 2 ms duration. An oscilloscope measured voltage drop across the bridge resistor. Figure 3.5(a) shows the transient resistance response of the type A cantilever during square pulse operation. Exponential growth/decay curve fits were introduced to extract heating time ($\tau_h$) and cooling time constants ($\tau_c$) of a type A device as shown in Figure 3.5(a). The experiments were repeated for all of the cantilever types, and the values for $\tau_h$ and $\tau_c$ are compared in Figure 3.5(b). The type C cantilever has the fastest cooling time constant at about 170 μs and the type F cantilever has the fastest heating time constant at about 250 μs. All cantilevers could be heated to above 550 °C within 20 μs using sufficiently large voltage pulses – usually in the range of 15 – 20 V.

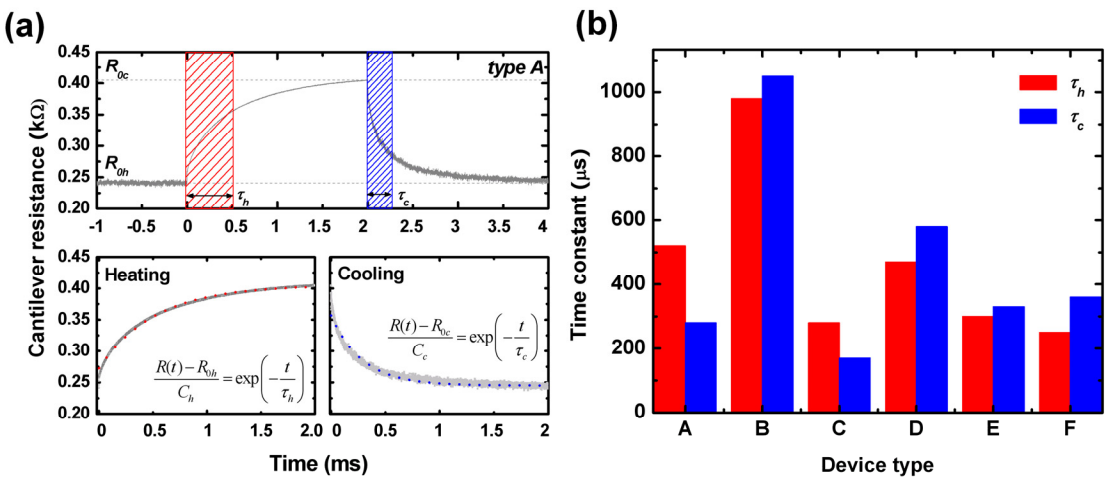


Figure 3.5 Transient electrical measurements that monitor the cantilever heating ($\tau_h$) and cooling time constants ($\tau_c$). (a) Transient resistance response of a type A device during a square pulse operation. (b) Comparison of heating and cooling time constants of each device type extracted from exponential growth / decay fits.

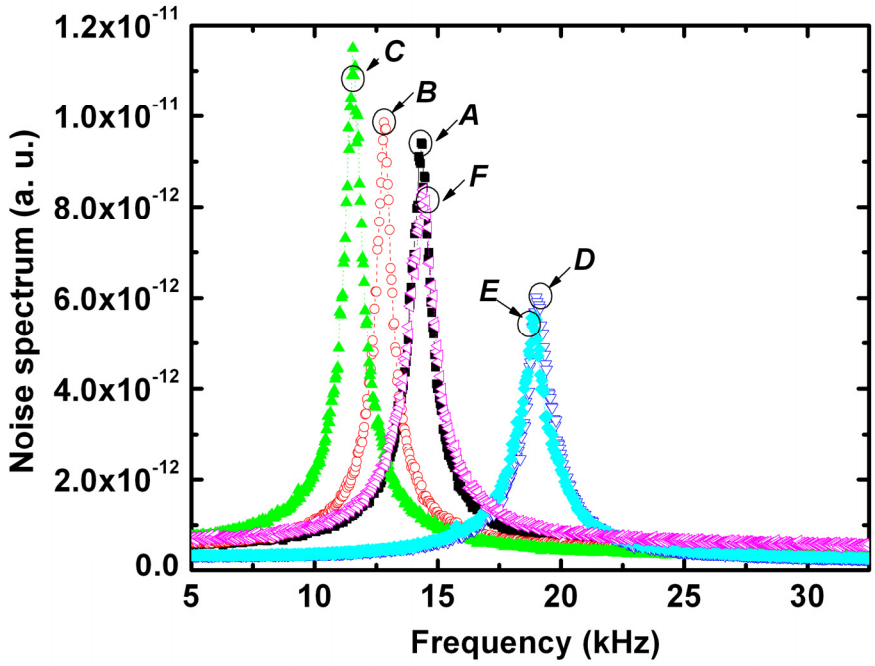


Figure 3.6 Fundamental resonance frequency of each device from thermomechanical noise spectra.

Following the electrical characterization, spring constant, resonance frequency, and quality factor of the cantilevers were characterized using a commercial AFM system (MFP-3D$^{TM}$, Asylum research). Figure 3.6 shows the fundamental resonance frequency

of each device from its thermomechanical noise spectrum. The thermomechanical noise spectra were measured for each cantilever and fitted using Lorentzian curve fits to get resonance frequencies and corresponding quality factors. The cantilever deflection sensitivity was also measured with a force-distance measurement. The equipartition theorem which relates potential energy to thermal energy [28] reveals the spring constant of each type for point force loading at its free end. Table 3.2 summarizes measurements of spring constant ($k$), resonance frequencies ($f_0, f_1, f_2$), and corresponding quality factors ($Q_0, Q_1, Q_2$).

Table 3.2 Summary of mechanical characterization: Spring constants, resonance frequencies and corresponding quality factors

| | A | B | C | D | E | F |
|---|---|---|---|---|---|---|
| $k$ (N/m) | 0.0044 | 0.0504 | 0.0348 | 0.0925 | 0.0985 | 0.0431 |
| $f_0$ (kHz) | 14.337 | 12.837 | 11.592 | 19.094 | 18.917 | 14.404 |
| $f_1$ (kHz) | 90.550 | 96.863 | 88.827 | 175.052 | 153.494 | 88.221 |
| $f_2$ (kHz) | 252.183 | 282.254 | 256.201 | 568.845 | 370.955 | 258.857 |
| $Q_0$ | 20.9 | 23.6 | 19.5 | 23.4 | 20 | 16.3 |
| $Q_1$ | 64.4 | 82.1 | 69.8 | 88.3 | 61.5 | 64.4 |
| $Q_2$ | 123.1 | 151.4 | 133.6 | 239.3 | 120.4 | 84.8 |

Finally, temperature calibration for each cantilever type was performed using both IR microscopy and Raman spectroscopy. Using IR microscopy, the spatial temperature distribution over the cantilever was investigated and local hot spots were identified. The IR microscopy was performed using an Infrascope$^{TM}$ II (Quantum Focus Instruments) equipped with a liquid nitrogen cooled 256 × 256 indium antimonide (InSb) detector

array. Using a 5× IR objective lens, the temperature data of each pixel represents a field of view of 1.24 μm square. Prior to temperature mapping, local emissivity of the non-operated device was obtained from reference radiance calibration at a fixed temperature using a temperature controlled sub-stage. Then, the device was powered and the local temperature of each pixel was measured using the obtained local emissivity [29].

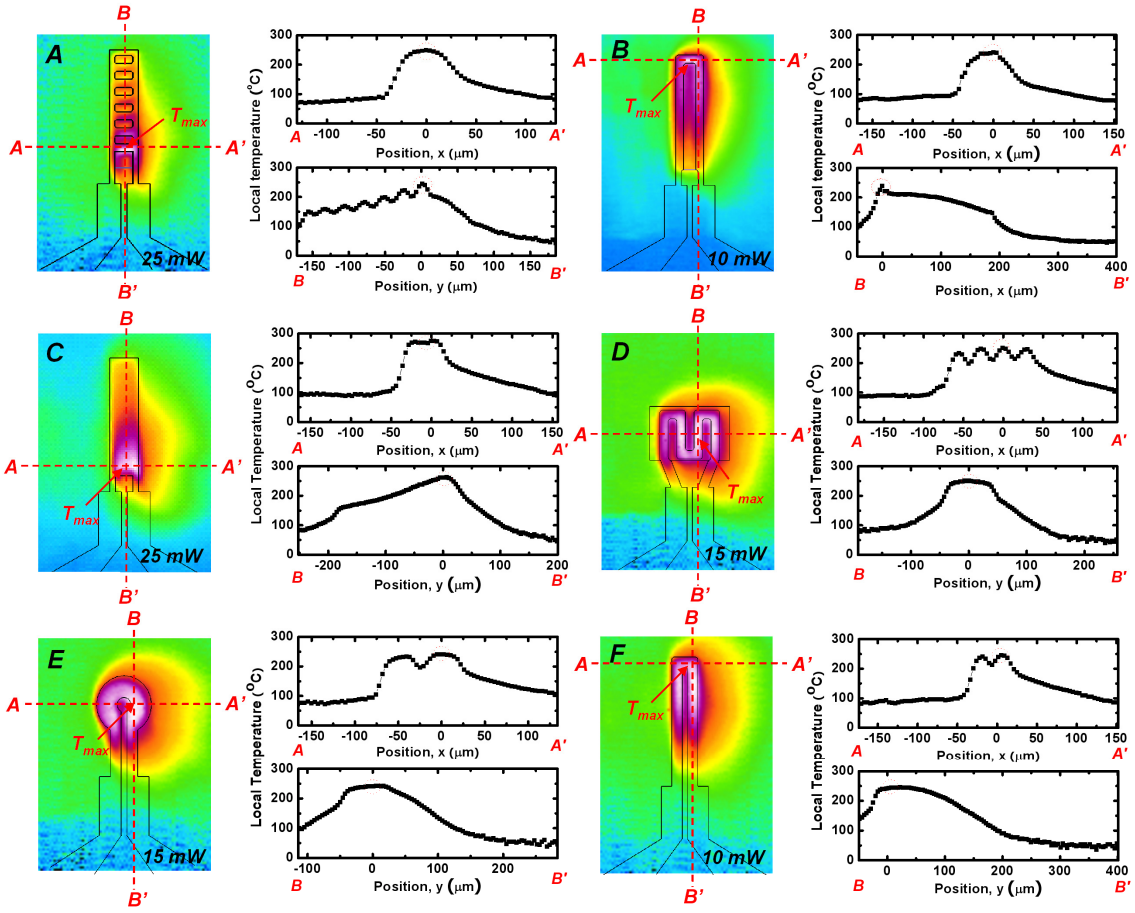


Figure 3.7 Temperature calibrations performed using IR microscopy. During IR temperature mapping, each device was heated with moderate electrical power in order not to exceed a defined temperature range (300 °C). 50 measurements for each device were made, averaged, and contour-plotted.

During IR thermometry, each device was heated with moderate electrical power in order not to exceed a device temperature of 300 °C. Fifty measurements were made for each device, averaged, and plotted as shown in Figure 3.7. The contour plots show the hot spots and vertical and horizontal cross-sectional plots show the temperature

distribution in the devices. Type A and C each have a hot spot near the anchor which is approximately 4 times thicker than the beam itself. Type B, E, and F have hot spots near their free end and the hot spot of type D is located around the center of the rectangular heater. The observed asymmetric temperature distribution was possibly due to the directional air motion and slight tilt angle between cantilever and microscope mount, which resulted in uneven localized thermal resistance. To evaluate temperature uniformity of each device, temperature average and standard deviation in the heater platform were extracted from the raw data. Figure 3.8 shows that the local temperature in the heaters of type A and C is highly populated below the average temperature. Cantilever types B, D, E, and F have local temperatures highly populated above the average temperature. For example, the type D device has a maximum temperature of 252 °C, and an average temperature of 213 °C with a standard deviation of 27.6 °C within the heater platform at 15 mW heating power. Average temperatures and standard deviations of other types for given electrical power are indicated in Figure 3.8.

In contrast to IR thermometry, Raman spectroscopy can produce higher accuracy temperature information, with a temperature range above 1000 °C and with 1 μm spatial resolution. Raman spectroscopy is, however, time consuming and has yet to be parallelized to produce large-scale temperature maps as in Figure 3.7. As explained in detail in chapter 2, local temperatures of these cantilevers can be measured by the intensity ratio of Stokes and Anti-Stokes peak, the line width of the Stokes peak, or the shift of the Stokes peak. The Stokes peak shift method was used in this chapter since the Stokes peak shows a linear shift over a wide temperature range and does not require detailed calibrations [30].

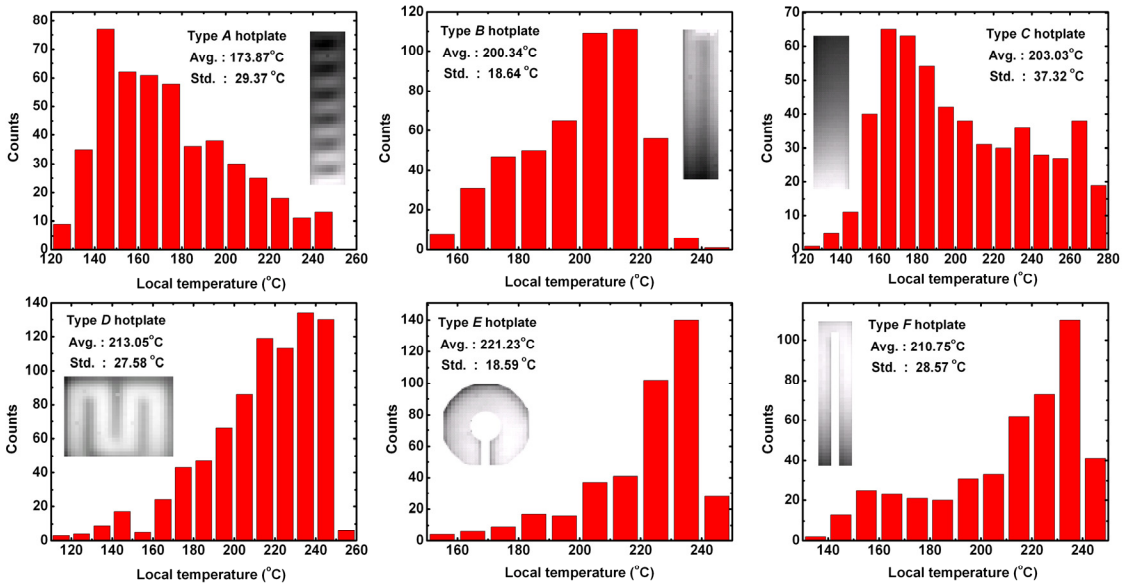


Figure 3.8 Histograms of the local temperatures in the heaters. Type A and C are highly populated at temperatures lower than average, however, other devices have the local temperature populated more at temperatures higher than average. Average temperatures and standard deviations for given electrical power are also included.

Figure 3.9 shows the maximum local temperature measured using an InVia Raman microscope (Renishaw). A 50× objective was used to collect the Raman signature of the devices and the laser power at the exit of the microscope objective was kept low to insure no change in Raman spectra due to laser heating [14]. During the voltage sweep, dissipated power and local temperature in each device were measured. Maximum local temperature in the heater region of each device is plotted as a function of device power in Figure 3.9. All devices show power consumption increased by a factor of 10 compared to heated cantilevers with localized heaters near the tip [14], but the measured power was still well below the design requirement for all types. The maximum local temperatures corresponding to $P_{crit}$ of types A, B, and D are far below 1000 °C. However, type C, E, and F can exceed 1000 °C at power < $P_{crit}$ where device operation is relatively safe. At low power, the maximum local temperature of each type changes linearly with power dissipation but nonlinearity is observed at high power. This is

possibly due to the higher uncertainty of the Raman measurement [30], which is ± 10 °C at the highest temperatures measured here.

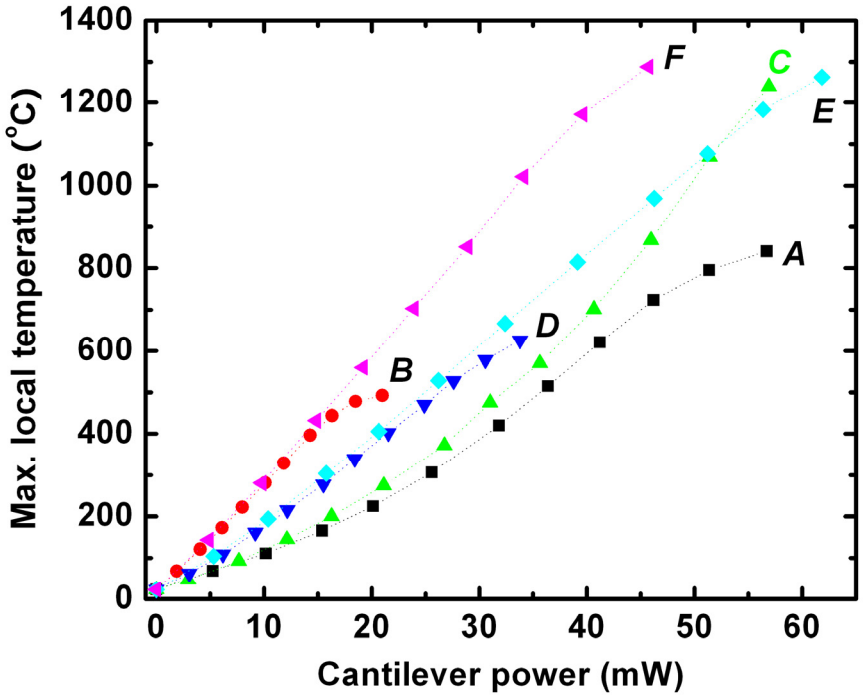


Figure 3.9 Maximum local temperature measured by the Stokes peak shift method using Raman spectroscopy.

### 3.4 Summary and Conclusions

In this chapter, various designs for cantilever type micro hotplates were proposed with the major requirements being fast response time and temperature uniformity by introducing parallel or series resistor networks and offsetting the major current carrying resistor from the free end to reduce the thermal diffusion length. Since the main objective of this work was to provide general characteristics of different shapes or resistor networks, none of the fabricated devices should be considered optimal. However these devices are an important first step in understanding the design of microcantilever hotplates. From the characterization results, the type C device shows the fastest response

and the type E device shows the best heating uniformity. The response time could be further improved by reducing the heater size and heating uniformity can be enhanced by making the resistor network narrower and denser. However, most bio/chemical sensors have sensing mechanisms that are improved with larger sensor area, and so the heating time constant must be balanced against the overall device sensitivity. This optimization of sensitivity vs. time constant should accommodate the end user's specifications.

In summary, cantilever type micro hotplates have been designed and fabricated to improve response time and enhance temperature uniformity. Detailed electrical, thermal, and mechanical characterizations were performed to evaluate the fabricated devices. The fabricated microcantilever hotplates have time constant < 1ms, maximum operation temperature > 1000 °C, and improved temperature uniformity over previously published results on heatable cantilevers.

## 3.5 References


[1] G. Y. Chen, R. J. Warmack, T. Thundat, D. P. Allison, and A. Huang, "Resonance response of scanning force microscopy cantilevers," *Review of Scientific Instruments*, vol. 65, pp. 2532-2537, 1994.

[2] T. Thundat, G. Y. Chen, R. J. Warmack, D. P. Allison, and E. A. Wachter, "Vapor detection using resonating microcantilevers," *Analytical Chemistry*, vol. 67, pp. 519-521, 1995.

[3] R. Berger, C. Gerber, J. K. Gimzewski, E. Meyer, and H. J. Guntherodt, "Thermal analysis using a micromechanical calorimeter," *Applied Physics Letters*, vol. 69, pp. 40-42, 1996.

[4] N. Abedinov, P. Grabiec, T. Gotszalk, T. Ivanov, J. Voigt, and I. W. Rangelow, "Micromachined piezoresistive cantilever array with integrated resistive microheater for calorimetry and mass detection," *Journal of Vacuum Science & Technology a-Vacuum Surfaces and Films*, vol. 19, pp. 2884-2888, 2001.

[5] S. Semancik and R. Cavicchi, "Kinetically controlled chemical sensing using micromachined structures," *Accounts of Chemical Research*, vol. 31, pp. 279-287, 1998.

[6] B. W. Chui, T. D. Stowe, Y. S. Ju, K. E. Goodson, T. W. Kenny, H. J. Mamin, B. D. Terris, and R. P. Ried, "Low-stiffness silicon cantilever with integrated heaters and piezoresistive sensors for high-density data storage," *Journal of Microelectromechanical Systems*, vol. 7, pp. 69-78, 1998.

[7] U. Drechsler, N. Burer, M. Despont, U. Dürig, B. Gotsmann, F. Robin, and P. Vettiger, "Cantilevers with nano-heaters for thermomechanical storage application," *Microelectronic Engineering*, vol. 67-68, pp. 397-404, 2003.

[8] F. T. Zhang, Z. Tang, J. Yu, and R. C. Jin, "A micro-Pirani vacuum gauge based on micro-hotplate technology," *Sensors and Actuators, A*, vol. 126, pp. 300-305, 2006.

[9] D.-S. Lee, J.-S. Huh, and D.-D. Lee, "Classifying combustible gases using micro-gas sensor array," *Sensors and Actuators, B*, vol. 93, pp. 1-6, 2003.

[10] D. N. Pagonis, G. Kaltsas, and A. G. Nassiopoulou, "Fabrication and testing of an integrated thermal flow sensor employing thermal isolation by a porous silicon membrane over an air cavity," *Journal of Micromechanics and Microengineering*, vol. 14, pp. 793-797, 2004.

[11] R. Triantafyllopoulou, S. Chatzandroulis, C. Tsamis, and A. Tserepi, "Alternative micro-hotplate design for low power sensor arrays," *Microelectronic Engineering*, vol. 83, pp. 1189-1191, 2006.

[12] P. Krebs and A. Grisel, "A low-power integrated catalytic gas sensor," *Sensors and Actuators, B*, vol. 13-14, pp. 155-158, 1993.

[13] J. Laconte, C. Dupont, D. Flandre, and J.-P. Raskin, "SOI CMOS compatible low-power microheater optimization for the fabrication of smart gas sensors," *IEEE Sensors Journal*, vol. 4, pp. 670-680, 2004.

[14] J. Lee, T. Beechem, T. L. Wright, B. A. Nelson, S. Graham, and W. P. King, "Electrical, thermal, and mechanical characterization of silicon microcantilever heaters," *Journal of Microelectromechanical Systems*, vol. 15, pp. 1644-1655, 2006.

[15] G. Binnig, M. Despont, U. Drechsler, W. Häberle, M. Lutwyche, P. Vettiger, H. J. Mamin, B. W. Chui, and T. W. Kenny, "Ultrahigh-density atomic force microscopy data storage with erase capability," *Applied Physics Letters*, vol. 76, pp. 1329-1331, 1999.

[16] W. P. King, T. W. Kenny, K. E. Goodson, G. L. W. Cross, M. Despont, U. Dürig, H. Rothuizen, G. Binnig, and P. Vettiger, "Atomic force microscope cantilevers for combined thermomechanical data writing and reading," *Applied Physics Letters*, vol. 78, pp. 1300-1302, 2001.

[17] P. E. Sheehan, L. J. Whitman, W. P. King, and B. A. Nelson, "Nanoscale deposition of solid inks via thermal dip pen nanolithography," *Applied Physics Letters*, vol. 85, pp. 1589-1591, 2004.

[18] B. A. Nelson, W. P. King, A. Laracuente, P. E. Sheehan, and L. J. Whitman, "Direct deposition of continuous metal nanostructures by thermal dip-pen nanolithography," *Applied Physics Letters*, vol. 88, pp. 033104, 2006.

[19] B. Gotsmann and U. Dürig, "Thermally activated nanowear modes of a polymer surface induced by a heated tip," *Langmuir*, vol. 20, pp. 1495-1500, 2004.

[20] B. Gotsmann and U. Dürig, "Experimental observation of attractive and repulsive thermal forces on microcantilevers," *Applied Physics Letters*, vol. 87, pp. 194102, 2005.

[21] E. O. Sunden, T. L. Wright, J. Lee, S. A. Graham, and W. P. King, "Room temperature chemical vapor deposition and mass detection on a heated atomic force microscope cantilever," *Applied Physics Letters*, vol. 88, 033107, 2006.

[22] W. P. King, S. Saxena, B. A. Nelson, B. L. Weeks, and R. Pitchimani, "Nanoscale thermal analysis of an energetic material," *Nano Letters*, vol. 6, pp. 2145-2149, 2006.

[23] S. L. Biswal, D. Raorane, A. Chaiken, and A. Majumdar, "Using a microcantilever array for detecting phase transitions and stability of DNA," *Journal of the Association for Laboratory Automation*, vol. 11, pp. 222-226, 2006.

[24] L. A. Pinnaduwage, A. Gehl, D. L. Hedden, G. Muralidharan, T. Thundat, R. T. Lareau, T. Sulchek, L. Manning, B. Rogers, M. Jones, and J. D. Adams, "A microsensor for trinitrotoluene vapour," *Nature*, vol. 425, pp. 474, 2003.

[25] J. Lee, T. Beechem, K. Park, Z. Zhang, S. Graham, and W. P. King, "Thermal and mechanical characterization and calibration of heated microcantilevers," presented at Solid State Sensors and Actuators Workshop, Hilton Head, SC, 2006.

[26] B. W. Chui, M. Asheghi, Y. S. Ju, K. E. Goodson, T. W. Kenny, and H. J. Mamin, "Intrinsic-carrier thermal runaway in silicon microcantilevers," *Microscale Thermophysical Engineering*, vol. 3, pp. 217-228, 1999.

[27] M. Despont, J. Brugger, U. Drechsler, U. Dürig, W. Häberle, M. Lutwyche, H. Rothuizen, R. Stutz, R. Widmer, G. Binnig, H. Rohrer, and P. Vettiger, "VLSI-NEMS chip for parallel AFM data storage," *Sensors and Actuators, A*, vol. 80, pp. 100-107, 2000.

[28] J. L. Hutter and J. Bechhoefer, "Calibration of atomic-force microscope tips," *Review of Scientific Instruments*, vol. 64, pp. 1869-1873, 1993.

[29] G. C. Albright, J. A. Stump, J. D. McDonald, and H. Kaplan, ""True" temperature measurements on microscopic semiconductor targets," *presented at 5th THERMINIC*, Rome, Italy, 1999.

[30] M. R. Abel, T. L. Wright, W. P. King, and S. Graham, "Thermal metrology of silicon micro-structures using Raman spectroscopy," *IEEE Transactions on Component and Packaging Technologies*, in press.

# CHAPTER 4

# 1 × 4 ARRAY OF MICROCANTILEVER HEATERS WITH INTEGRATED PIEZORESISTORS

## 4.1 Introduction

Microcantilevers have shown their versatility in various applications ranging from SPM to bio/chemical sensing. Single microcantilevers are capable of sub-nanometer topographic resolution in SPM [1] and femtogram adsorption/desorption detection in bio/chemical sensing [2]. The most common requirement in MEMS cantilever research is "array parallelization" to increase scanning speed and scan area or to test many analytes simultaneously. Array operation may also offer differential measurements that could cancel unwanted measurement artifacts.

Microcantilever probe arrays have been used in thermomechanical data storage [3-7], nanolithography [8-10], parallel imaging and force spectroscopy in life science applications [11]. Arrays having up to 64 × 64 microcantilevers with integrated heaters have been used to demonstrate probe based data storage [12]. Each cantilever enables writing, reading, and erasing of nanoscale indents on soft polymeric media [13]. A 100 × 100 array of thermo-piezoelectric microcantilevers has been reported with further improved data bit density [14]. A multifunctional microcantilever probe array has been developed for nano patterning and imaging using DPN and scanning probe contact printing [9]. A 4 × 4 array of piezoresistive microcantilever probes was specifically

designed and fabricated to image biological cells in a buffer solution and to perform force spectroscopy measurements on cells [11].

Another application of microcantilever arrays is bio/chemical species sensing where physiorption or chemiorption processes are transduced into a mechanical response [15]. In contrast to microcantilever probe arrays for imaging, these microcantilever arrays often operate far away from any substrate and do not require a tip. A $1 \times 8$ array of microcantilevers with selective coatings has been applied as an artificial nose to recognize and characterize alcohol vapors either in a static mode [16] or in a dynamic mode [17]. Besides gas sensing, the same platform was introduced to investigate DNA hybridization [15,18], antibody-antigen interaction [19,20], and two different DNA-binding proteins [21]. Recently, a 2D multiplexed array having 480 SiN/Au microcantilevers was fabricated to detect thermally induced phase transitions and stability of DNA [22].

Without regard to application, the major issue for the cantilever array operation is deflection sensing of each individual microcantilever. For small arrays, optical sensing such as vertical cavity surface emitting lasers (VCSELs) [16,17,21] can be used. However, having a large number of microcantilevers in the array requires integrated deflection sensing schemes, such as piezoelectric sensing, piezoresistive sensing, and capacitive sensing. Piezoresistive sensing has been widely used mainly because of the ease of fabrication. Moreover, it has been shown to be very sensitive with sub-nm minimum detectable deflection [23] and can be used in both static and dynamic modes for bio/chemical sensing.

Microcantilever arrays having both a resistive micro heater and a piezoresistor have been fabricated for thermomechanical data storage [4,24], and calorimetry and mass detection [25]. In the previous designs, there were little efforts to understand and suppress cross-coupling between the micro heater and the piezoresistor. Moreover, since they utilized evaporated or sputtered metals to make electrical tracks, the cantilevers were susceptible to electromigration and parasitic bending while the cantilevers were heated. This chapter describes design, fabrication, and characterization of a small 1D array of microcantilever heaters with integrated piezoresistors which only incorporate intrinsic and doped single crystalline silicon. The fabricated cantilever arrays can be used for high speed AFM, parallel scanning probe lithography and force spectroscopy on biological samples.

## 4.2 Electrical Simulation

The microcantilever arrays are made of doped single crystal silicon. In order to design the devices, it is important to estimate the resistivity and device resistance after implantation and diffusion since the thermophysical properties and heating characteristics of doped silicon depend upon local resistivity. This section describes modeling and simulation of diffusion, resistivity, and final resistance of doped silicon at given doping conditions.

To introduce dopants into the device layer in the microcantilever heater, ion implantation was chosen over diffusion since implantation is a low temperature process and gives more precise doping control. Equation (4.1) and (4.2) describe dopant

distribution, $N_d(x)$, in amorphous silicon after implantation following a Gaussian distribution.

$$N_d(x) = \frac{Q}{\sqrt{2\pi}\Delta R_P} \exp\left[-\frac{(x-R_P)^2}{2\Delta R_P{}^2}\right] \qquad (4.1)$$

$$Q = \sqrt{2\pi} N_{max} \Delta R_p \qquad (4.2)$$

where $Q$ is the dose, $N_{\max}$ is the maximum local doping concentration, $R_p$ is the average implant depth, and $\Delta R_p$ is the average variation in implant depth. The statistically determined values $R_p$ and $\Delta R_p$ are often referred to as range and straggle, respectively [26].

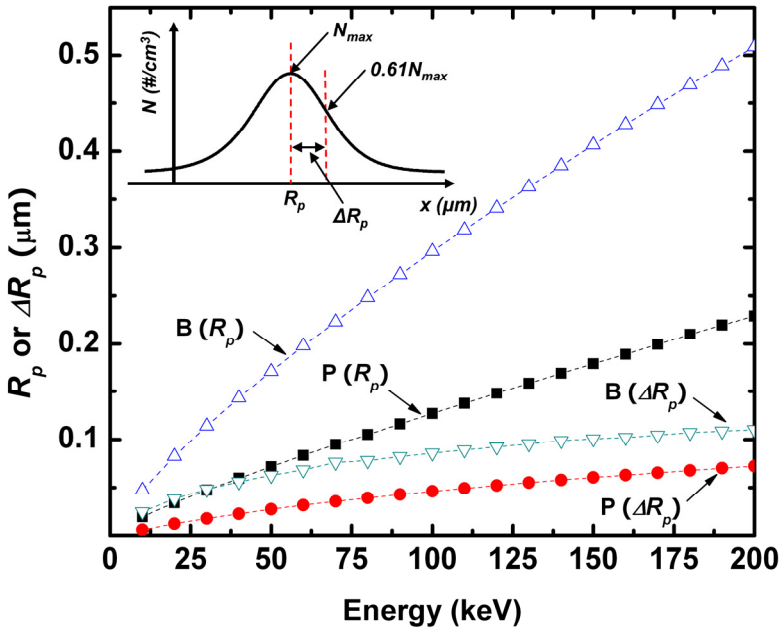


Figure 4.1 Range and straggle of boron (B) and phosphorus (P) as a function of implantation energy. Inset shows graphical indication for $N_{max}$ , $R_p$ , and $\Delta R_p$ [26].

Figure 4.1 shows range and straggle for phosphorus and boron as a function of implantation energy. Because single crystalline silicon will be the starting material for the array fabrication, introducing a 7° tilt angle during the implantation prevents ion channeling so that the Gaussian distribution can well describe doping profiles after

implantation. A 1D diffusion simulator using implantation results as initial conditions was constructed which accounts for both intrinsic and extrinsic diffusion. Diffusion phenomena are well described by Fick's 1st and 2nd laws given by

$$F = -D\frac{\partial N_d}{\partial x} \tag{4.3}$$

$$\frac{\partial N_d}{\partial t} = \frac{\partial}{\partial x}\left( D\frac{\partial N_d}{\partial x} \right) \tag{4.4}$$

where $D = D_0 \exp\left(-E_A / k_B T\right)$ is the diffusion coefficient or diffusivity, $E_A$ is the activation energy, $k_B$ is Boltzmann's constant, and $T$ is the diffusion temperature [27]. When the doping concentration ( $N_d$ ) is less than the intrinsic carrier concentration ( $N_i$ ) at diffusion temperature, diffusivity is independent of local doping concentration (intrinsic diffusion). However, diffusivity becomes concentration dependent when the doping concentration exceeds the intrinsic carrier concentration (extrinsic diffusion). This concentration dependent diffusivity can be explained in terms of the Fermi level. The main diffusion mechanism for dopants such as boron and phosphorus is vacancy diffusion such that the more vacancies exist, the faster dopants diffuse. Vacancy density ( $C_V$ ) also follows an Arrhenius relationship given by

$$C_V = C_i \exp\left( \frac{E_F - E_i}{k_B T} \right) \tag{4.5}$$

where $C_i$ is the intrinsic vacancy density, $E_F$ is the Fermi level, and $E_i$ is the intrinsic Fermi level [27]. Only when $N_d > N_i$, the Fermi level moves toward the conduction band and $C_V$ becomes greater than $C_i$. Finally, this increased vacancy density enhances the diffusion process. Therefore, equation (4.4) must be solved numerically. When $N_d > N_i$,

equations (4.6) and (4.7) were used in our simulation instead of using $D = D_0 \exp\left(-E_A / k_B T\right)$.

$$D_N = D^0 + D^- \left(\frac{N}{N_i}\right) + D^{--} \left(\frac{N}{N_i}\right)^2 \qquad (4.6)$$

$$D_P = D^0 + D^+ \left(\frac{P}{N_i}\right) + D^{++} \left(\frac{P}{N_i}\right)^2 \qquad (4.7)$$

where $D_N$ is the extrinsic diffusivity of the n-type dopant, $D_P$ is the extrinsic diffusivity of the p-type dopant, $N$ is the electron concentration, $P$ is the hole concentration, $D^0$ is the neutral component, $D^-$ and $D^+$ are the negative and positive components, and $D^{--}$ and $D^{++}$ are the double-negative and double-positive components of extrinsic dopant diffusion [28,29]. Again, each component follows an Arrhenius relationship. For example, $D^0 = D_0{}^0 \exp\left(-E_A{}^0 / k_B T\right)$. Coefficients used in the simulation are summarized in Table 4.1.

Table 4.1 Coefficients used in simulation for boron and phosphorus [26].

| | | Boron | Phosphorus |
|---|---|---|---|
| Intrinsic diffusion ($N_d < N_i$) | $D_0$ (cm$^2$/sec) | 1.0 | 4.7 |
| | $E_A$ (eV) | 3.5 | 3.68 |
| Extrinsic diffusion ($N_d > N_i$) | $D_0{}^0$ (cm$^2$/sec) | 0.05 | 3.85 |
| | $E_A{}^0$ (eV) | 3.5 | 3.66 |
| | $D_0{}^+$ (cm$^2$/sec) | 0.95 | - |
| | $E_A{}^+$ (eV) | 3.5 | - |
| | $D_0{}^-$ (cm$^2$/sec) | - | 4.44 |
| | $E_A{}^-$ (eV) | - | 4.0 |
| | $D_0{}^{--}$ (cm$^2$/sec) | - | 44.2 |
| | $E_A{}^{--}$ (eV) | - | 4.37 |

The bulk mobility ( $\mu_b$ ) was calculated using the simulated doping concentration. An electron and hole mobility model was adopted from [30] and is given by equations (4.8) - (4.11).

$$\mu_b(N_D,N_A,T)=\mu_0(N_D,N_A,T)+\frac{\mu_L(T)-\mu_0(N_D,N_A,T)}{1+\left(\frac{N_D}{C_{r1}}\right)^{\alpha_1}+\left(\frac{N_A}{C_{r2}}\right)^{\alpha_2}}+\frac{\mu_1(N_D,N_A,T)}{1+\left(\frac{N_D}{C_{r1}}+\frac{N_A}{C_{r2}}\right)^{-2}} \tag{4.8}$$

$$\mu_L(T)=\mu_{max}\left(\frac{T}{300}\right)^{-\gamma+c\left(T/300\right)} \tag{4.9}$$

$$\mu_0(N_D,N_A,T)=\frac{\mu_{0d}N_D+\mu_{0a}N_A}{N_D+N_A} \tag{4.10}$$

$$\mu_1(N_D,N_A,T)=\frac{\mu_{1d}N_D+\mu_{1a}N_A}{N_D+N_A} \tag{4.11}$$

where $\mu_L$ is the lattice mobility limited by acoustic and optical phonon scattering and $\mu_0(N_D,N_A,T)$ and $\mu_1(N_D,N_A,T)$ are weighted averages of the limiting values for donor and acceptor concentrations [30]. Coefficients and parameters for mobility calculations are summarized in Table 4.2.

Figure 4.2 shows doping concentration and resistivity of low doped phosphorus, high doped phosphorus, and medium doped boron which are obtained from the simulation. Finally, the simulated resistivity was used to calculate device resistance per unit length using a parallel resistor network [31] and the final resistance was obtained considering the actual geometry of the device. The device resistance was calculated once the cantilever dimensions were finalized. Our simulation up to the diffusion step was

compared with a SSUPREME simulation and showed good agreement. Simulated device resistances are compared with measurements in a following section.

Table 4.2 Coefficients and parameters for bulk mobility calculation [30].

| Parameters ($T_n = T$ / 300 K) | Boron | Phosphorus |
|---|---|---|
| $\mu_{max}$ (cm$^2$/Vsec) | 470.5 | 1441 |
| $c$ | 0.0 | 0.07 |
| $\gamma$ | 2.16 | 2.45 |
| $\mu_{0d}$ (cm$^2$/Vsec) | 90.0 × $T_n^{-1.3}$ | 62.2 × $T_n^{-0.7}$ |
| $\mu_{0a}$ (cm$^2$/Vsec) | 44.0 × $T_n^{-0.7}$ | 132.0 × $T_n^{-1.3}$ |
| $\mu_{1d}$ (cm$^2$/Vsec) | 28.2 × $T_n^{-2.0}$ | 48.6 × $T_n^{-0.7}$ |
| $\mu_{1a}$ (cm$^2$/Vsec) | 28.2 × $T_n^{-0.8}$ | 73.5 × $T_n^{-1.25}$ |
| $C_{r1}$ (cm$^{-3}$) | 1.3e18 × $T_n^{2.2}$ | 8.5e16 × $T_n^{3.65}$ |
| $C_{r2}$ (cm$^{-3}$) | 2.45e17 × $T_n^{3.1}$ | 1.22e17 × $T_n^{2.65}$ |
| $C_{s1}$ (cm$^{-3}$) | 1.1e18 × $T_n^{6.2}$ | 4e20 |
| $C_{s2}$ (cm$^{-3}$) | 6.10e20 | 7.0e20 |
| $\alpha_1$ | 0.77 | 0.68 |
| $\alpha_2$ | 0.719 | 0.72 |

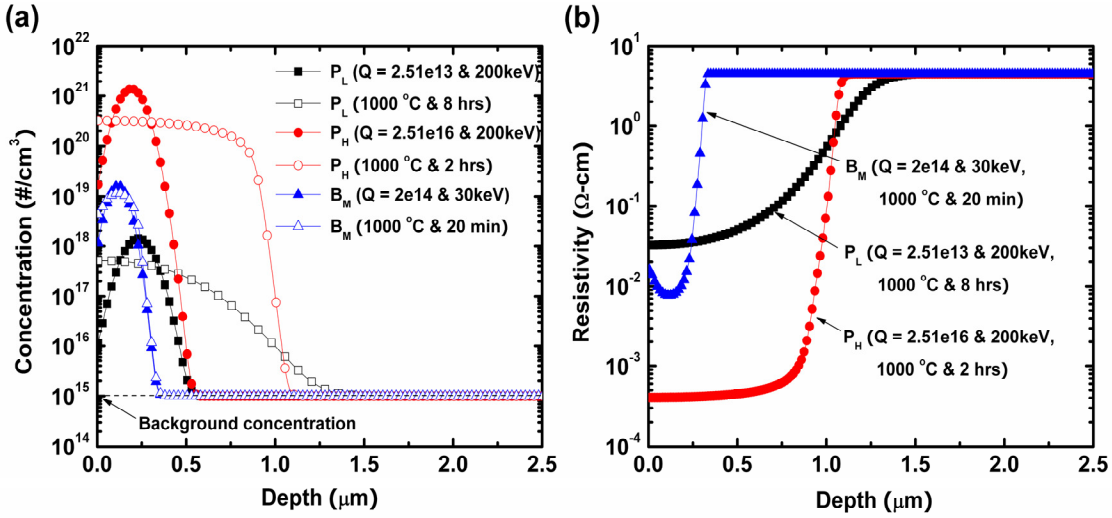


Figure 4.2 (a) Doping concentration of low doped phosphorus, high doped phosphorus, and medium doped boron after implantation and diffusion. (b) Resistivity after implantation and post diffusion.

Figure 4.3 shows a flow chart for the developed simulation which summaries this section.

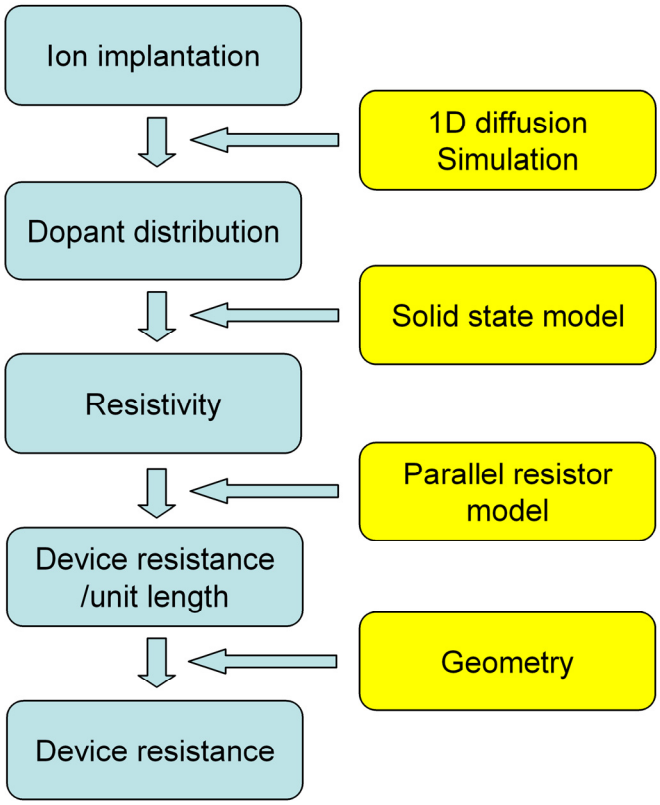


Figure 4.3 Flow chart to simulate doping concentration, resistivity, and resistance of doped silicon devices.

### 4.3 Design and Fabrication

The design of the cantilever array is based on the microcantilever heater introduced in chapter 2. A U-shaped cantilever is used to achieve thermal isolation between the heater and the piezoresistor. Extenders that connect the cantilever beam to the silicon handle layer are not necessary, since the cantilever can be made long enough without extenders, and because the fabricated device will have self sensing piezoresistors so that there is no requirement for the optical path of the laser in an AFM. Perhaps more importantly, the extenders' location in the previous microcantilever heater is the preferred site for the piezoresistors in order to maximize deflection sensitivity. Each individual

cantilever in an array will have 4 legs. The two outer legs will be highly doped to act as electrical leads to the resistive heater near the cantilever free end and the two inner legs will be used to define piezoresistors. The length of the inner legs, which is equivalent to that of the piezoresistors, is chosen to be about 0.4 of the overall cantilever length considering noise and resolution [32]. Figure 4.4(a) shows the final design of the 1 × 4 array of microcantilever heaters with integrated piezoresistors and dimensions for an individual cantilever in micron.

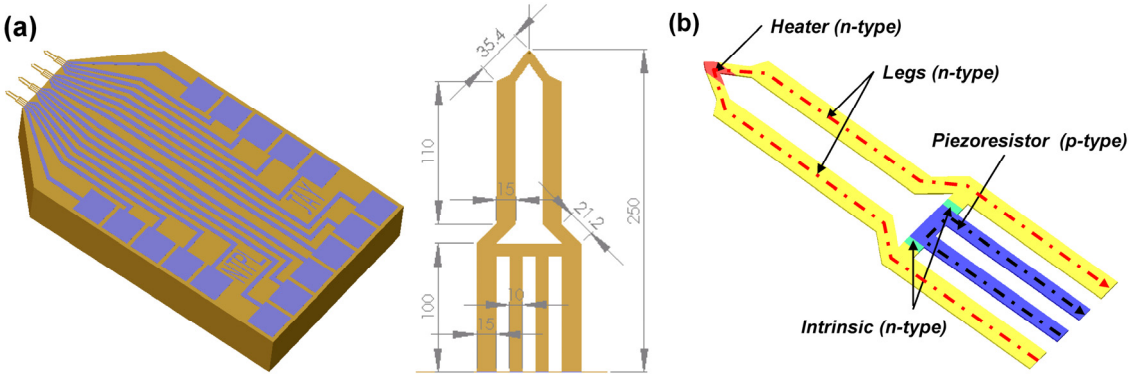


Figure 4.4 (a) Design of 1 × 4 array of microcantilever heaters with integrated piezoresistors and dimensions for an individual cantilever in micron. (b) Single cantilever showing different doping regions for heater and piezoresistor.

Resonance frequency and spring constant can be easily obtained from finite element simulation. Figure 4.5(a), (b), and (c) show predicted resonance frequency and spring constant as a function of the cantilever thickness ($t$). As expected, simulated resonance frequency and spring constant are proportional to $t$ and $t^3$, respectively. The simple harmonic oscillator model can be applied to a microcantilever structure, but the mass needs to be corrected since it is distributed over the cantilever length direction instead of being concentrated at the free end. This corrected mass is often referred to as effective mass ($m_{eff}$). The resonance frequency of the microcantilever is given by

$$f_0 = \frac{1}{2\pi}\sqrt{\frac{k}{m_{eff}}} = \frac{1}{2\pi}\sqrt{\frac{k}{C_m m}} \qquad (4.12)$$

where $k$ is the spring constant, $m$ is the total mass, and $C_m$ is the correction factor. For example, the effective mass of a simple rectangular cantilever is 24 % of the total mass. A correction factor of 0.148 was obtained for our cantilever as shown in Figure 4.5 (d).

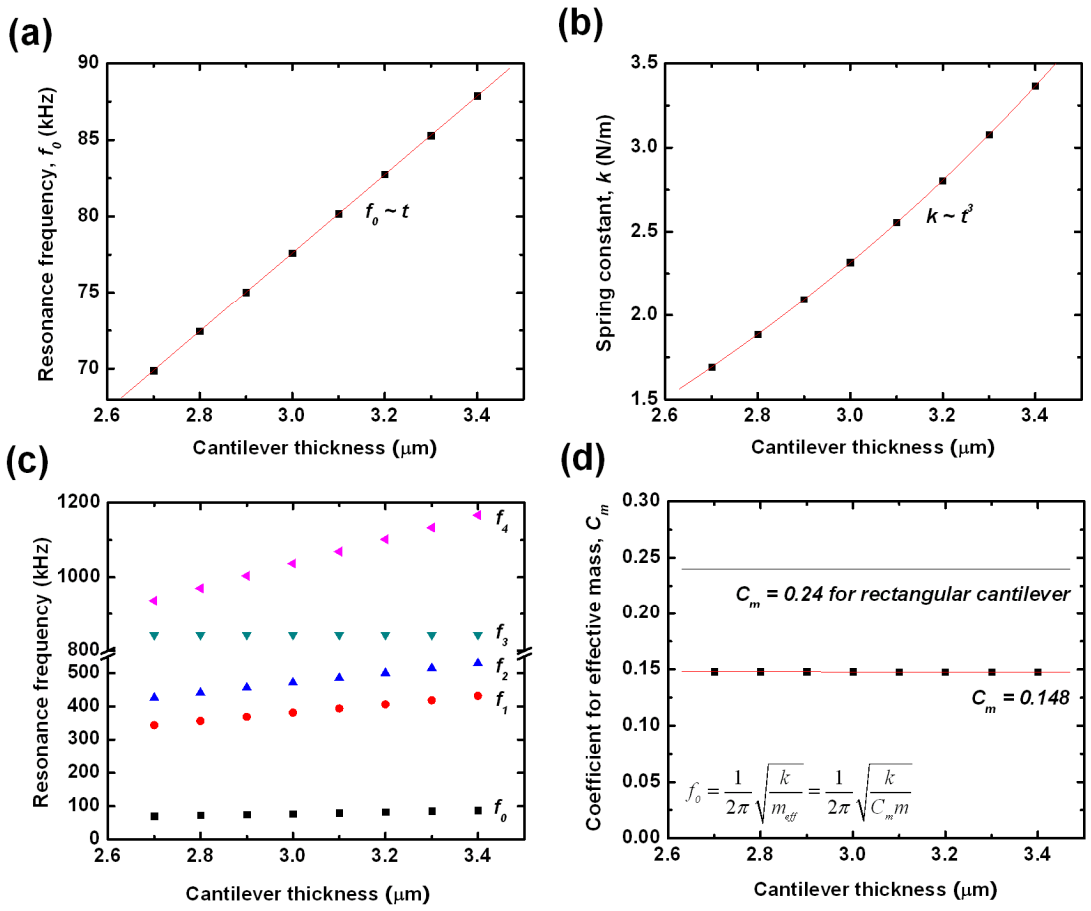


Figure 4.5 (a) Fundamental resonance frequency, (b) spring constant, (c) higher order harmonics, and (d) coefficient for effective mass calculation as functions of cantilever thickness. Results shown here are obtained from finite element simulation.

As dopants of the active silicon elements, phosphorus was chosen for the heater and the two outer legs because phosphorus has a lower resistivity than boron at a given doping concentration [33]. However, boron was chosen for the piezoresistors, mostly based on its higher piezoresistive coefficient than that of phosphorus in <110> crystalline

direction. Different dopant species and regions for the heater and the piezoresistor are shown in Figure 4.4(b).

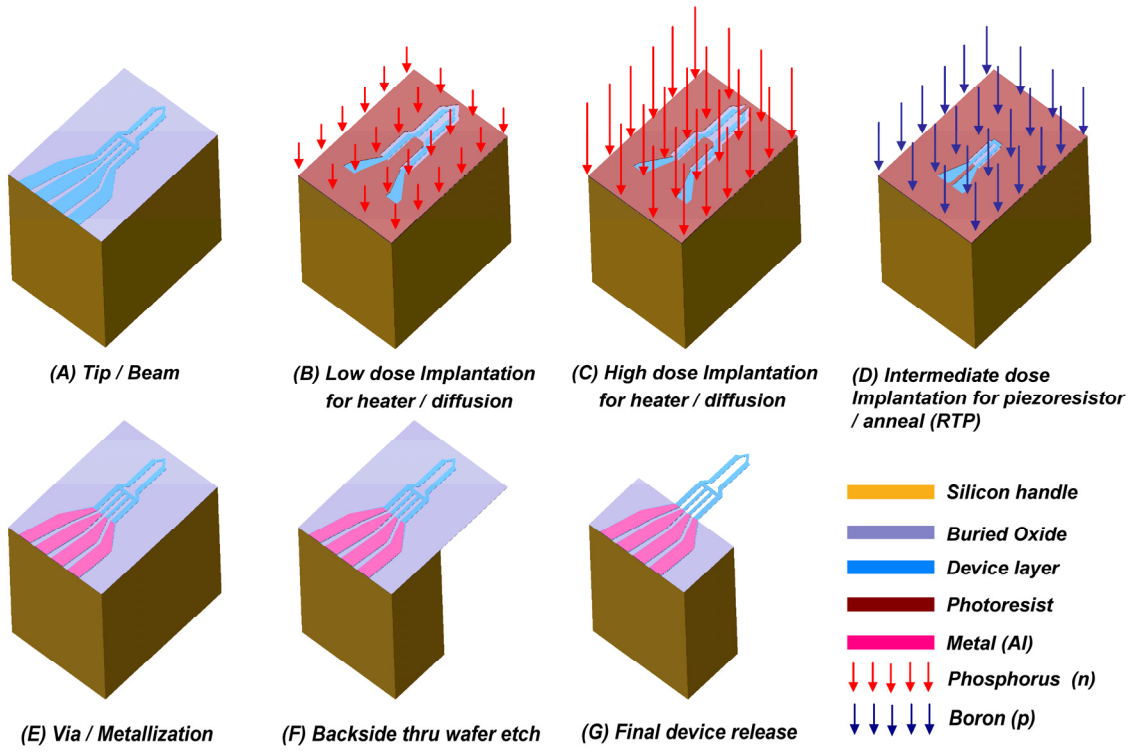


Figure 4.6 Seven major fabrication steps to make the microcantilever array

Figure 4.6 shows the seven major fabrication steps to make the microcantilever array. The fabrication process started with an n-type SOI wafer of orientation <100>, where the silicon device layer was 5 μm, the buried oxide layer was 1 μm, and the silicon handle layer was 500 μm. Background doping in the device layer was $1\times10^{15}cm^{-3}$ with a resistivity of approximately 4 Ω-cm. The first step was to define a probe tip via dry isotropic silicon etch followed by oxidation sharpening. Then, photolithography patterned negative photoresist (Futurrex NR7-1500) to define the cantilever structures. A Bosch process using ICP etched the patterned window all the way through the device layer until the buried oxide layer was fully exposed. After the probe tip and beam structures were defined in the device layer, three implantation steps were performed with

hard baked positive photoresist (Shipley 1827) as a mask for ion implantation. The first implantation doped the heater region near the free end with $2.51\times10^{13}$ $cm^{-2}$ of phosphorous at 200 keV. A post diffusion step was performed for 6 hours at 1000°C in the furnace to distribute the implanted dopant uniformly. The second implantation step doped the two outer legs with $2.51\times10^{16}$ $cm^{-2}$ of phosphorous at 200 keV and a post diffusion step was performed for 2 hours at 1000°C in the furnace. The two implantations finalized the n-type resistive heaters. The final implantation defined the piezoresistor in the two inner legs with $2\times10^{14}$ $cm^{-2}$ of boron at 30 keV. The implanted piezoresistors were annealed for 20 minutes at 1000°C in a rapid thermal processing (RTP) chamber. After metallization and lift-off to define aluminum contacts, the backside of the handle wafer was etched using ICP until the buried oxide layer was exposed. The cantilever arrays were finally released by a 15 s dip in 49% hydrofluoric acid. More detailed fabrication processes can be found in Appendix B.

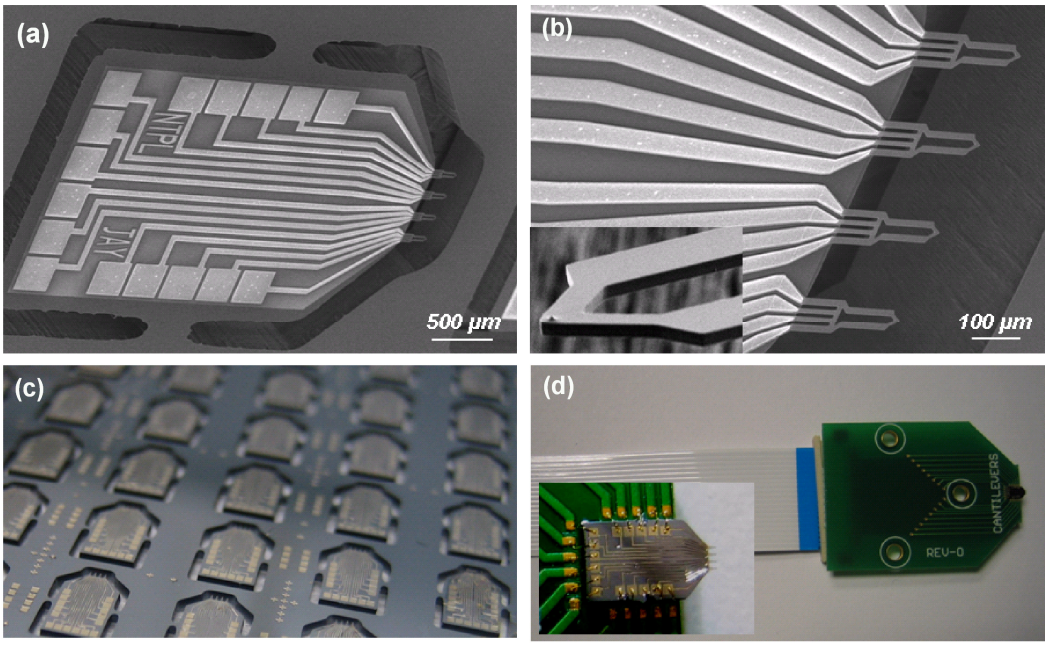


Figure 4.7 (a) (b) SEM images of the fabricated array chip. Inset in (b) shows the sharp tip near the low doped resistive heater (c) Batch fabricated array chip with high yield (d) Custom PCB and flexible ribbon cable to mount an array chip and make electrical connections. Inset shows a wire-bonded array chip.

Figure 4.7(a) and (b) show SEMs of the fabricated microcantilever array. The inset in Figure 4.7(b) shows the probe tip near the low doped resistive heater. Figure 4.7(c) shows batch fabricated array chips with high throughput and Figure 4.7(d) shows a custom printed circuit board (PCB) to mount the array chip and a flexible ribbon cable for electrical connection to power supply and front end of data acquisition.

## 4.4 Cantilever Characterization

After the array fabrication, microcantilever characterization was performed following the characterization techniques described in chapter 2. For the electrical testing, the cantilever was configured in series with precision 1 and 10 kΩ power resistors for heater and piezoresistor, respectively. The tested cantilever was excited with DC voltage to investigate steady state responses. Figure 4.8(a) shows the DC response of the heater defined near the free end and connected through the two outer highly conductive legs, which is typical of heater-cantilevers [5,34-36]. The critical power, $P_{crit}$, at which the TCR changes from positive to negative was 18 mW and the corresponding critical temperature, $T_{crit}$, was approximately 560°C. Figure 4.8(b) shows the DC response of the p-type piezoresistor defined in the two inner legs. $P_{crit}$ was not observed up to 20 mW since the TCR is much smaller than that of the heater. The piezoresistor is expected to reach its burn-out point before showing the critical power. Temperature data included herein were collected using Raman spectroscopy as explained in detail in chapter 2. Figure 4.8(c) and Figure 4.8(d) show the comparison of the normalized electrical resistances of the heater and the piezoresistor as functions of power dissipation and maximum temperature in the resistor, respectively. From Figure 4.8(d), the TCR of

the doped resistor was obtained. The TCR values of the heater and the piezoresistor were $2.01 \times 10^{-3}$ and $0.83 \times 10^{-3}$ Ω/Ω-°C, respectively. The higher TCR in the heater is mainly due to its low doping level.

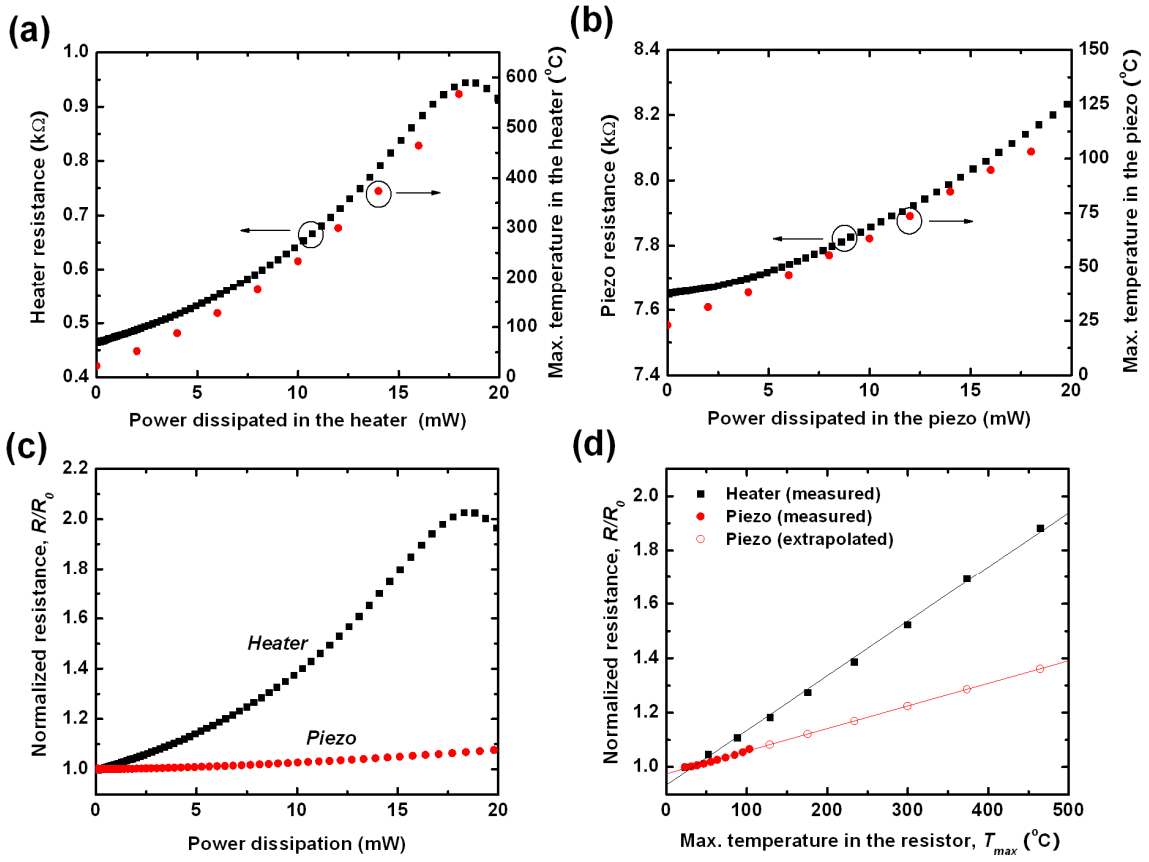


Figure 4.8 (a) Electrical resistance and temperature of the heater as a function of power dissipation in the heater. (b) Electrical resistance and maximum temperature of the piezoresistor as a function of power dissipation in the piezoresistor. (c) Normalized resistance comparison between the heater and the piezoresistor. (d) Normalized resistance of the heater and the piezoresistor as a function of the maximum temperature in each resistor. Temperature data were obtained using Raman spectroscopy [36].

After DC characterization and Raman temperature measurement, the temperature distribution both in the heater and in the piezoresistor was investigated using IR microscopy. Similar to the IR measurement in chapter 3, fifty measurements were made for each device, averaged, and plotted as shown in Figure 4.9. Figure 4.9(a) shows identical emissivity maps for two microcantilevers. Since the cantilevers are free standing, the region adjacent to each cantilever is air so that the emissivity data should be

neglected. Figure 4.9(b) and (c) show temperature distributions when the heater and the piezoresistor were heated to 5mW, respectively. Figure 4.9(d) shows a temperature map for combined operation when both the heater and the piezoresistor dissipated 5mW simultaneously. It should be noted that the additional 5 mW in the piezoresistor do not affect the maximum heater temperature since power generated in the piezoresistor is mostly dissipated into the silicon handle. For a practical use, the power dissipation in the piezoresistor will be less than 1 mW so that the heater temperature can be maintained regardless of the piezoresistor operation. However, temperature rise in the piezoresistor due to the heater operation might not be negligible since high power/temperature operation is often required for thermal nano-metrology and nano-manufacturing.

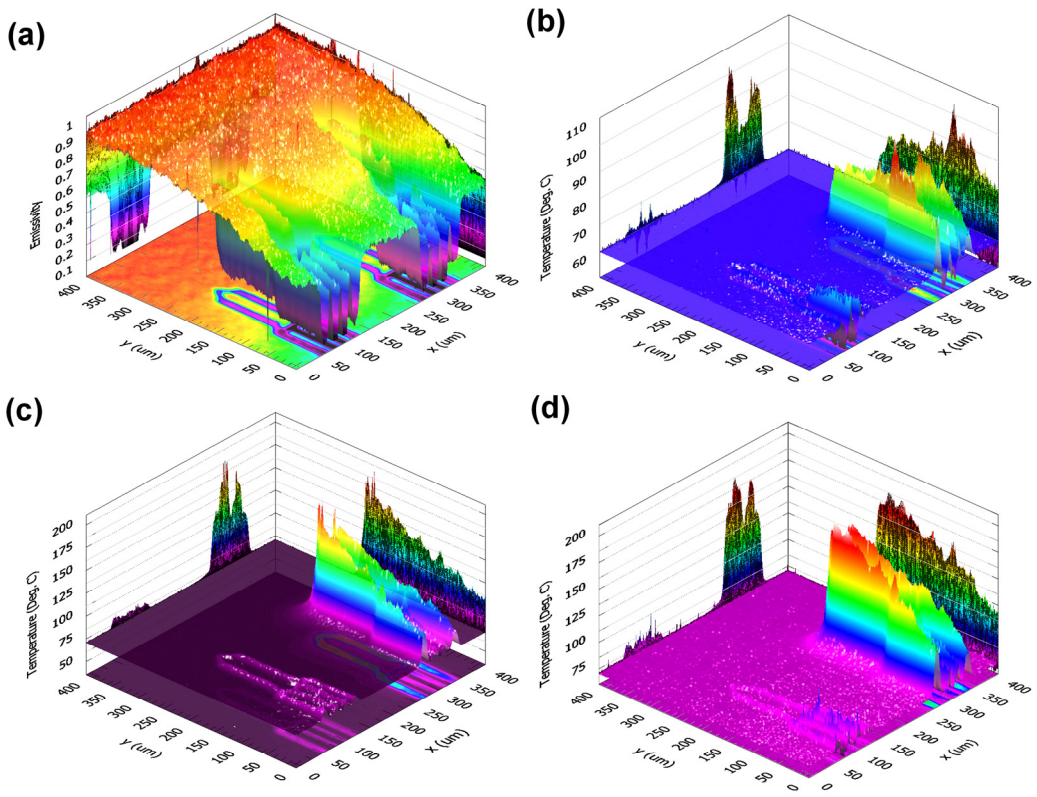


Figure 4.9 (a) Emissivity map for two neighboring cantilevers in an array chip. (b) IR micrograph with 5mW power dissipation in the piezoresistor of the right cantilever. (c) IR micrograph with 5mW power dissipation in the heater of the right cantilever. (d) IR micrograph with 5mW power dissipation both in the piezoresistor and in the heater of the right cantilever. The left cantilever was off during the measurement.

The most required characterization for a piezoresistive element is a deflection sensitivity measurement. To test the piezoresistor, a precision 3 axis microstage having 50 nm minimum increments was incorporated with a tungsten needle probe from a probe station, a 3 axis coarse manual stage, and a CCD camera as shown in Figure 4.10. This was modified based on the setup initially used in [37]. While the needle probe approaches and deflects the microcantilever probe tip, resistance changes are recorded using a Wheatstone bridge in conjunction with data acquisition. Since white light can change the resistance of the piezoresistor, the intensity of the coaxial light source for the CCD was fixed during sensitivity measurements.

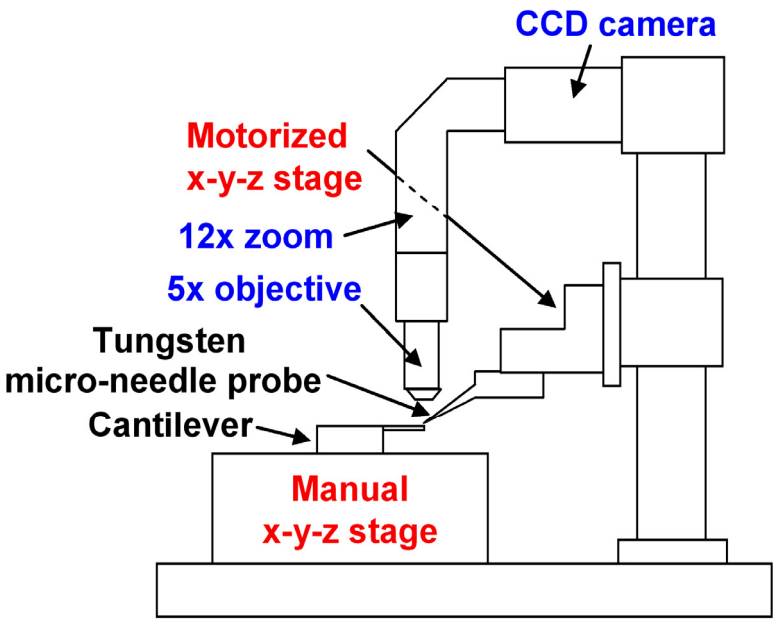


Figure 4.10 Experimental setup for deflection sensitivity measurement

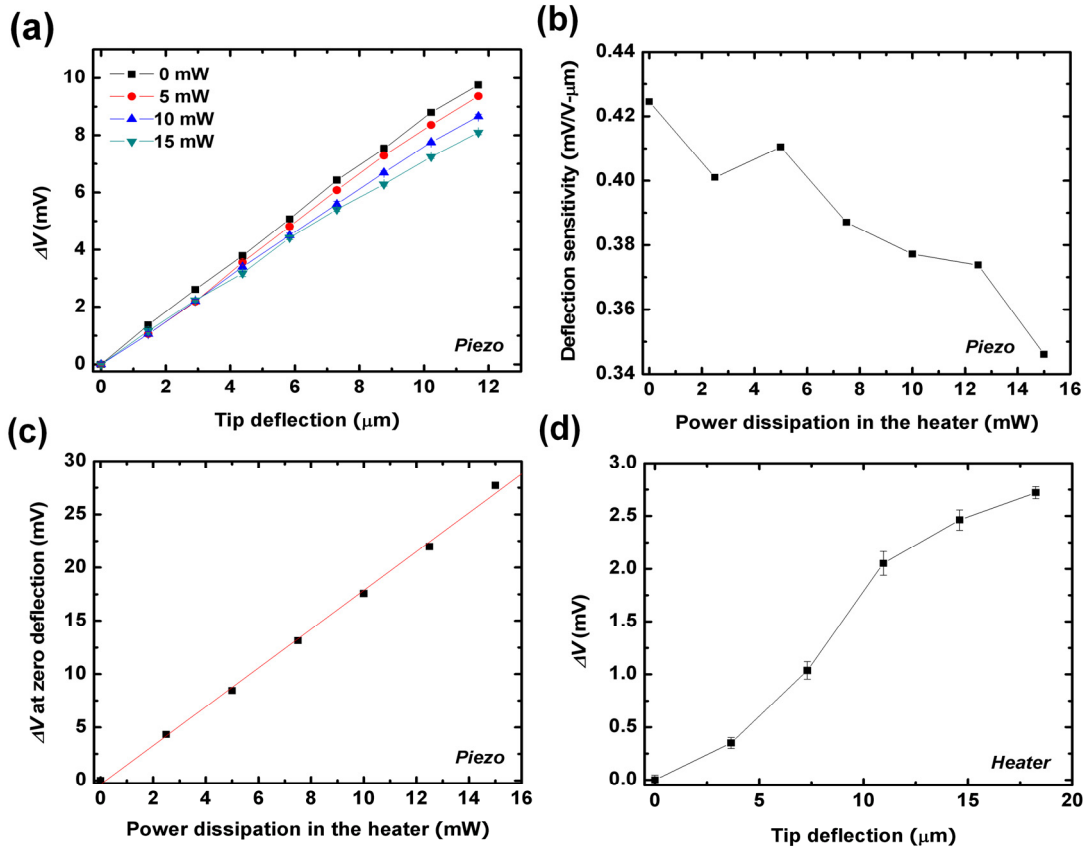


Figure 4.11 Cantilever deflection sensitivity. (a) Bridge voltage output as a function of the tip deflection where the applied voltage to the Wheatstone bridge is 2 V. (b) Deflection sensitivity of the piezoresistors which decreases as power dissipation in the heater increases. (c) Voltage offset linearly increases with power dissipation in the heater. (d) Voltage output from another bridge as a function of the tip deflection where the applied voltage to the Wheatstone bridge is 2 V.

Using the above setup, the deflection sensitivities of the heater and the piezoresistor were measured. Figure 4.11(a) shows the voltage change in the piezoresistor as a function of the tip deflection where the applied voltage to the Wheatstone bridge is 2 V. When the piezoresistor was operated alone, its deflection sensitivity was $4.245 \times 10^{-4}$ V/V-μm. Since both the mechanical properties of the microcantilever and the piezoresistivity of the doped silicon can be modulated upon heating, the deflection sensitivity measurement is required while the resistive heater is powered. Figure 4.11(a) and (b) show that the deflection sensitivity decreases as power

dissipation in the heater increases. When the piezoresistor temperature increases due to the power input in the heater, the piezoresistive coefficients decrease [38]. In addition, the elastic modulus of the silicon decreases upon heating so that the cantilever becomes softer. For a given deflection, the soft cantilever will experience less stress change than the stiff cantilever. These two effects are combined and decrease the deflection sensitivity of the piezoresistor. Heating affects not only the deflection sensitivity but also the offset in the voltage output from the bridge. To measure the voltage offset upon heating, the tungsten needle probe was brought into contact with the microcantilever probe tip and the Wheatstone bridge was tuned to give zero output voltage. Then, the resistive heater was heated with a certain power and the voltage output from the bridge was measured without deflection. Figure 4.11(c) shows that the voltage offset from the initially balanced Wheatstone bridge linearly increases with power dissipation in the heater.

Theoretically, highly doped silicon has very low piezoresistivity [38]. Therefore, it is often believed that microcantilever heaters having highly doped legs will have negligible piezoresistive effect so that their electrical resistance will be dominantly affected by temperature. Thus, little effort has been made to measure deflection sensitivity of microcantilever heaters. After another Wheatstone bridge was constructed with the heater and three additional resistors, the voltage output was measured and it is shown in Figure 4.11(d). The deflection sensitivity of the heater obtained from the linear fit was $7.86 \times 10^{-5}$ V/V-μm. Table 4.3 summarizes characterization results and also includes simulated electrical resistances which show good agreement with the measurement.

Table 4.3 Summarized characterization results.

| | Heater / legs | Piezoresistor |
|---|---|---|
| Measured electrical resistance (kΩ) | 0.45 ~ 0.50 (total) | 7.5 ~ 8.0 |
| Simulated electrical resistance (kΩ) | 0.4 / 0.17 | 8.60 |
| TCR (Ω/Ω-°C) | $2.010 \times 10^{-3}$ | $8.30 \times 10^{-4}$ |
| Deflection sensitivity (V/V-μm) | $7.86 \times 10^{-5}$ | $4.245 \times 10^{-3}$ |
| Spring constant (N/m) | 2.2 ~ 2.35 | |
| Resonance frequency (kHz) | 72.33 ~ 73.75 | |
| Quality factor | 110 ~ 134 | |

Then, the cantilever was mounted on a commercial AFM system to scan a calibration grating. The used grating had 200 nm tall square patterns which were evenly spaced. Two constructed Wheatstone bridges were used and interfaced with the data acquisition in the AFM controller. When the cantilever deflects against the calibration grating, the resistance of the piezoresistor changes and this unbalances the piezoresistor's Wheatstone bridge. When the gap distance between the cantilever heater and the substrate changes the thermal resistance from the cantilever to the substrate is modulated. This modulation changes the cantilever temperature which is transduced into the voltage signal from the Wheatstone bridge configured for the heater. This thermal reading concept originates from thermomechanical data storage research [39] and detailed demonstrations in contact mode [40] and tapping mode [41] have recently been reported. Theoretical and experimental studies have been published to compare the sensitivity of piezoresistive and thermal sensing. However, previous work employed two similarly sized cantilevers that have either resistive heaters or piezoresistors in simulations [42] or experimented only on thermal reading, and then compared its sensitivity to previously

reported sensitivities for piezoresistive reading [40]. The most relevant comparison could be performed on a cantilever which enables both thermal and piezoresistive reading but this has not been reported in the literature to our knowledge.

While the cantilever scanned the grating with the proportional-integral feedback loop turned off, either the piezoresistive reading or the thermal reading was recorded. Figure 4.12 shows the piezoresistive reading and the thermal reading for different bias voltages (3 V, 4 V, 5 V and 6 V) to each Wheatstone bridge. The scan area was 30 μm square, the scan rate was 1 Hz, and each frame had an image resolution of 256 × 256 pixels. When one doped resistor, either the piezoresistor or the heater, was powered, the other one was not used. The images on the left show filtered piezoresistive readings with 42.3 Hz cut-off frequency and 20 dB output gain. The images on the right show unfiltered thermal readings. When the same bias voltages were used, the signal to noise ratio (SNR) of the piezoresistive reading was too low to be measured. Therefore, the piezoresistor readings were filtered and amplified, although the cut-off frequency of 42.3 Hz could distort the signals. In contrast, thermal readings were sensitive enough not to require filtering. Piezoresistive signals linearly increased with the bias voltage to the Wheatstone bridge and the measured deflection sensitivity was approximately $2.5 \times 10^{-7}$ V/V-nm. The images on the right show unfiltered thermal readings. As expected from sensitivity measurements, thermal readings were more sensitive than piezoresistive readings. Thermal reading sensitivity ranged from $1 \times 10^{-6}$ to $5.83 \times 10^{-6}$ V/V-nm when the bias voltage changed from 3 to 6 V.

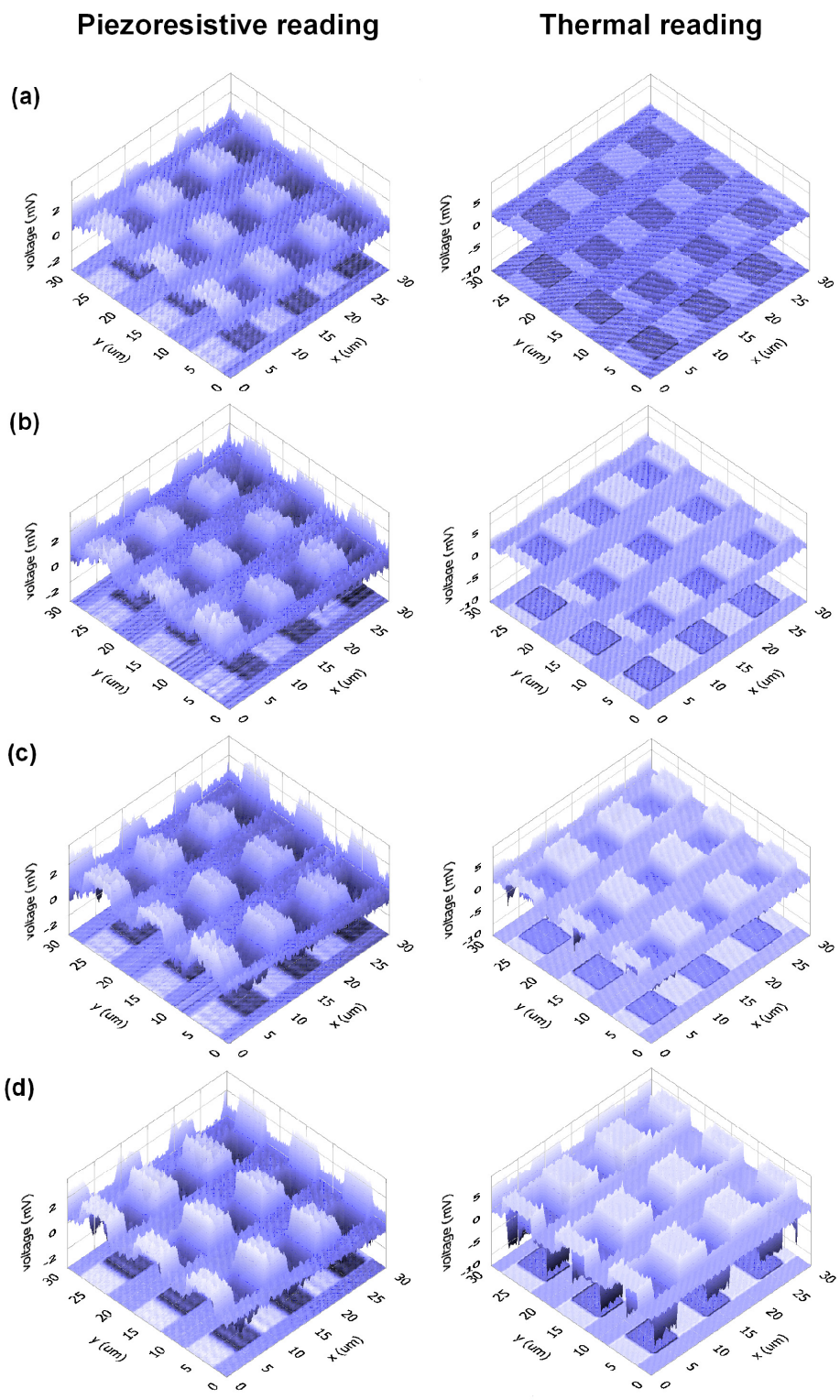


Figure 4.12 The left images show filtered piezoresistive reading with 20 dB gain and the right images show unfiltered thermal reading from a single cantilever. Voltages to the Wheatstone bridge are (a) 3 V (b) 4 V (c) 5 V and (d) 6V. Either the piezoresistor or the heater was operated independently.

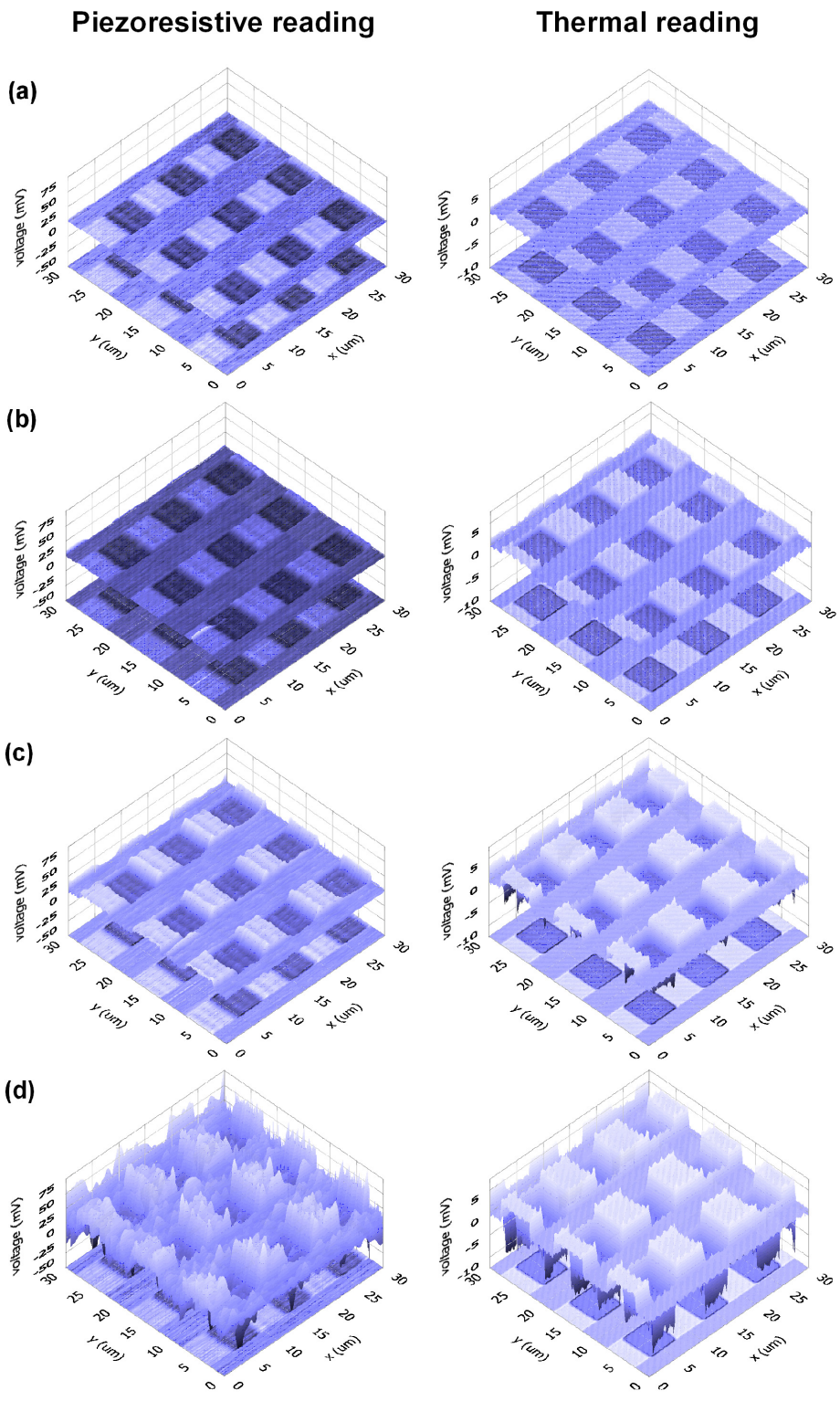


Figure 4.13 The left images show filtered piezoresistive reading with 20 dB gain and the right images show unfiltered thermal reading from a single cantilever. Voltages applied to the two Wheatstone bridges are (a) 3 V (b) 4 V (c) 5 V and (d) 6V. Both the piezoresistor and the heater were operated simultaneously.

After the independent operation of each doped resistor was performed, both the piezoresistor and the heater were powered simultaneously when the cantilever scanned the calibration grating to investigate thermal cross-talk between two doped resistors. Figure 4.13 shows the piezoresistive reading and the thermal reading for different bias voltages (3 V, 4 V, 5 V and 6 V) to each Wheatstone bridge. The other scanning parameters remain unchanged. Again, the images on the left show filtered piezoresistive readings and the images on the right show unfiltered thermal readings. Thermal readings were similar and comparable to the results from the independent operation since the additional heating from the piezoresistor would not affect the resistive heater temperature. However, the piezoresistive readings were significantly different to the results in Figure 4.12. Their signals showed steep increase with bias voltage so that the deflection sensitivity was not constant any more. Moreover, the sensitivity increased rather than decreased with the bias voltage. This is counter-intuitive since Figure 4.11 confirmed that the deflection sensitivity of the piezoresistor decreases as power dissipation in the heater increases. As mentioned earlier, the laser optical feedback was turned off during scanning. Due to the absence of the feedback loop, the cantilever deflection or contact force could not be controlled. Thus, the gap distance between the cantilever legs and the substrate could be greatly changed. Changes in the gap distance would be less problematic for independent piezoresistor operation or even for simultaneous operation with low bias voltage to the heater. However, the temperature change in the piezoresistor due to the gap distance modulation could be significant when the power dissipation in the heater is high enough. Finally, the piezoresistor temperature change unbalances the Wheatstone bridge. This is the most probable explanation for the enhanced piezoresistive readings when both

the piezoresistor and the heater are powered. Even though the piezoresistor was designed to transduce mechanical strain into a measurable electrical signal, it could be better to use it as a thermal displacement sensor when the temperature of the piezoresistor is high enough. Figure 4.14 summarizes the sensitivity results for comparison between the piezoresistive reading and the thermal reading for both independent and combined operation. Interestingly, the sensitivity of the piezoresistive reading might exceed that of the thermal reading at bias voltages above 6 V.

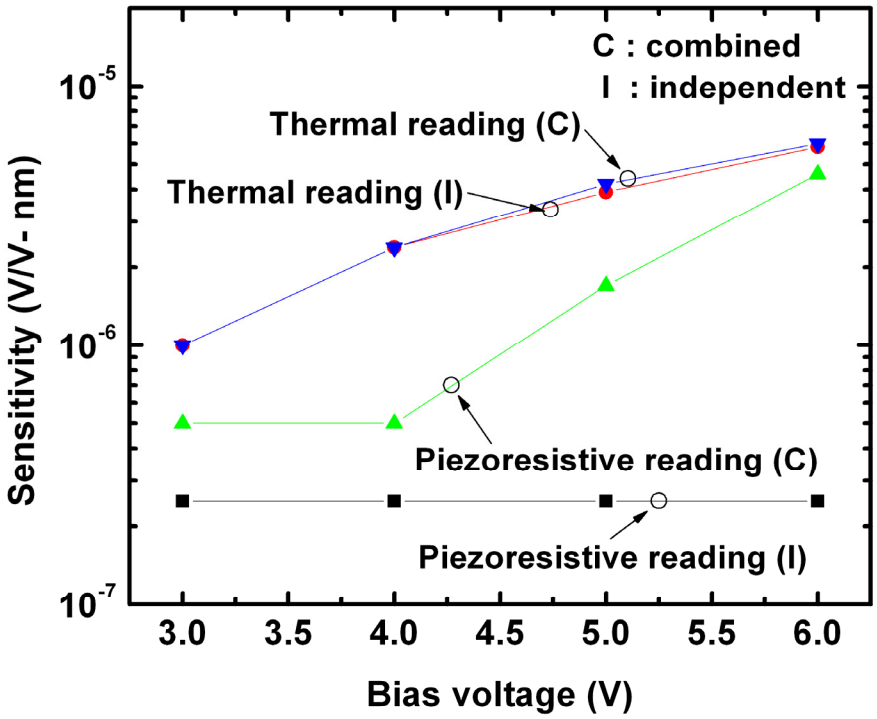


Figure 4.14 Sensitivity comparison between piezoresistive reading and thermal reading for both independent and combined operation.

### 4.5 Array Characterization

Since all cantilevers in an array chip were fabricated adjacent to each other, their dimensions including the cantilever thickness were more or less identical. Any local variation during fabrication steps such as etching, deposition, and implantation was less

likely to be observed within an array. In addition, each cantilever has individual electrical contacts due to the small number of devices per array so that no additional components such as Schottky diodes [5] are required to suppress electrical cross-talk for individual cantilever addressing. Therefore, basic mechanical, thermal, and electrical characteristics were expected to be uniform. The most relevant array characterization would be to scan the calibration grating using four cantilevers at the same time.

Figure 4.15 shows the topography based on scans performed with optical reading, piezoresistive reading and thermal reading for four cantilevers in a single array chip. Four cantilevers were operated simultaneously but either the piezoresistor or the heater in a cantilever was powered at a time. The bias voltage was fixed at 4 V for both Wheatstone bridges. Before the array chip was attached and wire-bonded to the custom PCB, it was mounted on the dedicated cantilever holder in the commercial AFM. This enabled topography scans employing a laser and a photodiode. The images on the left show the topography data from the four cantilevers. This topography was not necessary since the cantilevers have two additional topography sensing mechanisms. However, the obtained four topographic images could be used to compare the tip shape of each cantilever. The center and right columns of images show results from the filtered piezoresistive reading and the unfiltered thermal reading, respectively. The measured sensitivities for the piezoresistors ranged from $1.5 \times 10^{-7}$ to $1.61 \times 10^{-7}$ V/V-nm and the sensitivities for the heaters ranged from $4.88 \times 10^{-6}$ to $6.0 \times 10^{-6}$ V/V-nm.

Most of the tests on the calibration grating except for the topography relying on the optical readout contained significant noise in their images. The major source was 60 Hz and their integer multiples from the power electronics and laboratory environment.

More efforts should follow to suppress this. Moreover, both the piezoresistive reading and the thermal reading were performed without any feedback routine so that their signal readouts possibly contained abnormal spikes when the cantilever met a sudden change in the local topography. Since both the piezoresistive reading and the thermal reading can be used for a feedback loop, it is recommended to construct a feedback control to eliminate the parasitic spikes and also prevent mechanical wear problems of the probe tip.

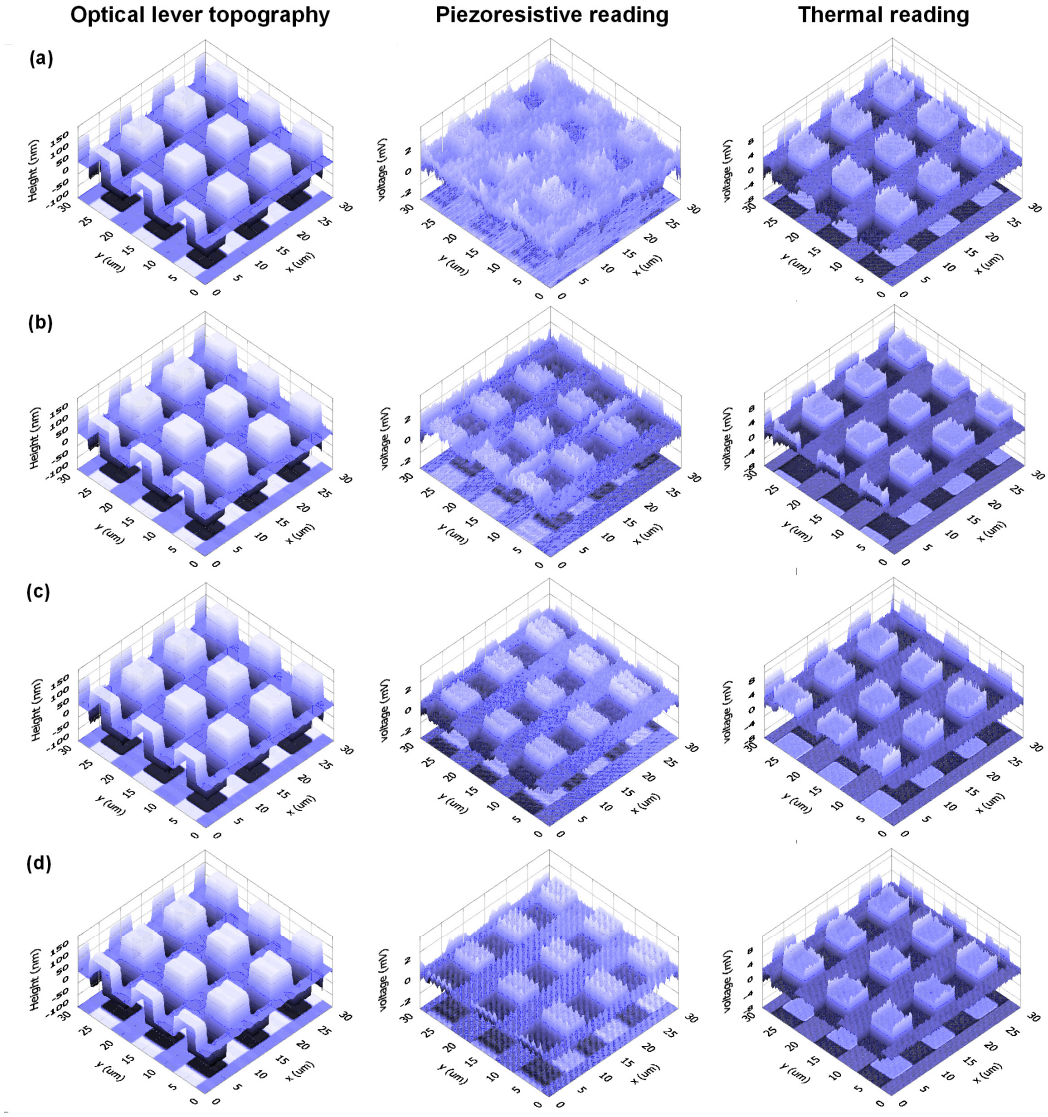


Figure 4.15 Left images show topography, center images show filtered piezoresistive readings with 20 dB gain, and right images show unfiltered thermal reading. Data are from (a) 1st cantilever (b) 2nd cantilever (c) 3rd cantilever and (4) 4th cantilever. All four cantilevers are operated simultaneously but either the piezoresistor or the heater in a cantilever is operated at a time with 4 V bias voltage.

The cantilevers scanned the calibration grating in "deflection mode (constant height mode)". This is originally useful for imaging very flat surfaces with high resolution and speed. In addition, this deflection mode is useful to test cantilever array devices that might have nonuniform tip height or initial deflection. However, this mode might result in more complex cantilever tip - substrate dynamics and instabilities. In the deflection mode, contact force changes according to the local topographic variation on the substrate. This dynamic force changes might result in instabilities especially at the edges of the square patterns. Transient effects might last longer in the deflection mode than in the feedback mode. However, this problem will be small when the scanning speed is fast enough. Scanning parameters were 1 Hz (or 75.12 μm/sec) for a 30 μm scanning area, thus there should be enough time, i.e., 1.5 ms, for the transient effects to die out between two adjacent topographic readings. Another possible problem is the torsional motion of the cantilever due to the friction. However, the torsional motion will not be effectively sensed using the piezoresistor aligned to the <110> crystalline direction. The resistance / temperature changes in the resistive heater and legs due to the torsional motion are also negligible since one half of them gets colder and the last half gets hotter so that this will average the resistance signal. Thermal reading results from the fabricated array device without optical feedback were compared with thermal reading results of a similarly sized heated cantilever with optical feedback. Even with the optical feedback, the anomalous spikes near the transitions existed so that they are expected to be a parasitic effect in thermal reading. The magnitude of those spikes possibly depends on the cantilever tip shape.

## 4.6 Summary and Conclusions

This chapter describes the design, fabrication and characterization of a small array of microcantilever heaters with integrated piezoresistors. The fabricated devices show successful integration of a resistive heater with a piezoresistive element in each cantilever. Instead of using metal traces, only doped silicon was used to suppress parasitic bending and prevent eletromigration upon heating. Each cantilever in an array was first characterized and array characterization was also performed on a calibration grating. In addition, thermal cross-talk between the piezoresistor and the heater was investigated and sensitivity comparison for the two topographic sensors embedded in a single cantilever was demonstrated for the first time. The fabricated devices will be applicable to parallel scanning probe lithography (SPL) and force spectroscopy. Combined heater and piezoresistor operation will enable *in-situ* detection and the construction of a compact customized AFM system. The results obtained in this chapter will give guidelines for the fabrication and integration of large 1D or 2D arrays of microcantilevers.

## 4.7 References


[1] T. R. Albrecht and C. F. Quate, "Atomic resolution imaging of a nonconductor by atomic force microscopy," *Journal of Applied Physics*, vol. 62, pp. 2599-2602, 1987.

[2] N. V. Lavrik and P. G. Datskos, "Femtogram mass detection using photothermally actuated nanomechanical resonators," *Applied Physics Letters*, vol. 82, pp. 2697-2699, 2003.

[3] P. Vettiger, J. Brugger, M. Despont, U. Drechsler, U. Dürig, W. Häberle, M. Lutwyche, H. Rothuizen, R. Stutz, R. Widmer, and G. Binnig, "Ultrahigh density, high-data-rate NEMS-based AFM data storage system," *Microelectronic Engineering* vol. 46, pp. 11-17, 1999.

[4] M. Lutwyche, C. Andreoli, G. Binnig, J. Brugger, U. Drechsler, W. Häberle, H. Rohrer, H. Rothuizen, P. Vettiger, G. Yaralioglu, and C. Quate, "5 × 5 2D AFM cantilever arrays a first step towards a Terabit storage device," *Sensors and Actuators, A*, vol. 73, pp. 89-94, 1999.

[5] M. Despont, J. Brugger, U. Drechsler, U. Dürig, W. Häberle, M. Lutwyche, H. Rothuizen, R. Stutz, R. Widmer, G. Binnig, H. Rohrer, and P. Vettiger, "VLSI-NEMS chip for parallel AFM data storage," *Sensors and Actuators, A*, vol. 80, pp. 100-107, 2000.

[6] U. Dürig, G. Cross, M. Despont, U. Drechsler, W. Häberle, M. I. Lutwyche, H. Rothuizen, R. Stutz, R. Widmer, P. Vettiger, G. K. Binnig, W. P. King, and K. E. Goodson, ""Millipede" - an AFM data storage system at the frontier of nanotribology," *Tribology Letters*, vol. 9, pp. 25-32, 2000.

[7] P. Vettiger, G. Cross, M. Despont, U. Drechsler, U. Dürig, B. Gotsmann, W. Häberle, M. Lantz, H. Rothuizen, R. Stutz, and G. Binnig, "The "Millipede"-nanotechnology entering data storage," *IEEE Transactions on Nanotechnology*, vol. 1, pp. 39-64, 2002.

[8] S. C. Minne, S. R. Manalis, A. Atalar, and C. F. Quate, "Independent parallel lithography using the atomic force microscope," *Journal of Vacuum Science & Technology B*, vol. 14, pp. 2456-2461, 1996.

[9] X. Wang and C. Liu, "Multifunctional probe array for nano patterning and imaging," *Nano Letters*, vol. 5, pp. 1867-1872, 2005.

[10] K. Kakushima, T. Watanabe, K. Shimamoto, T. Gouda, M. Ataka, H. Mimura, Y. Isono, G. Hashiguchi, Y. Mihara, and H. Fujita, "Atomic force microscope cantilever array for parallel lithography of quantum devices," *Japanese Journal of*

*Applied Physics Part 1-Regular Papers Brief Communications & Review Papers*, vol. 43, pp. 4041-4044, 2004.

[11] L. Aeschimann, A. Meister, T. Akiyama, B. W. Chui, P. Niedermann, H. Heinzelmann, N. F. de Rooij, U. Staufer, and P. Vettiger, "Scanning probe arrays for life sciences and nanobiology applications," *Microelectronic Engineering*, vol. 83, pp. 1698-1701, 2006.

[12] M. Despont, T. Altebaeumer, P. Bächtold, G. K. Binnig, G. Cherubini, U. Drechsler, U. Dürig, E. Eleftheriou, B. Gotsmann, W. Häberle, C. Hableitner, D. Jubin, A. Knoll, M. A. Lantz, A. Pantazi, H. Pozidis, H. Rothuizen, A. Sebastian, R. Stutz, P. Vettiger, D. Wiesmann, and J. Windeln, "A highly parallel probe-based storage system," *Digest of Papers - Microprocess and Nanotechnology 2004*, pp. 4-5, 2004.

[13] M. Despont, U. Drechsler, R. Yu, H. B. Pogge, and P. Vettiger, "Wafer-scale microdevice transfer/interconnect: Its application in an AFM-based data-storage system," *Journal of Microelectromechanical Systems*, vol. 13, pp. 895-901, 2004.

[14] Y. S. Kim, C. S. Lee, W. H. Jin, S. Jang, H. J. Nam, and J. U. Bu, "100 × 100 thermo-piezoelectric cantilever array for SPM nano-data-storage application," *Sensors and Materials*, vol. 17, pp. 57-63, 2005.

[15] J. Fritz, M. K. Baller, H. P. Lang, H. Rothuizen, P. Vettiger, E. Meyer, H. J. Guntherodt, C. Gerber, and J. K. Gimzewski, "Translating biomolecular recognition into nanomechanics," *Science*, vol. 288, pp. 316-318, 2000.

[16] M. K. Baller, H. P. Lang, J. Fritz, C. Gerber, J. K. Gimzewski, U. Drechsler, H. Rothuizen, M. Despont, P. Vettiger, F. M. Battiston, J. P. Ramseyer, P. Fornaro, E. Meyer, and H. J. Guntherodt, "A cantilever array-based artificial nose," *Ultramicroscopy*, vol. 82, pp. 1-9, 2000.

[17] F. M. Battiston, J. P. Ramseyer, H. P. Lang, M. K. Baller, C. Gerber, J. K. Gimzewski, E. Meyer, and H. J. Guntherodt, "A chemical sensor based on a microfabricated cantilever array with simultaneous resonance-frequency and bending readout," *Sensors and Actuators B-Chemical*, vol. 77, pp. 122-131, 2001.

[18] R. McKendry, J. Y. Zhang, Y. Arntz, T. Strunz, M. Hegner, H. P. Lang, M. K. Baller, U. Certa, E. Meyer, H. J. Guntherodt, and C. Gerber, "Multiple label-free biodetection and quantitative DNA-binding assays on a nanomechanical cantilever array," *Proceedings of the National Academy of Sciences of the United States of America*, vol. 99, pp. 9783-9788, 2002.

[19] G. H. Wu, R. H. Datar, K. M. Hansen, T. Thundat, R. J. Cote, and A. Majumdar, "Bioassay of prostate-specific antigen (PSA) using microcantilevers," *Nature Biotechnology*, vol. 19, pp. 856-860, 2001.

[20] Y. Arntz, J. D. Seelig, H. P. Lang, J. Zhang, P. Hunziker, J. P. Ramseyer, E. Meyer, M. Hegner, and C. Gerber, "Label-free protein assay based on a nanomechanical cantilever array," *Nanotechnology*, vol. 14, pp. 86-90, 2003.

[21] F. Huber, M. Hegner, C. Gerber, H. J. Guntherodt, and H. P. Lang, "Label free analysis of transcription factors using microcantilever arrays," *Biosensors & Bioelectronics*, vol. 21, pp. 1599-1605, 2006.

[22] S. L. Biswal, D. Raorane, A. Chaiken, and A. Majumdar, "Using a microcantilever array for detecting phase transitions and stability of DNA," *Journal of the Association for Laboratory Automation*, vol. 11, pp. 222-226, 2006.

[23] M. Tortonese, R. C. Barrett, and C. F. Quate, "Atomic resolution with an atomic force microscope using piezoresistive detection," *Applied Physics Letters*, vol. 62, pp. 834-836, 1993.

[24] Z. X. Yang, X. X. Li, Y. L. Wang, H. F. Bao, and M. Liu, "Micro cantilever probe array integrated with Piezoresistive sensor," *Microelectronics Journal*, vol. 35, pp. 479-483, 2004.

[25] N. Abedinov, P. Grabiec, T. Gotszalk, T. Ivanov, J. Voigt, and I. W. Rangelow, "Micromachined piezoresistive cantilever array with integrated resistive microheater for calorimetry and mass detection," *Journal of Vacuum Science & Technology A*, vol. 19, pp. 2884-2888, 2001.

[26] J. D. Plummer, M. D. Deal, and P. B. Griffin, *Silicon VLSI technology*: Prentice Hall Electronics and VLSI series, 2000.

[27] G. S. May and S. M. Sze, *Fundamentals of semiconductor fabrication*: Wiley, 2004.

[28] J. P. John and M. E. Law, "Phosphorus diffusion in isoconcentration backgrounds under inert conditions in silicon," *Applied Physics Letters*, vol. 62, pp. 1388-1389, 1993.

[29] R. B. Fair, *Impurity doping processes in silicon*, New York: North-Holland, 1981.

[30] S. Reggiani, M. Valdinoci, L. Colalongo, M. Rudan, G. Baccarani, A. D. Stricker, F. Illien, N. Felber, W. Fichtner, and L. Zullino, "Electron and hole mobility in silicon at large operating temperatures - Part I: Bulk mobility," *IEEE Transactions on Electron Devices*, vol. 49, pp. 490-499, 2002.

[31] S. D. Senturia, *Microsystem Design*, Boston: Kluwer Academic Publishers, 2001.

[32] J. A. Harley and T. W. Kenny, "1/F noise considerations for the design and process optimization of piezoresistive cantilevers," *Journal of Microelectromechanical Systems*, vol. 9, pp. 226-235, 2000.

[33] T. L. Wright, "Design and fabrication of heated atomic force microscope cantilevers," M. S. Thesis, Woodruff school of Mech. Eng., Georgia Inst. of Tech., Atlanta, GA, 2005.

[34] B. W. Chui, T. D. Stowe, Y. S. Ju, K. E. Goodson, T. W. Kenny, H. J. Mamin, B. D. Terris, and R. P. Ried, "Low-stiffness silicon cantilever with integrated heaters and piezoresistive sensors for high-density data storage," *Journal of Microelectromechanical Systems*, vol. 7, pp. 69-78, 1998.

[35] B. W. Chui, M. Asheghi, Y. S. Ju, K. E. Goodson, T. W. Kenny, and H. J. Mamin, "Intrinsic-carrier thermal runaway in silicon microcantilevers," *Microscale Thermophysical Engineering* vol. 3, pp. 217-228, 1999.

[36] J. Lee, T. Beechem, T. L. Wright, B. A. Nelson, S. Graham, and W. P. King, "Electrical, thermal, and mechanical characterization of silicon microcantilever heaters," *Journal of Microelectromechanical Systems*, vol. 15, pp. 1644-1655, 2006.

[37] B. W. Chui, L. Aeschimann, T. Akiyama, U. Staufer, N. F. de Rooij, J. Lee, F. Goericke, W. P. King, and P. Vettiger, "Advanced temperature compensation for piezoresistive cantilevers using 45-degree angle resistor pairs," *Review of Scientific Instruments*, in press.

[38] R. Hull and INSPEC (Information service), *Properties of crystalline silicon*, London: INSPEC, 1999.

[39] G. Binnig, M. Despont, U. Drechsler, W. Häberle, M. Lutwyche, P. Vettiger, H. J. Mamin, B. W. Chui, and T. W. Kenny, "Ultrahigh-density atomic force microscopy data storage with erase capability," *Applied Physics Letters*, vol. 74, pp. 1329-1331, 1999.

[40] K. J. Kim, K. Park, J. Lee, Z. M. Zhang, and W. P. King, "Nanotopograpical imaging using a heated atomic force microscope cantilever probe," *Sensors and Actuators A*, in press.

[41] K. Park, J. Lee, Z. M. Zhang, and W. P. King, "Nanotopograpical imaging with a heated atomic force microscope cantilever in tapping mode," *Review of Scientific Instruments*, in press.

[42] W. P. King, T. W. Kenny, and K. E. Goodson, "Comparison of thermal and piezoresistive sensing approaches for atomic force microscopy topography measurements," *Applied Physics Letters*, vol. 85, pp. 2086-2088, 2004.

# CHAPTER 5

# THERMAL CONDUCTION FROM MICROCANTILEVER IN PARTIAL VACUUM

## 5.1 Introduction

Thermal transport in regimes of size comparable to the energy carrier mean free path can differ significantly from thermal transport in bulk regimes [1] and the relevant physics govern both microcantilever heaters in partial vacuum and the operation of micron-sized Pirani gauges [2-4]. Pirani pressure sensors consist of a resistive heating element, having a temperature-dependent electrical resistance, mounted a finite distance from a heat sink. The typical Pirani sensor exploits the pressure-dependent molecular collision rate in the gap between heater and heat sink, such that enhanced cooling can be observed with increasing pressure. The dynamic range of the sensor is limited by the saturation of thermal conductance of the gas medium, which depends on the molecular collision rate. While micro Pirani gauges are well understood, somewhat less well studied are MEMS devices with an integrated heater where the heater element is small compared to the mean free path of the gas environment. The Knudsen number, $Kn = \Lambda / l$, is the ratio of the energy carrier mean free path, $\Lambda$, to the size of either the heater or the constriction, $l$. $Kn$ is a measure of molecular collision rate and can characterize the operation of Pirani gauges and other MEMS devices having integrated heaters [5].

AFM cantilevers having integrated resistive heaters were originally developed for data storage [6-8], but have since been shown to be useful for sensing [9,10], nanoscale manufacturing [11,12], and microscale thermophysical measurements [13-16]. Previous published studies of thermal interactions between a heated cantilever and its surroundings have shown that gas-gas and gas-solid molecular collisions in the gap between a heated microcantilever and a surface can play a significant role in the thermal conductance between the two bodies and can exert Knudsen forces on the cantilever, inducing cantilever bending [10,13-16]. For decreasing pressure, the gaseous molecular mean free path becomes long and these effects may become particularly acute. However, there are no published reports on thermal transport between an AFM cantilever having an integrated heater and a vacuum environment.

This chapter reports experimental observations of heat flow from microcantilever heaters into air or helium for $10^{-2} < Kn < 10^{4}$ where $Kn$ is based on the cantilever heater size. Unlike previous reports on heat transport between a heated cantilever and a vacuum environment, the present study measures both temperature and heating power inside the cantilever, allowing direct measurement of thermal conductance.

## 5.2 Experiments

The experiments were performed using heatable AFM cantilevers fabricated following a fabrication process modified from previous reports [17]. The heatable cantilever was 100 μm long with two 10 μm wide legs and the heater was approximately 8 μm × 16 μm in size. Overall the cantilevers had electrical resistance near 1.8 kΩ. When electrical current passes through the cantilever, the high resistance region at the

end of the cantilever is resistively heated. When the cantilever is operated in a quiescent environment, solid conduction through the cantilever legs and gas conduction through the adjacent gas surroundings balance the heat generated near the cantilever free end.

The experiment began with electrical characterization of the heated cantilever described in chapter 2. Because about 90 % of the cantilever resistance is the resistance of the cantilever heater region, the cantilever total electrical resistance is very close to the resistance of the cantilever heater. The cantilever total electrical resistance is thus a good indicator of the temperature in the cantilever heater region. Thus, it is reasonable to assume that the temperature calibration of cantilever electrical resistance performed at ambient pressure can be broadly applied over a large range of pressures [7,8,13-17]. Over the temperature range measured, the cantilever temperature was linear with heating power, indicating that for operation in air at 1 ATM, thermal radiation is not a significant mode of heat transfer. A detailed analysis of the heat transfer modes will be discussed later.

Six cantilevers were calibrated and prepared in a single package, to check the consistency of the experimental results. The package was placed into an ultra high vacuum (UHV) chamber capable of controlled pressure between $10^{-6}$ and $10^{3}$ mbar. Since the cantilevers were positioned about 500 μm apart from the center of the bottom of the UHV chamber and about 25 cm away from the other surfaces, only the bottom surface of the UHV chamber and the nearby gas could act as conduction heat sinks. The chamber could be backfilled with different gases such that it was possible to modulate thermal properties of the gaseous environment near the cantilever. In this experiment, the gases were air and Helium.

The UHV chamber was pumped down to $10^{-6}$ mbar at the start of the experiments. The chamber was slowly filled with gas, stopping at predetermined pressures. At this point, the cantilever was powered with a steady excitation voltage, and the cantilever resistance and power were recorded. Three measurements were made for every decade of pressure. The cantilever response was measured for chamber pressures between $10^{-5}$ and $10^{3}$ mbar for air, and between $10^{-3}$ and $10^{3}$ mbar for Helium.

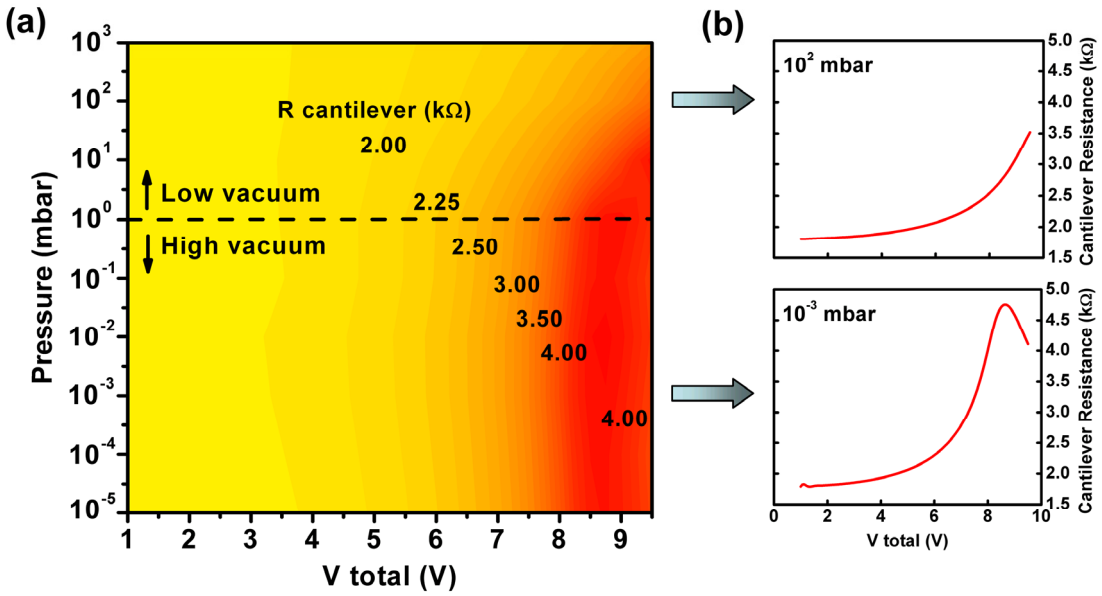


Figure 5.1 (a) Contour plot of electrical resistance of a heated AFM cantilever as a function of bias voltage and pressure in air. (b) Two representative plots of measured cantilever electrical resistance as a function of bias voltage at low vacuum ($10^{2}$ mbar) and high vacuum regime ($10^{-3}$ mbar).

Figure 5.1 shows measured cantilever electrical resistance as a function of excitation voltage in air with pressure between $10^{-5}$ and $10^{3}$ mbar. Figure 5.1(a) shows two distinct pressure regimes of thermal coupling between the cantilever and environment. At low vacuum, the peak resistance occurred at a decreasing excitation voltage with decreasing pressure. However, the heated cantilever became insensitive to further pressure reduction at high vacuum. Figure 5.1(b) shows two representative

cantilever electrical responses at $10^2$ and $10^{-3}$ mbar, corresponding to low vacuum and high vacuum cantilever response.

To compare power dissipation at a given pressure, Figure 5.2(a) shows dissipated power in the cantilever as a function of gas pressure for both air and helium when the cantilever heater temperature was held at 400 ºC. As expected, the cantilever could dissipate more power to the helium since helium thermal conductivity is higher than that of air at a given pressure. However, both air and helium show a crossover between 1 and 10 mbar where the dissipated power becomes pressure-independent.

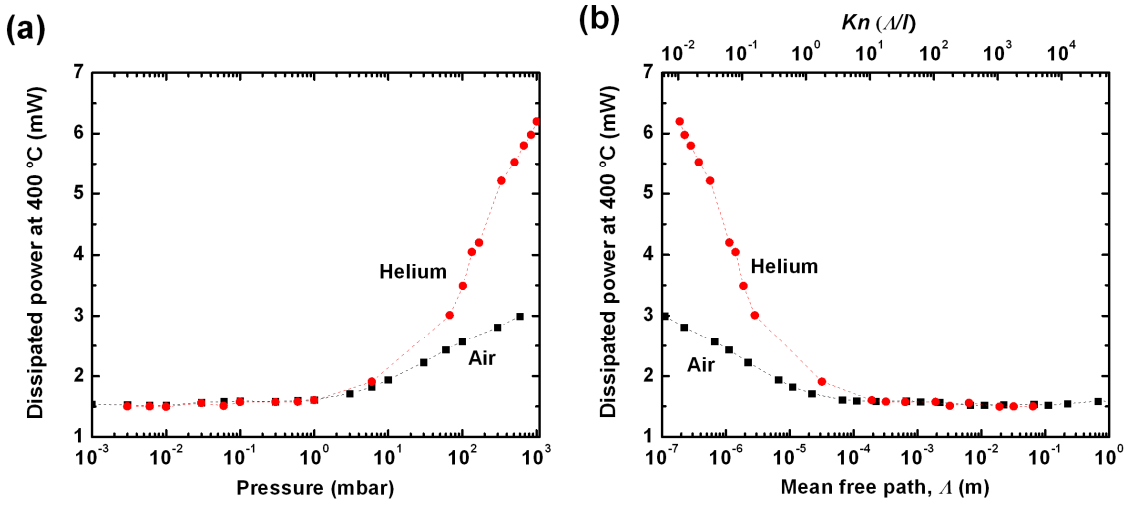


Figure 5.2 (a) Dissipated power in a heated AFM cantilever as a function of pressure (b) Dissipated power in a heated AFM cantilever as a function of gas mean free path and corresponding *Kn* number for both air and helium where the cantilever heater temperature is held at 400 °C.

It is helpful to examine the pressure-dependence of heat flow into the two gases used by considering the molecular mean free path. With the ideal gas assumption, the molecular mean free path can be calculated by

$$\Lambda = \frac{k_B T_g}{\sqrt{2}\pi P_g d_g^{\,2}} \qquad (5.1)$$

where $k_B$ is the Boltzmann's constant, $T_g$ is temperature, $P_g$ is pressure, and $d_g$ is effective diameter of the gas molecule [5]. The molecular collisions between the cantilever heater and the gaseous medium are expected to drop near $Kn$ = 1, and we presume that heater size modulates the thermal conduction between the cantilever heater and the environment.

Figure 5.2(b) shows dissipated power in the cantilever as a function of calculated mean free path or corresponding $Kn$ when the cantilever heater temperature was held at 400 °C. Figure 5.2(b) shows results for both air and Helium. There is a transition from pressure-dependence to pressure-independence of thermal conduction from the cantilever heater at approximately $2 \times 10^{-5}$ m which is close to the cantilever heater size. Although the thermophysical properties of helium are significantly different to the properties of air, the transition of the thermal response is near $Kn$ = 1 for both air and Helium.

The observed transition from pressure-dependence to pressure-independence of the near $Kn$ = 1 can be explained as follows. When $Kn$ is equal to or greater than 1, i.e. the size of the heater becomes comparable to the molecular mean free path, the character of the heat exchange between the heater and the gaseous medium is changing from diffusive to stochastic, which is dominated by the frequency of the molecular collisions with the heater. While air and helium conductances may still show pressure-dependence near $Kn$ = 1, however, their relative contribution to the overall conductance become negligible and undetectable.

To summarize the experimental observations: at high vacuum, thermal conduction to the gas was negligible compared to thermal conduction through the cantilever legs; at

low vacuum, gas conductance increased such that higher power could be dissipated at a given temperature.

## 5.3 Heat Transfer Modeling

A simple model for heat flow within and from the cantilever was developed to guide a deeper understanding of the thermal interactions between the cantilever and its gaseous environment. The heat transfer model employed the thermal resistance network shown in Figure 5.3, following previously published analyses of heat transfer in heated microcantilevers [7,8,18]. Because the thermal resistance to heat flow away from the cantilever is greater than the thermal resistance to heat flow within the cantilever, it can be assumed that the cantilever temperature varies only along its length, and does not vary across the cantilever width or thickness. A one-dimensional finite difference heat transfer simulation was employed, where the cantilever was divided into 216 nodes. Thermal conduction between adjacent nodes was calculated using Fourier's law [19]. Temperature dependent thermal conductivity of doped silicon was adopted from literature values [20]. Each node was assigned a cantilever-gas thermal conductance, which was used as a fitting parameter. While the cantilever-gas conductance was constant for every position along the cantilever and independent of temperature, the heat flow from any given node into the surrounding gaseous medium was the product of the node temperature and the conductance. As was observed above, at 1 ATM, thermal conductance from the cantilever was linear with temperature over the entire temperature range, indicating that thermal radiation was small compared to thermal conduction. Natural convection was neglected as well; for micron-scale heat sources, buoyancy forces

are not sufficiently large to overcome viscous forces. For each simulation, an energy balance was performed on the system to check that the heat generated was equal to the heat leaving the cantilever. The predictions closely matched analytical solutions for a test case that assumed a known cantilever-gas conductance.

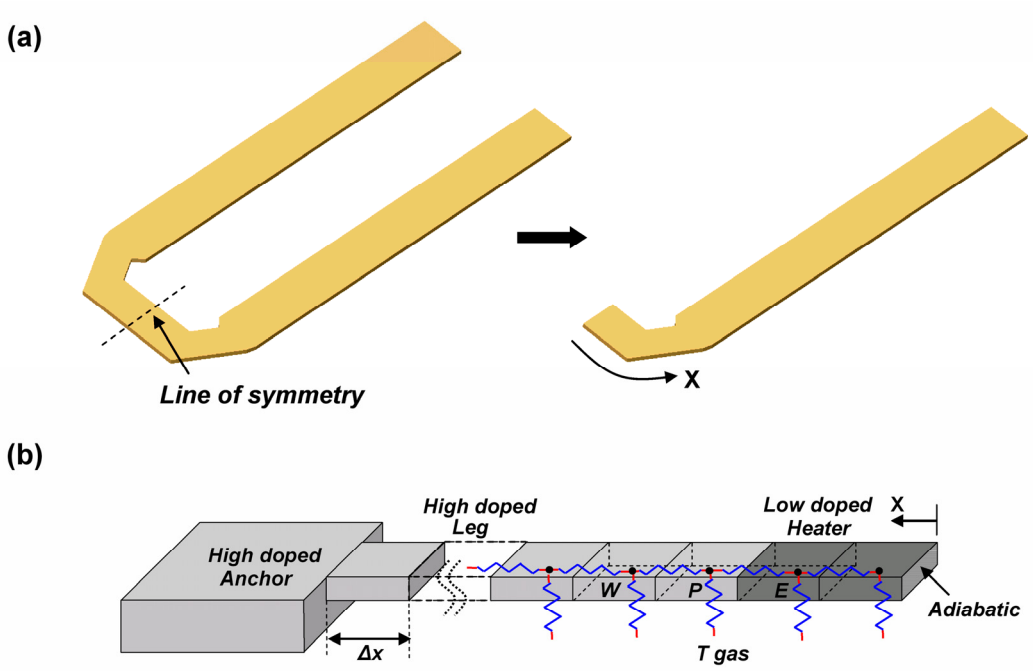


Figure 5.3 (a) 'U'- shape cantilever structure showing line of symmetry (b) One dimensional finite difference heat transfer model including solid conduction resistance between adjacent nodes and air conduction resistance.

Figure 5.4 shows the predictions for the temperature along the cantilever, along with measured temperature in the cantilever heater at 1 ATM. When the cantilever was heated to 2.97 mW in air at 1 ATM, the cantilever heater temperature was 400 ºC and the cantilever electrical resistance was 4.61 kΩ. Because more than 90 % of the cantilever electrical resistance occurs in the cantilever heater region, when the measured cantilever electrical resistance was 4.61 kΩ, the cantilever heater region was at 400 ºC regardless of the fraction of heat that flowed into the nearby gas vs. down the legs of the cantilever. In Figure 5.4(a) and (b), local temperature along the cantilever changes exponentially [21]

except near the heater region. The temperature drop along the cantilever is more significant with helium than with air due to the difference in thermal conductivity between the gases. As pressure decreases, the cantilever-gas conductance decreases, and less power is required to produce a fixed temperature.

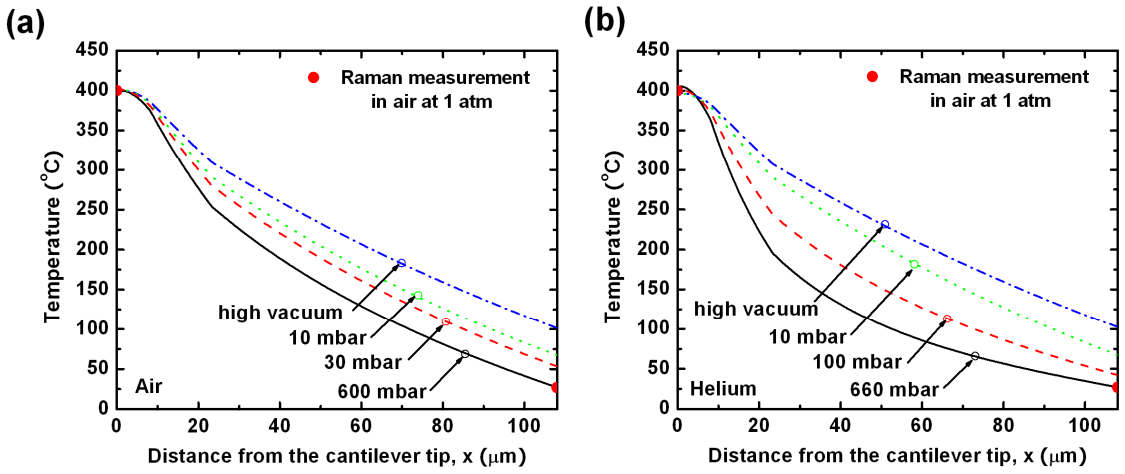


Figure 5.4 Simulated temperature distribution in the heated cantilever at different pressure in (a) air and (b) helium.

Figure 5.5 shows measured and predicted conductances from the cantilever at 400 ºC in air and Helium, with good agreement between simulation and measurement. The experimental values for conductance are simply the cantilever heating power divided by temperature difference between the heater and the UHV chamber. The simulated conductance was found as the best fit within the simulation to the experimentally measured temperature and power. Once the best fit was found, the total conductance from each node could be divided into both solid conductance along the cantilever and gas conductance. The plots of Figure 5.5 show these values for both air and Helium. Measured and simulated conductances are pressure-dependent when $Kn < 1$ and become pressure-independent when $Kn > 1$. Both air and helium show the similar trend except

the solid conductance. While the solid conductance in air decreases, the solid conductance in helium increases with decreasing pressure.

When $Kn < 1$, simulated solid conductance is not constant since the temperature distribution along the cantilever depends upon pressure. Simulation results using air as gas medium show that air conductance is 2.67 μW/K corresponding to 1mW power at atmospheric pressure. As pressure decreased, air conductance decreased to 0.155 μW/K or less at 1 mbar and below where it became negligible compared to solid conductance. For the helium, solid conductance also shows pressure-dependence only when $Kn < 1$ and the simulated gas conductance varied between 13.76 μW/K at atmospheric pressure and 0.174 μW/K or less at 1 mbar and below.

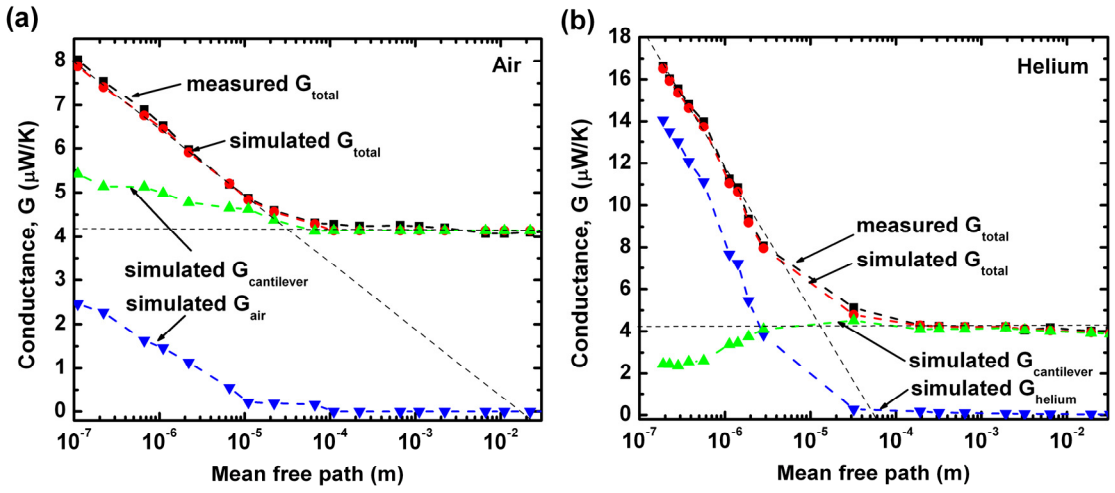


Figure 5.5 Simulated conductances show good agreement with measurements with the microcantilever in (a) air and (b) helium. Finite difference heat transfer simulation fits the air conductance to cantilever power, electrical resistance, and temperature.

To verify that thermal radiation was not significant, the simulations were performed with and without thermal radiation between the cantilever and the environment. The cantilever was assumed to be a black body and the radiative exchange between each node and the environment was evaluated using the Stefan-Boltzmann's law

[19]. From simulation, heat transfer due to thermal radiation was 20 μW and total power dissipation was 1.59 mW at high vacuum. Thermal radiation will not exceed 1.3 % of the total power dissipation regardless of pressure when the cantilever heater temperature is held at 400 ºC. At high vacuum, which is $10^{-5}$ mbar for air and $10^{-3}$ mbar for Helium, thermal radiation will exceed 6.5 % of the total power at 1000 ºC. When operated in air at 1 ATM, thermal radiation accounts for 0.5 % of the total power when the cantilever heater region is 400 ºC and thermal radiation will exceed 2 % of the total power at 1000 ºC. For operation in air at 1 ATM, the cantilever temperature should exceed 1850 ºC in order for thermal radiation to account for more than 10 % of the dissipated power. This temperature would be well above the melting temperature of silicon.

For microfabricated Pirani gauges, the gap distance between heater and heat sink is typically considered as the characteristic length scale and the device size is overlooked since the gap distance is kept shorter than the heater size. In contrast, this chapter examines a device where the heater size has a dominant effect. While microfabricated Pirani sensors are designed to minimize solid conductance, the current microcantilevers have solid conductance comparable to or higher than gas conductance. The microcantilever exhibits pressure-dependent power dissipation near atmospheric pressure, which is out of range for traditional Pirani gauges.

In this chapter, the heated microcantilever was configured in the UHV chamber with 500 μm separation so that the cantilever hardly feels the presence of the substrate. This heated cantilever needs to be located in proximity of the substrate and be engaged for application such as UHV tDPN. Since the presence of the substrate in proximity greatly affect heat transfer physics around the cantilever, more detailed experiments and

simulations are required. The gap distance between the cantilever and the substrate will be much smaller than the heater size such that gap distance will be system characteristic length and used for *Kn* number.

## 5.4 Summary and Conclusions

This chapter reports the thermal and electrical characteristics of a heated microcantilever in air and helium over a wide range of pressures. The cantilever heater size modulates thermal conductance between the cantilever and its gaseous surroundings; and the Knudsen number, *Kn*, characterizes this thermal conductance. When $Kn < 1$, thermal transport from the cantilever heater depends upon gas pressure, and when $Kn > 1$, thermal transport from the cantilever heater remains constant. The change in the thermal conductance regime associated with a microcantilever heater can be universally described by *Kn* for different gas species. This measurement of thermal conductance around $Kn = 1$ may aid the design of future micro Pirani and other thermal MEMS sensors. Moreover, this measurement enables research into UHV applications of heated AFM cantilevers.

## 5.5 References


[1] D. G. Cahill, W. K. Ford, K. E. Goodson, G. D. Mahan, A. Majumdar, H. J. Maris, R. Merlin, and S. R. Philpot, "Nanoscale thermal transport," *Journal of Applied Physics*, vol. 93, pp. 793-818, 2003.

[2] R. Puers, S. Reyntjens, and D. D. Bruyker, "The NanoPirani - an extremely miniaturized pressure sensor fabricated by focused ion beam rapid prototyping," *Sensors and Actuators A*, vol. 97-98, pp. 208-214, 2002.

[3] M. Doms, A. Bekesch, and J. Mueller, "A microfabricated Pirani pressure sensor operating near atmospheric pressure," *Journal of Micromechanics and Microengineering*, vol. 15, pp. 1504-1510, 2005.

[4] J. Chae, B. H. Stark, and K. Najafi, "A micromachined Pirani gauge with dual heat sinks," *IEEE Transactions on Advanced Packaging*, vol. 24, pp. 619-625, 2005.

[5] E. H. Kennard, *Kinetic Theory of Gases*, New York: McGraw-Hill, 1938.

[6] G. Binnig, M. Despont, U. Drechsler, W. Häberle, M. Lutwyche, P. Vettiger, H. J. Mamin, B. W. Chui, and T. W. Kenny, "Ultrahigh-density atomic force microscopy data storage with erase capability," *Applied Physics Letters*, vol. 76, pp. 1329-1331, 1999.

[7] W. P. King, T. W. Kenny, K. E. Goodson, G. L. W. Cross, M. Despont, U. Dürig, H. Rothuizen, G. Binnig, and P. Vettiger, "Atomic force microscope cantilevers for combined thermomechanical data writing and reading," *Applied Physics Letters*, vol. 78, pp. 1300-1302, 2001.

[8] W. P. King, T. W. Kenny, K. E. Goodson, G. L. W. Cross, M. Despont, U. T. Dürig, H. Rothuizen, G. Binnig, and P. Vettiger, "Design of atomic force microscope cantilevers for combined thermomechanical writing and thermal reading in array operation," *Journal of Microelectromechanical Systems*, vol. 11, pp. 765-774, 2002.

[9] L. A. Pinnaduwage, A. Gehl, D. L. Hedden, G. Muralidharan, T. Thundat, R. T. Lareau, T. Sulchek, L. Manning, B. Rogers, M. Jones, and J. D. Adams, "A microsensor for trinitrotoluene vapour," *Nature*, vol. 425, pp. 474, 2003.

[10] W. P. King, T. W. Kenny, and K. E. Goodson, "Comparison of thermal and piezoresistive sensing approaches for atomic force microscopy topography measurements," *Applied Physics Letters*, vol. 85, pp. 2086-2088, 2004.

[11] P. E. Sheehan, L. J. Whitman, W. P. King, and B. A. Nelson, "Nanoscale deposition of solid inks via thermal dip pen nanolithography," *Applied Physics Letters*, vol. 85, pp. 1589-1591, 2004.

[12] B. A. Nelson, W. P. King, A. Laracuente, P. E. Sheehan, and L. J. Whitman, "Direct deposition of continuous metal nanostructures by thermal dip-pen nanolithography," *Applied Physics Letters*, vol. 13, pp. 033104, 2006.

[13] A. Passian, A. Wig, F. Meriaudeau, T. L. Ferrell, and T. Thundat, "Knudsen forces on microcantilevers," *Journal of Applied Physics*, vol. 92, pp. 6326-6333, 2002.

[14] A. Passian, R. J. Warmack, T. L. Ferrell, and T. Thundat, "Thermal transpiration at the microscale: A Crookes cantilever," *Physical Review Letters*, vol. 90, 2003.

[15] B. Gotsmann, and U. Dürig, "Experimental observation of attractive and repulsive thermal forces on microcantilevers," *Applied Physics Letters*, vol. 87, pp. 194102, 2005.

[16] N. Masters, W. Ye, and W. P. King, "The impact of sub-continuum gas conduction on the sensitivity of heated atomic force microscope cantilevers," *Physics of Fluids*, vol. 17, pp. 100615, 2005.

[17] B. W. Chui, T. D. Stowe, Y. S. Ju, K. E. Goodson, T. W. Kenny, H. J. Mamin, B. D. Terris, and R. P. Ried, "Low-stiffness silicon cantilever with integrated heaters and piezoresistive sensors for high-density data storage," *Journal of Microelectromechanical Systems*, vol. 7, pp. 69-78, 1998.

[18] W. P. King, "Design analysis of heated atomic force microscope cantilevers for nanotopography measurements," *Journal of Micromechanics and Microengineering*, vol. 15, pp. 2441-2448, 2005.

[19] F. P. Incropera and D. P. DeWitt, *Fundamentals of heat and mass transfer*, 4th ed., New York: Wiley, 2002.

[20] W. J. Liu, K. Etessam-Yazdani, R. Hussin, and M. Asheghi, "Modeling and data for thermal conductivity of ultrathin single-crystal SOI layers at high temperature," *IEEE Transactions on Electron Devices*, vol. 53, pp. 1868-1876, 2006.

[21] J. Lee, T. Beechem, T. L. Wright, B. A. Nelson, S. Graham, and W. P. King, "Electrical, thermal, and mechanical characterization of silicon microcantilever heaters," *Journal of Microelectromechanical Systems*, vol. 15, pp. 1644-1655, 2006.

# CHAPTER 6

# CHARACTERIZATION OF LIQUID AND GASEOUS MICRO- AND NANOJETS USING MICROCANTILEVER SENSORS

## 6.1 Introduction

Micro/nanoscale jets have a number of industrial and medical applications including microelectronics cooling [1,2], inkjet printing [3], precision manufacturing [4], drug delivery [5] and microsurgery [6,7]. While **O**(100-1000 μm) – scale high speed gaseous jets have been investigated as potential actuators for flow control applications, little work has been reported on free liquid and gaseous jets having characteristic scales that extend below 10 μm. As the jet diameter becomes comparable to or even smaller than the wavelength of the light source employed, optical metrology such as particle image velocimetry (PIV) and laser Doppler velocimetry may not be viable. Hot-wire anemometry (HWA) has been miniaturized using microfabrication techniques [8] but its size is still comparable to or larger than the nozzle diameters, such that hot-wire sensors could not be fully submerged into micro/nanoscale flows. Moreover, the hot-wire is generally too fragile to be interfaced with liquid jet environment. Flow visualization techniques such as Schlieren photography, interferometry, and shadowgraphy are also challenging even for liquid jets that have a distinctive refractive index compared to the ambient.

Recently, microcantilevers also have been used as metrology tools to measure fluid properties and investigate flow characteristics. Micromachined silicon cantilever beams have been applied in liquid flow volume sensing [9,10] and highly sensitive piezoresistive cantilevers have been introduced for measuring air flow velocity in a small pipe [11]. Microcantilevers immersed in viscous fluids have been characterized [12] and applied to measure viscous drag [13]. AFM cantilever based anemometers have been designed to measure gas and liquid flows with high spatial and temporal resolution and demonstrated turbulent flow measurements in both air and water [14]. Due to their high deflection sensitivity and small minimum detectable deflection in the sub-nm regime, microcantilevers are promising candidates for micro/nanojets flow characterization.

Among microcantilever sensing mechanisms, piezoresistive and thermal sensing are best suited for liquid and gaseous jets environment. With the liquid jet impingement, optical sensing using a laser and a position sensitive diode could generate spurious signals due to refraction in the liquid layer around the cantilever. Capacitive sensing usually requires electrode structures that could block the jet flow and limit cantilever deflection. Free standing structures are preferred for micro/nanojets metrology since they can be fully exposed to the jet environment. Piezoresistive sensing is well-suited for deflection, thrust, and velocity measurement for both liquid and gaseous micro/nanojets. Since a commercial piezoresistive cantilever was readily available, it was introduced to verify the working concepts. After that, customized piezoresisitve cantilevers could be fabricated considering problems associated with the commercial cantilevers. For heat flux measurements of micro/nanojets, heated cantilevers were introduced. By mimicking HWA, the heated cantilevers can interrogate the cooling capacity of micro/nanojets by

monitoring heat transfer from the integrated resistive heater to micro/nanojets environment.

This chapter presents novel metrology applications of microfabricated cantilevers to investigate micro/nanojet flows. The jets were generated from micromachined silicon nozzles defined in the chip plane, connected to a small-scale pressurized reservoir [15]. Liquid butane and gaseous nitrogen jets ejected from 1 to 12 μm diameter nozzles have been characterized with the microcantilever sensors. Piezoresistive cantilevers were used to extract jet thrust and velocity from the measured beam deflection and heated cantilevers were used to estimate either the heat transfer coefficient or cooling capacity of micro/nanojets.

## 6.2 Experiments

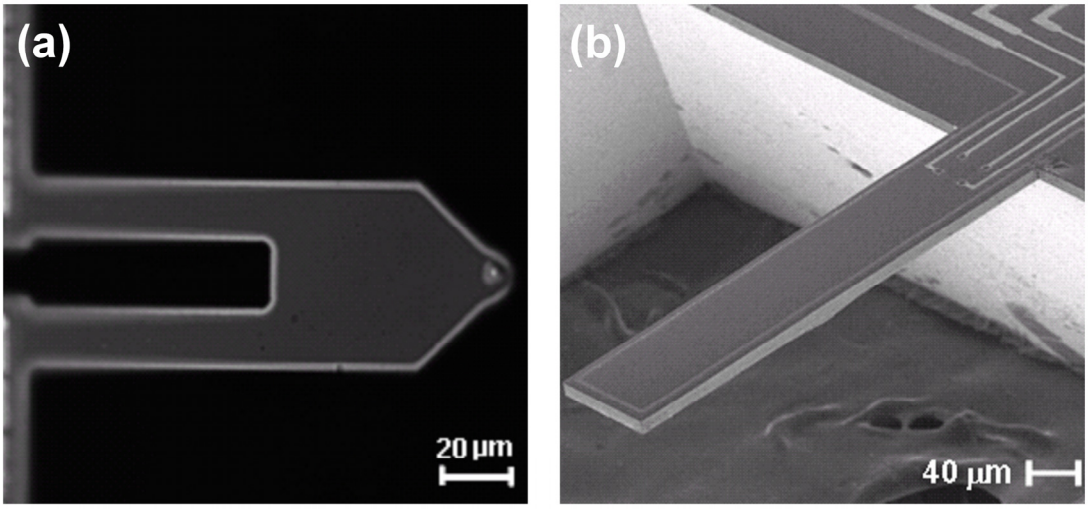


Figure 6.1 (a) Optical micrograph of a commercial piezoresistive cantilever and (b) scanning electron micrograph of a fabricated piezoresistive cantilever.

The experimental setup consisted of a high pressure fluidic system including microfabricated nozzles, optical diagnostic tools, high resolution positioning systems, and

microcantilever sensors. Figure 6.1 shows an optical micrograph of a commercially available piezoresisitve cantilever and a SEM image of a fabricated piezoresistive cantilever with an embedded full piezoresistive Wheatstone bridge to minimize temperature effects due to jet cooling while monitoring jet thrust.

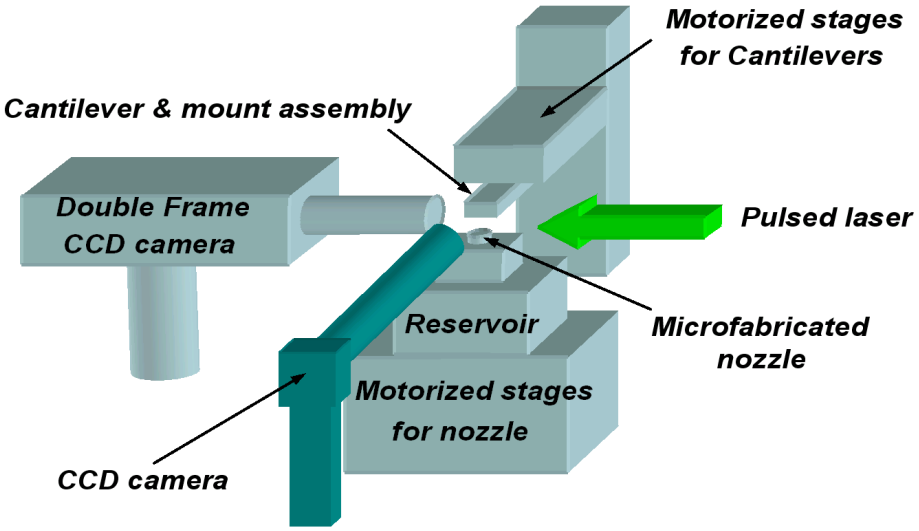


Figure 6.2 Experimental setup which enables to switch two different types of microcantilever sensors. Double frame CCD camera with a pulsed laser is used for shadowgraphy and normal CCD camera with co-axial illumination is configured for monitoring cantilever motion and coarse alignment. Both microcantilever sensor and microfabricated nozzle are mounted on independent 3-axis motorized stages.

Figure 6.2 shows the experimental setup that accommodates the two different types of microcantilever sensors. Both microcantilever and microfabricated nozzle are controlled by independent 3-axis motorized transverse stages with 50 nm resolution. The flow field is illuminated using a double-pulse ND:YAG laser (532 nm) where the pulse duration is on the order of 5 ns. Instantaneous images of the flow are captured using a PIV CCD camera having 1008 × 1018 pixels equipped with a high-magnification microscope lens. The lens system consists of a 50× infinity corrected microscope objective lens coupled with a 6.5:1 zoom lens having 0.7 to 4.5 zoom ratio for a total maximum magnification of 228×. The smallest achievable field of view measures 28 μm

on a side. For coarse alignment and quick inspection, another CCD camera in conjunction with a 12:1 zoom lens and a 5× microscope objective lens is configured.

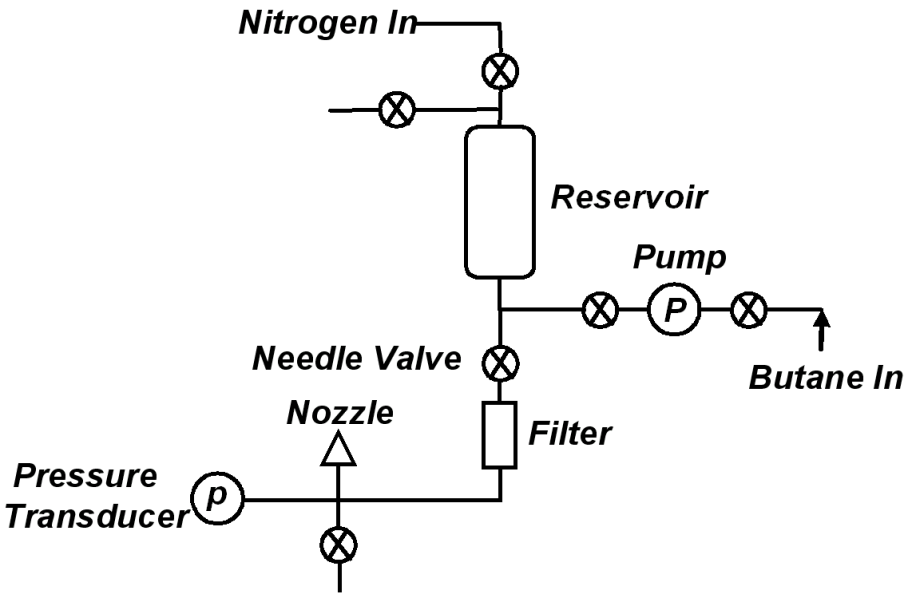


Figure 6.3 Fluidic system diagram. The maximum operating pressure of the present system is 34.5 MPa. The system was vacuumed to remove air as much as possible and then the liquid butane was pumped into the reservoir to the desired level. The system was then pressurized to the desired driving pressure using nitrogen. Both liquid and gaseous micro/nanojets can be driven with this fluidic system.

Measurements were made on liquid butane and gaseous nitrogen jets. Liquid butane has a surface tension of 0.012 N/m and a vapor pressure of 0.22 MPa at standard temperature and pressure. Figure 6.3 shows the constructed fluidic system which can generate high-speed submicron-scale jets. In this system, nitrogen was used for pressurizing. The maximum operating pressure of the present system was 34.5 MPa. The system was vacuumed to remove air as far as possible and then the liquid butane was pumped into the reservoir to the desired level. The system was then pressurized to the desired driving pressure using nitrogen. The microfabricated nozzle was directly connected to the reservoir and designed to minimize the volume of possible nitrogen

pockets. With the needle valve to the liquid butane supply closed, gaseous nitrogen jets could be driven.

Once the position of the nozzle and reservoir assembly was fixed, the piezoresistive cantilevers were brought close to the jet and scanned over the entire effective flow field. The pre-calibrated commercial piezoresistive cantilever with its single piezoresistor was configured in an off-chip Wheatstone bridge, whose output signal was amplified by a differential amplifier. The cantilevers with embedded piezoresistive Wheatstone bridge were directly interfaced with the measurement equipment. The heated cantilever was fixed after alignment to the jet such that the heating element near its tip could be fully exposed to the jet environment during jet impingement. Since the resistance change of the heated cantilever was much larger than that of the piezoresistive cantilever, measurement were done with a voltage divider having one off-chip resistor connected in series to the cantilever heater. All cantilever types were powered by a Keithley SourceMeter 2400 and monitored by an Agilent 34401A multimeter. Both liquid and gaseous jets were tested using two different types of microcantilevers.

### 6.3 Cantilever Calibration

The experimental procedure began with calibration of the microcantilever sensors. The temperature of the liquid butane jet is well below room temperature while the temperature of the gaseous nitrogen jet is close to room temperature. Since piezoresistive cantilevers with a single piezoresistor are sensitive to deflection and temperature, they must be calibrated independently for both. A calibration setup was constructed using a

precise motorized micro-transverse stage and an optical microscope. Figure 6.4 shows the calibration results of a commercial piezoresistive cantilever configured in an off-chip Wheatstone bridge with applied deflection. The voltage from the Wheatstone bridge increases linearly with cantilever deflection. The calibration was repeated during liquid jet impingement. The deflection sensitivity with jet impingement was identical to that without jet impingement such that each output due to mechanical deflection and temperature change could be added together.

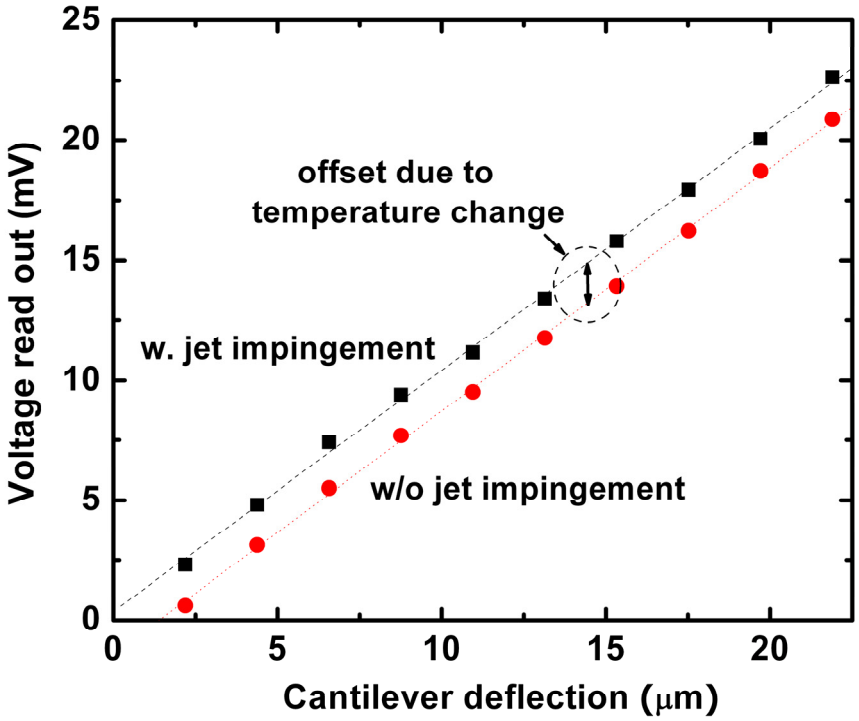


Figure 6.4 Voltage read out from a Wheatstone bridge as a function of deflection of the commercial piezoresistive cantilever with 2V bias voltage. Both calibrations with and without jet impingement show the same deflection sensitivity. The offset due to environmental temperature change should be considered to get actual cantilever deflection.

Silicon piezoresistors exhibit a sensitive TCR and any cantilever with a single piezoresistor must be temperature compensated to obtain the actual cantilever deflection. To this end, the commercial piezoresistive cantilever was placed in a cryostat to check the temperature dependence of the cantilever resistance as shown in Figure 6.5. The

sensor read out changes in a parabolic fashion with the sensor temperature under the assumption of thermal equilibrium between the cantilever and the mounting stage in the cryostat. The piezoresistive cantilever signal, $V_{piezo}$ is approximated by

$$V_{piezo} = S_\delta \delta + S_T (T_{sur} - T_c)^2 + c \qquad (6.1)$$

where $\delta$ is cantilever deflection, $T_{sur}$ is effective temperature of surroundings, $T_c$ is critical temperature where $\partial V/\partial T=0$, $S_\delta$ is deflection sensitivity, $S_T$ is temperature sensitivity, and $c$ is the maximum temperature offset at the critical temperature.

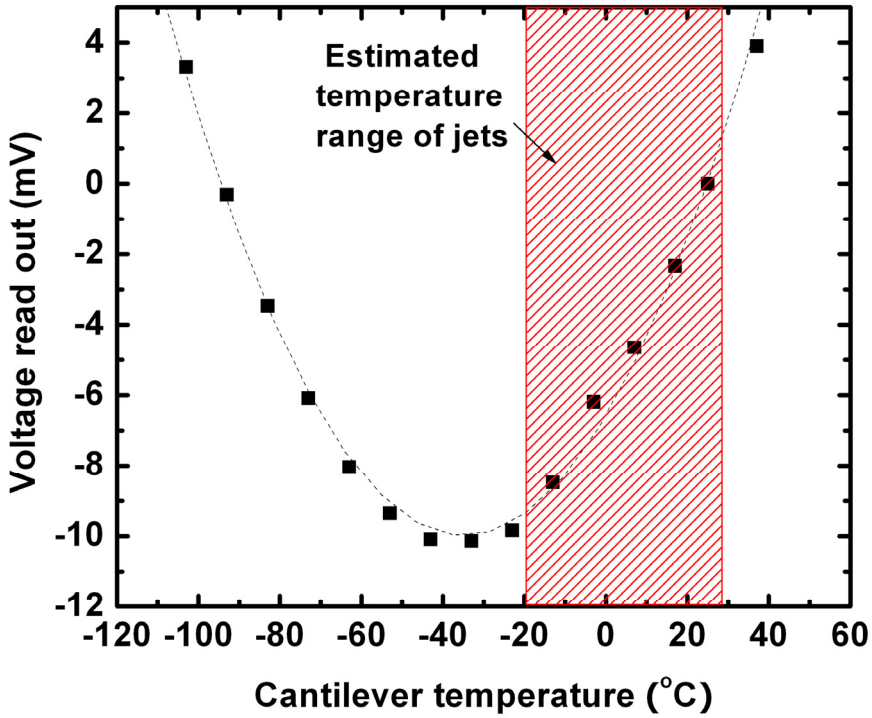


Figure 6.5 Temperature calibration results of a commercial piezoresistive cantilever. Wheatstone bridge outputs were measured at different cantilever temperatures in the cryostat. The sensor read out changes in a parabolic fashion with the sensor temperature under the assumption of thermal equilibrium between the piezoresistive cantilever and the mounting stage in the cryostat.

In contrast to the piezoresistive cantilever, the heated cantilever is less sensitive to the applied deflection compared to its temperature sensitivity such that only the temperature calibration is required. Following the characterization methods in chapter 2,

the resistance of the heated cantilever was calibrated with electrical heating at relatively low temperature where the cantilever shows positive TCR.

## 6.4 Results and Discussion

### 6.4.1 Piezoresistive cantilever sensor

Piezoresistive cantilevers were employed first to estimate the thrust and velocity of the micro/nanojets. The piezoresistive cantilever was scanned over the effective flow field of both liquid and gaseous micro/nanojets. During scanning, the sensor outputs were recorded and processed to extract the actual deflection of the cantilever using the aforementioned calibration results. Then, cantilever deflections were used to extract jet thrusts and velocities.

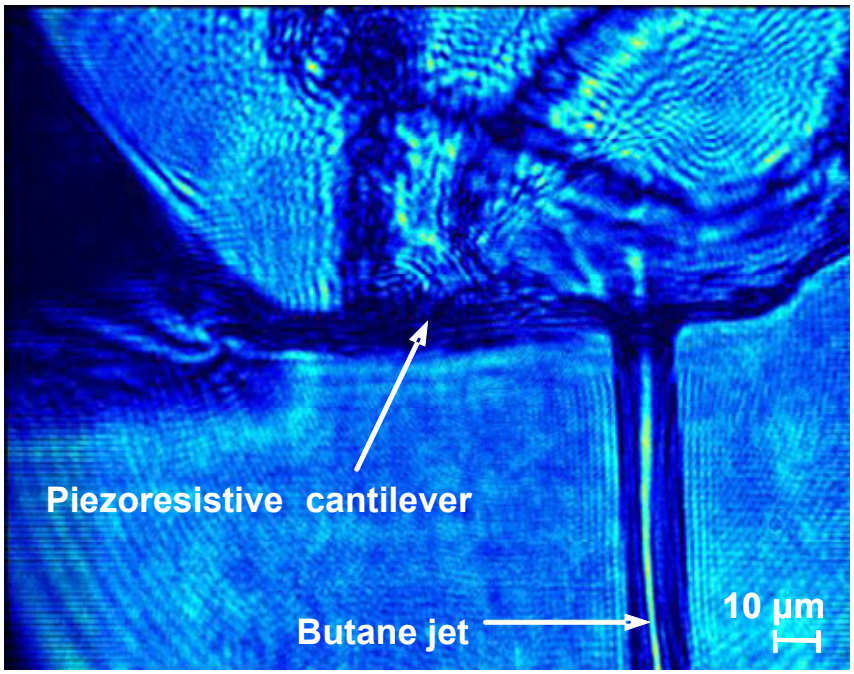


Figure 6.6 Piezoresistive cantilever deflects when the liquid butane jets impinge on the bottom surface of the cantilever. Small portion of the butane jets still have vertical direction velocity components after impinging on the piezoresistive cantilever. Momentum of liquid jets is not fully transferred to the cantilever when the nozzle diameter is comparable to the cantilever width.

Figure 6.6 shows the commercial piezoresistive cantilever impinged by a liquid butane jet from a 12 μm diameter nozzle. The cantilever shows a significant deflection of about 20 μm when the liquid jet impinges on its bottom side. The liquid butane jet still had a small portion of vertical direction velocity component after impinging on the cantilever. We conclude that the vertical momentum of the liquid jet was not fully transferred to the cantilever.

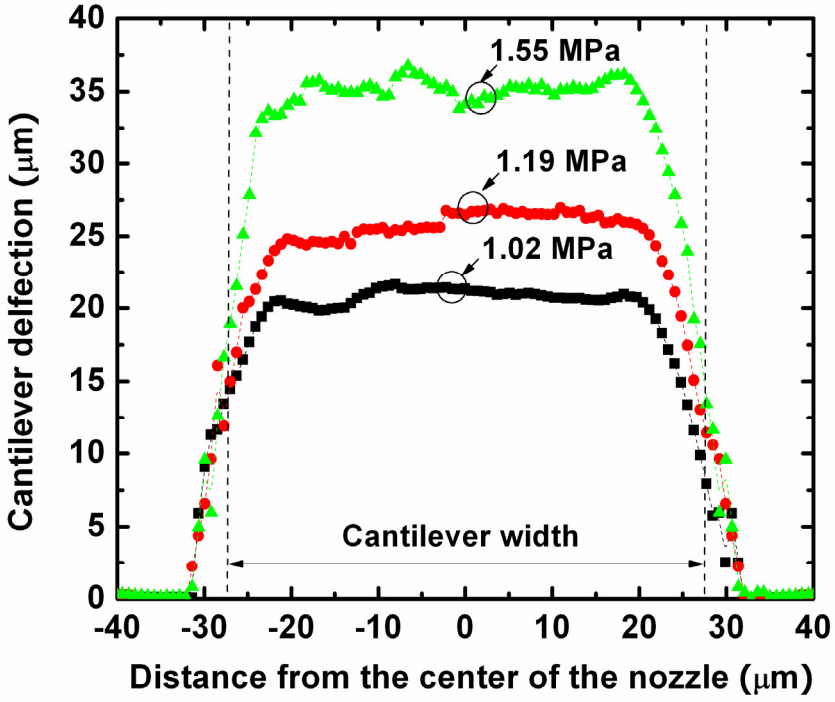


Figure 6.7 Deflection of the commercial piezoresistive cantilever as the cantilever is traversed through liquid butane jets where butane microjets are generated from a 6 μm microfabricated nozzle with 130 μm separation between the cantilever and the nozzle. Each deflection curve has a plateau which indicates that the cantilever deflection is nearly constant once the jets are blocked completely by the cantilever.

Figure 6.7 shows the measured cantilever deflection as the cantilever is traversed through liquid butane jets generated from a 6 μm microfabricated nozzle with 130 μm separation between the cantilever and the nozzle. Each deflection curve has a plateau which indicates that the cantilever deflection is nearly constant once the liquid butane jet is blocked completely by the cantilever. Therefore, there is negligible effect of the

torsional motion on the cantilever deflection signal. Wide cantilevers are better for characterizing averaged properties but may limit spatial resolution of the measurements.

When the liquid butane jet is aligned to the center of the cantilever in the scanning direction, the force exerted on the cantilever due to the jet impingement, $F_{jet}$ can be inferred by

$$F_{jet} = \frac{2L^3}{d^2(3L-d)} k\delta \qquad (6.2)$$

with the assumption that the piezoresistive cantilever has a uniform rectangular cross-section from its free end to clamped base and experiences pure bending. In addition, the cantilever needs to remain relatively flat, surface tension is neglected, and any possible unsteady effect such as mass accumulation and evaporation is not considered. $L$ is the cantilever length, $d$ is the distance from the clamped base to the center of the jet, and $k$ is the spring constant [16]. The distance $d$ was measured with a PIV CCD camera and the spring constant ($k$ = 1.4 N/m) of the commercial piezoresistive cantilever was obtained using an AFM system before jet testing. If the cantilever deflection is not significant, the jet velocity, $V_{jet}$ could be also inferred by

$$V_{jet} = \sqrt{\frac{F_{jet}}{\rho A_{jet}}} \qquad (6.3)$$

where $\rho$ is the density of the fluid, and $A_{jet}$ is the cross-sectional area of the jet [17]. It should be noted that jet velocity determination herein is too simplified for the jet from the nozzle of which size is comparable to the cantilever width since the effects neglected above may play a role to affect the piezoresistive readouts. For example,

momentum loss due to the large cantilever deflection should be considered for better estimation of force and velocity since the measured deflection was not negligible.

Equation (6.2) and (6.3) are combined to estimate the jet velocity. Two assumptions are made to estimate the jet velocity. First, the cross-section of the liquid jet is a perfect circle with a diameter measured using a PIV CCD camera. Second, the density of the liquid jet does not change much with the driving pressure after the jet is ejected from the nozzle. However, the analytical model greatly simplified the cantilever geometry as a rectangular one and the jet impingement thrust as a point load. In analytical model, it is difficult to incorporate distributed load in three dimensional Cartesian coordinate. Moreover, the analytical beam bending given by Equation (6.2) employed a simple approximation for the curvature which limits validity of the model for small angular displacement. Therefore, finite element model will be more appropriate for large deflection resulting from the high speed jet impingement. To improve problems associated with the analytical model, a finite element simulation was performed to better estimate the cantilever tip deflection at a given jet velocity. In the FEM simulation, the jet impingement was modeled as a distributed load on a circular area defined by the liquid jet and density of the butane was used to calculate the distributed load.

FEM simulation confirmed that the simplified geometry can be used as long as the cantilever stiffness is same. FEM results with distributed load were nearly identical to those with point load such that simplified force loading in the analytical model was validated. Therefore, FEM results with linear solver were similar to results from the analytical model. However, both the FEM with linear solver and the analytical model might not be valid for the experimented large deflections. For larger cantilever deflection,

the lateral displacement as well as the vertical displacement becomes non-negligible such that non-linearity increases. To check nonlinearity associated with large deflections, the FEM simulation was performed with nonlinear solver. Figure 6.8 shows the cantilever tip deflection as a function of the jet velocity using both linear and nonlinear FEM solver. As mentioned earlier, the solution from nonlinear model shows good agreement with the analytical model mainly due to the similar cantilever stiffness. Therefore, equation (6.2) is applicable to the commercial piezoresistive cantilever even though it simplifies the shape of the cantilever and uses the jet thrust as a point load. However, solution considering nonlinearity associated with large deflection starts to deviate from the analytical model as jet velocity increases. For example, the error between linear and nonlinear model is about 6.5 % when the jet velocity is 65 m/s.

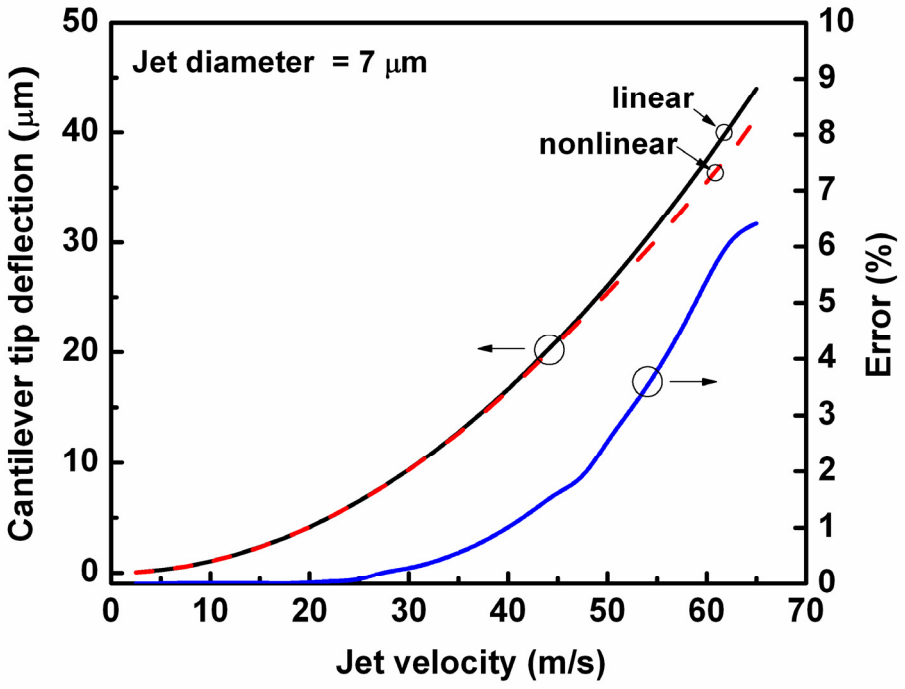


Figure 6.8 Finite element simulation results showing the cantilever tip deflection at a given jet velocity. Both linear and nonlinear solvers are used to calculate tip deflection and % error between linear and nonlinear solution is also included in another y-axis on the right. Local position of the jet impingement on the cantilever is based on experiments and density of the liquid butane is used to calculate the distributed load.

Since the measured cantilever deflections are somewhat large, the FEM results better estimate the jet velocity. Figure 6.9 compares the calculated jet velocities with jet velocities obtained using laser shadowgraphy. The piezoresistive cantilever measurements have no more than 12.5 % error compared to shadowgraphy results. When the driving press is less than 0.9 MPa, the FEM results agree to the results from the analytical model. For higher driving pressures, the nonlinear effect becomes important such that the cantilever becomes stiffer and two models start to deviate. Even the more realistic FEM model is used, there is still big discrepancy between the shadowgraphy results and the calculation based on the piezoresistive cantilever measurement.

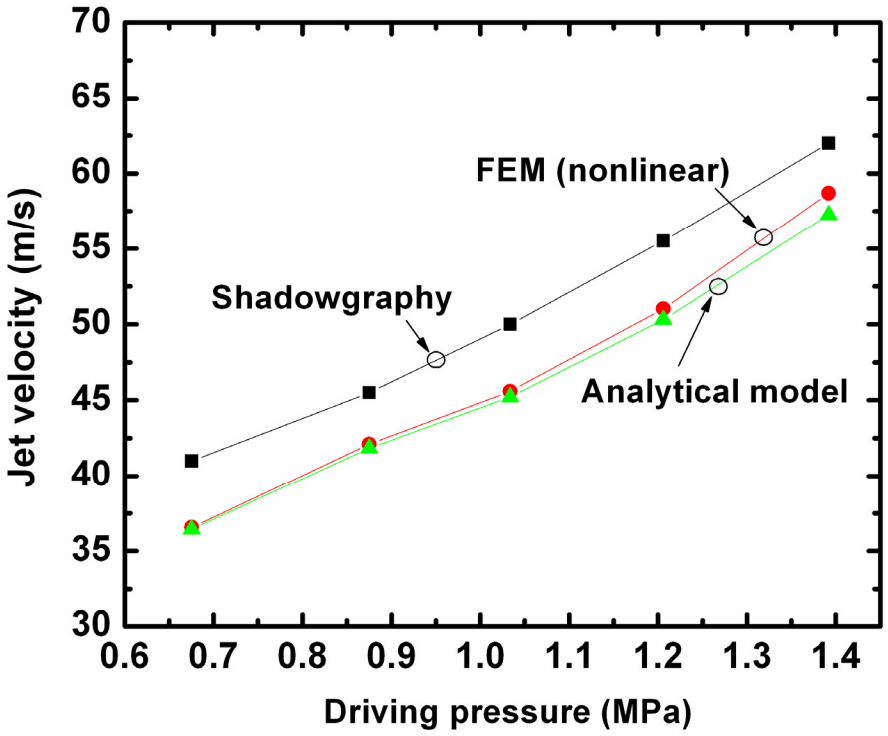


Figure 6.9 Measured jet velocities as a function of the driving pressure extracted from the piezoresistive cantilever measurements and shadowgraphy.

It should be noted that both the FEM simulation and the analytical model can not take into account the partial momentum transfer from the jet to the cantilever when the

nozzle diameter is comparable to the size of the cantilever. Correction to the jet momentum due to the partial momentum transfer might be necessary for the microjet from large diameter nozzles or with high velocity. To minimize error originated from the partial momentum transfer, it is recommended to limit the cantilever deflection after experiments decide the allowable cantilever deflection. To sense microjets with high momentum within the limited cantilever deflection, the jet impingement can be moved away from the free end. Figure 6.10 shows simulated cantilever tip deflection as a function of the jet velocity at different local position of the jet impingement. Microjet having higher momentum can be measured within the limited cantilever deflection by offsetting the local position of the jet impingement.

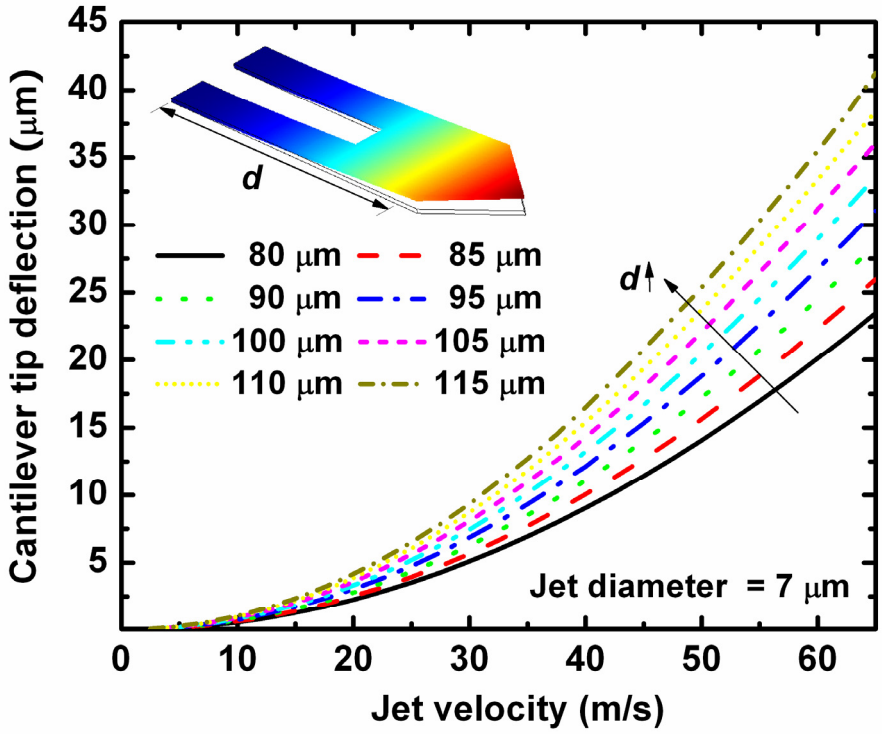


Figure 6.10 Cantilever tip deflection as a function of the jet velocity at different local position of the jet impingement. Jet having higher momentum can be measured within the limited cantilever deflection by offsetting the local position of the jet impingement.

Gaseous micro/nanojets were also tested using the same fluidic system with the needle valve for liquid butane supply closed. Figure 6.11 shows the measured cantilever deflection as the commercial piezoresistive cantilever is traversed through gaseous nitrogen jets generated from a 1 μm microfabricated nozzle with 27 μm separation distance between the cantilever and the nozzle. The driving pressure varies from 6.8 to 10.6 MPa. In contrast to the liquid jet, the gaseous jet shows almost symmetric deflection curves having a maximum deflection when the cantilever is aligned to the center of the nozzle. As an example, Figure 6.11(b) shows a Gaussian-like deflection curve when the driving pressure is 9.65 MPa (see cross-section AA´ in Figure 6.11(a)).

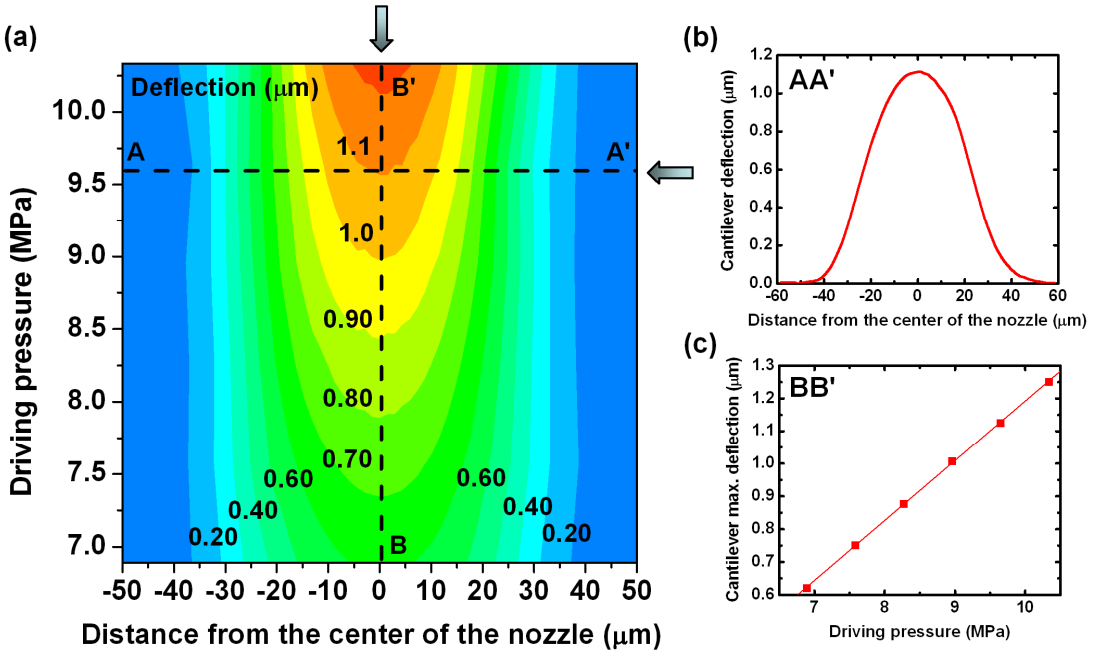


Figure 6.11 (a) Contour plot of deflection of the piezoresistive cantilever as the cantilever is traversed through gaseous nitrogen jets. (b) A Gaussian-like deflection curve when the driving pressure is 9.65 MPa. (c) Linear relationship between cantilever maximum deflection and driving pressure. Gaseous nitrogen jets are generated from a 1 μm diameter nozzle with 27 μm separation between the cantilever and the nozzle.

Figure 6.11 also shows that the effective flow field of the gaseous nitrogen jet does not change within the tested pressure range. The effective flow field of gaseous nitrogen jet was much wider than that of liquid butane jet even though a much smaller

diameter nozzle was configured. It can be inferred that the gaseous jet sprays out while the cross-section of the liquid jet remains uniform as shown in Figure 6.12 even though the gaseous jet can not be visualized at the moment.

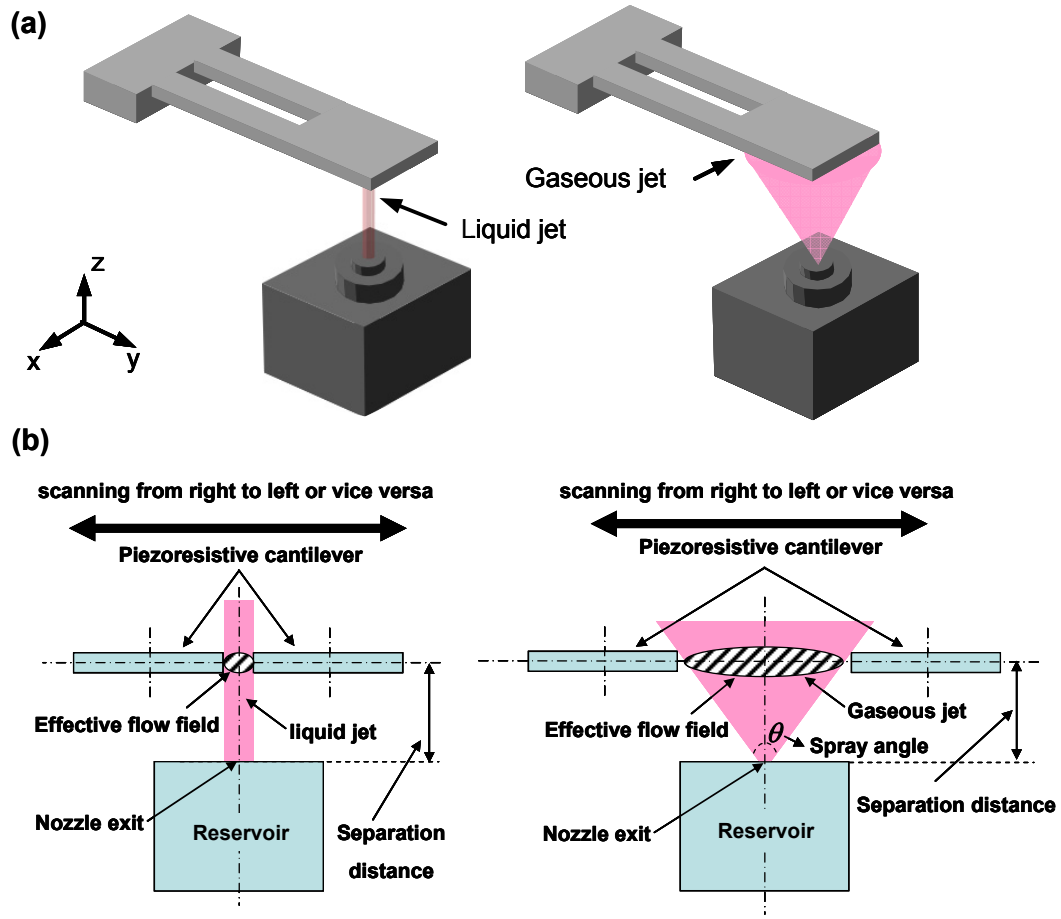


Figure 6.12 (a) Configuration of nozzle and cantilever for liquid and gaseous jets. In contrast to liquid jets, gaseous jets tend to spray out. (b) Gaseous jets can have much larger effective flow field than liquid jet even with smaller diameter nozzles.

With the cantilever dimension and the measured jet flow field, the spray angle of the gaseous nitrogen jet, $\theta_{spray}$ can be defined as

$$\theta_{spray} = 2 \times \arctan\left(\frac{r_{jet} - r_{nozzle}}{d_{separation}}\right) \qquad (6.4)$$

where $r_{jet}$ is the radius of the jet flow, $r_{nozzle}$ is the radius of the microfabricated nozzle, and $d_{separation}$ is the separation distance between the cantilever and the nozzle. For the tested pressure range from 6.8 to 10.6 MPa, the radius of effective flow field measured about 25 μm and separation distance was 27 μm. We conclude that the 1 μm diameter nozzle has a spray angle of about 84 degree for gaseous nitrogen jets.

Figure 6.11(c) shows the linear relationship between the cantilever maximum deflection and the driving pressure using gaseous nitrogen jets from the 1 μm diameter nozzle. Once the driving pressure is fixed, the cantilever maximum deflection can be estimated. Local thrust and velocity estimations for gaseous jets are not possible since the interaction between the cantilever and gaseous jets is more complicated because the gaseous jet sprays out and impinges on the cantilever with a finite angle other than 90 degree. If the piezoresistive cantilever approaches to the nozzle exit within sub-micron proximity, the effective field of gaseous jets becomes small such that the thrust and velocity can be characterized as local flow properties.

### 6.4.2 Heated cantilever sensor

Heated cantilevers introduced in chapter 2 can detect changes in power dissipation and cooling capacity of micro/nanojets by heat transfer since heated cantilevers are very sensitive to small thermal agitation. The experiments above were repeated using a heated cantilever that has an integrated micro-heater near its free end to investigate the cooling capacity of the liquid and gaseous microjets and thermal transport between the cantilever heater and the impinging jet environment.

The heater region of the cantilever was aligned to and impinged by a liquid butane jet from a 10 μm diameter nozzle. Figure 6.13 shows that the resistance of the heated cantilever changes with the dissipated power in the cantilever with and without jet impingement. Without jet impingement, the results show typical nonlinear electrical properties of the heated cantilever [18]. When the liquid butane jet impinges upon the cantilever heater region, the cantilever can dissipate more power without significant temperature rise. Figure 6.13 also exhibits discontinuities representing local vaporization of a liquid butane droplet and each discontinuity is associated with a critical power. At each critical power, the cantilever electrical resistance and corresponding cantilever heater temperature increase all of a sudden and that critical power increases as the jet velocity increases.

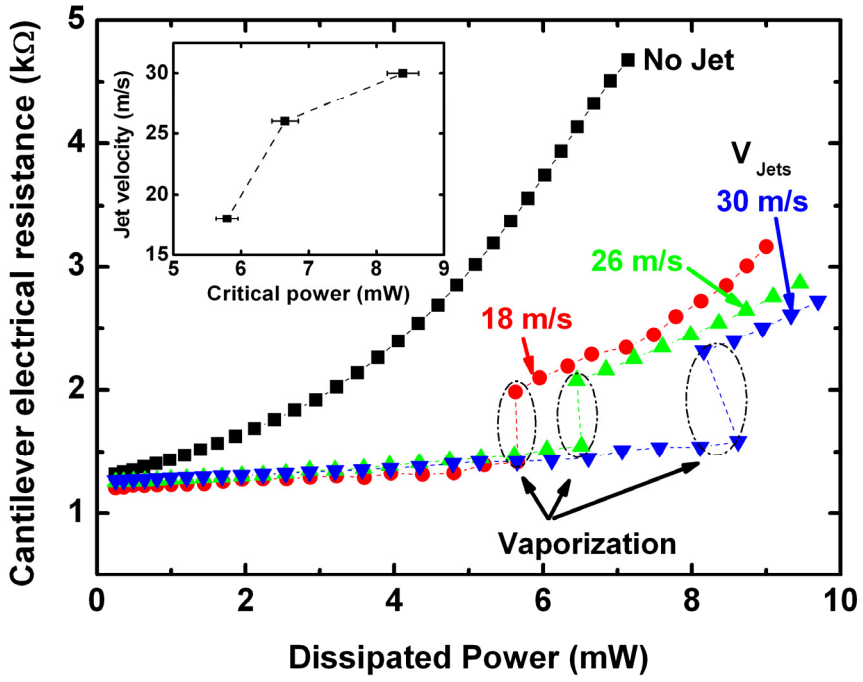


Figure 6.13 Resistance of a heated cantilever as a function of dissipated power with and without additional cooling by liquid microjets. Without jet impingement, the results show the typical nonlinear electrical resistance of the heated cantilever. With jet impingement, the cantilever can dissipate more power without significant temperature rise. There are discontinuities representing local vaporization of liquid butane droplet and each discontinuity is associated with a critical power. The inset shows the critical power increases as the jet velocity increases.

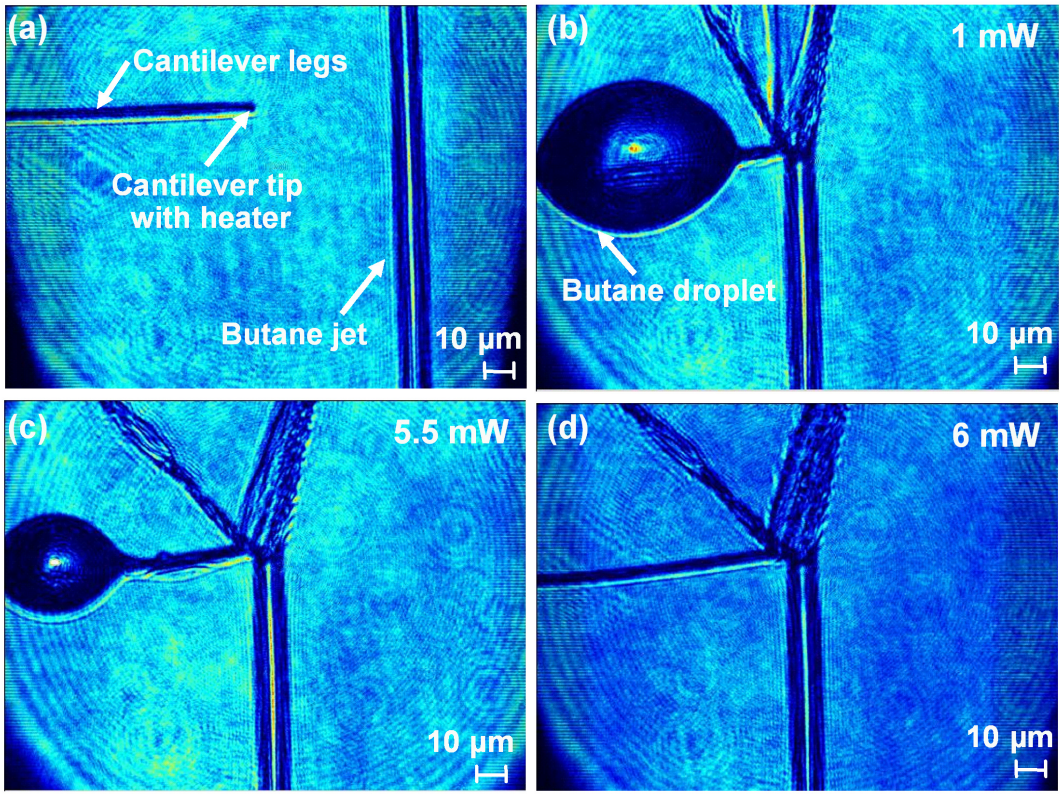


Figure 6.14 (a) The heated cantilever and liquid butane jets from a 10 µm diameter nozzle before the heating element is submerged into the butane jets. The liquid butane jets impinge on the heating element near free end of the cantilever at different cantilever powers where the measured jet velocity is 18 m/s. Cantilever powers are: (b) 1 mW (c) 5.5 mW, and (d) 6mW, respectively.

A liquid butane droplet is observed around the heated cantilever legs at lower power than the critical power. However, the droplet vaporizes and disappears at higher power as shown in Figure 6.14. Figure 6.14 (a) shows the heated cantilever and liquid butane jet from the 10 µm diameter nozzle before the cantilever heater is submerged in the butane jet. Figure 6.14 (b)-(d) show that the liquid butane jet impinges on the heating element near the free end of the cantilever at different cantilever powers where the measured jet velocity is 18 m/s. When the cantilever power is 5.5 mW or less, a liquid butane droplet is observed around the heated cantilever legs. As power increases, the size of the droplet tends to decrease. The butane droplet vaporizes completely when the cantilever power is increased beyond 6.0 mW. Before the liquid droplet vaporizes, the

cantilever is almost fully surrounded by the cold liquid jet environment and resistance versus power ($R$ vs. $P$) plots are independent of the jet velocity. Once the droplet vaporizes completely, the heated cantilever can dissipate more power at same electrical resistance as the jet velocity increases as shown in Figure 6.13. Measured power when the vaporization occurs definitely depends on the droplet size. However, it is not possible to separate the measured power into dissipation due to vaporization and dissipation due to impinging jet near the cantilever free end since we only measured total power dissipation.

Micromachined hot-wire flow sensors [8] have been developed by several research groups to provide high spatial resolution, better uniformity, fast time response, and mass productivity. They have a thin wire element that acts as both Joule heater and temperature sensor and two parallel prongs that support the wire element and act as electrical leads. In steady state operation, the power generated by joule heating is balanced by convection to the external flow and conduction through the support prongs. They are designed to minimize conduction heat loss through the support prongs in order to enhance sensitivity. The thermal measurement using the heated cantilever mimics HWA. Heated cantilevers can be operated with constant driving current or fixed heater temperature using appropriate feedback loops such that a constant temperature or a constant current anemometer can be constructed based on the heated cantilever. The heated cantilever herein has a resistive heater area sized 5 μm × 10 μm and the heater region was directly exposed to jet impingement. Therefore, gaseous jets that spray out or liquid jets from a nozzle larger than 10 μm are preferred to fully immerse the heater area in the jet environment. To measure liquid jets from much smaller nozzles, the heater size should be scaled down. In contrast to micromachined hot-wire sensors, a significant

amount of heat conducts through the cantilever legs and it depends upon the external environment. Therefore, a heat transfer simulation including relevant heat transfer mechanisms is required to estimate cooling capacity or heat transfer coefficients of microjets.

Using the thermal resistance network employed in previously published analyses of heat transfer in the heated cantilever [19-21], a one-dimensional finite difference heat transfer simulation was performed to estimate the thermal conductance – cooling capacity – via the microjets. With the cantilever heater temperature maintained at 150 °C, the thermal conductances between liquid butane jets and the cantilever heating element were 0.0197, 0.0231, and 0.0275 mW/K when the jets velocities were 18, 26, and 30 m/s, respectively. These numbers are comparable to heat transfer accompanied by phase change [22].

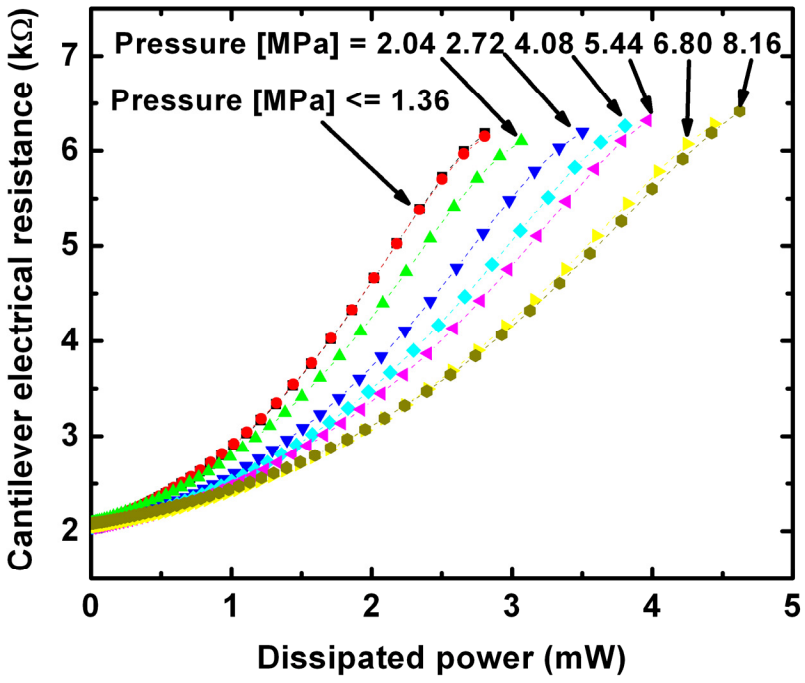


Figure 6.15 Cantilever electrical resistance as a function of dissipated power in the cantilever at various gaseous nitrogen jet driving pressures where a 10 μm diameter nozzle is used with 700 μm separation between the cantilever and the nozzle.

Heated cantilevers were also tested with gaseous nitrogen jets from the 10 μm diameter nozzle. Figure 6.15 shows the cantilever electrical resistance as a function of the dissipated power in the cantilever at various driving pressures where the heated cantilever is located 700 μm above the nozzle exit. First, the electrical responses of the heated cantilever remain unchanged as long as the driving pressure is less than 1.36 MPa. As the pressure increases, the $R$ vs. $P$ curves are shifted to higher powers such that the cantilever can dissipate more power at fixed cantilever heater temperature. At pressure higher than 8.16 MPa, the flow velocity of nitrogen jet becomes saturated and no more changes in the electrical response will be expected beyond this pressure. Since the heated cantilever is strongly sensitive to any change that affects the heat transfer, it can be inferred that the momentum of the nitrogen jet becomes negligible at pressures less than 1.36 MPa with a separation distance of 700 μm between the cantilever and the nozzle. The shifted $R$ vs. $P$ curves in the intermediate pressure ranges indicate the enhanced cooling capacity of nitrogen jets.

The gaseous nitrogen jet sprays out such that the effective flow field and momentum of the gaseous jet strongly depend on the separation distance between the cantilever and the nozzle. Therefore, the separation distance is a very important parameter required to explore for gaseous micro/nanojets.

## 6.5 Summary and Conclusions

This chapter demonstrates novel microcantilever based metrology for investigating both liquid and gaseous micro/nanoscale jets. Liquid butane and gaseous nitrogen jets generated from 1 to 12 μm diameter nozzles have been characterized with

piezoresistive and heated microcantilever sensors. Results show that the piezoresisitve cantilevers measure jet thrusts ranging from 30 to 75 μN and estimate jet velocities of 40-60 m/s during liquid butane microjets impingement from a 6 μm diameter nozzle. Estimated jet velocities agree to the shadowgraphy results within 12.5 %. More accurate velocity measurement can be made with nozzles having sub-micron diameter without any correction since the jet momentum will be completely transferred to the cantilever as the nozzle size becomes much smaller. The piezoresistive cantilever sensors can also investigate the effective flow field, estimate spray angle of the gaseous jet, and inspect nozzle clogging.

With the heated cantilever, local vaporization of butane droplets and the localized cooling capability of the liquid microjets were examined. Finite difference heat transfer simulations showed the cooling capacity of the liquid butane microjet was in the order of $10^{-5}$ W/K for single phase cooling. There was a critical power indicating vaporization of the liquid butane droplet and the critical power increased with jet velocity. The heated cantilever could also detect small changes in the jet velocity and flow rate of gaseous jets.

## 6.6 References


[1] E. N. Wang, L. Zhang, L. Jiang, J.-M. Koo, J. G. Maveety, E. A. Sanchez, K. E. Goodson, and T. W. Kenny, "Micromachined jets for liquid impingement cooling of VLSI chips," *Journal of Microelectromechanical Systems*, vol. 13, pp. 833-842, 2004.

[2] D. S. Kercher, J. Lee, O. Brand, M. G. Allen, and A. Glezer, "Microjet cooling devices for thermal management of electronics," *IEEE Transactions on Component and Packaging Technologies*, vol. 26, pp. 359-366, 2003.

[3] D. J. Hayes, D. B. Wallace, and W. R. Cox, "Microjet printing of solder and polymers for multi-chip modules and chip-scale packages," *Proc. of the SPIE - The international Society for Optical Engineering*, vol. 3830, pp. 242-247, 1999.

[4] O. D. Sibailly, F. R. Wagner, L. Mayor, and B. Richerzhagen, "High precision laser processing of sensitive materials by Microjet," *presented at Fourth International Symposium on Laser Precision Microfabrication*, 2003.

[5] D. A. Fletcher, D. V. Palanker, P. Huie, J. Miller, M. F. Marmor, and M. S. Blumenkranz, "Intravascular drug delivery with a pulsed liquid microjet," *Archives of Ophthalmology*, vol. 120, pp. 1206-1208, 2002.

[6] D. A. Fletcher and D. V. Palanker, "Pulsed liquid microjet for microsurgery," *Applied Physics Letters*, vol. 78, pp. 1933-1935, 2001.

[7] M. S. Blumenkranz, D. V. Palanker, D. Fletcher, and J. Miller, "A pulsed liquid microjet for ocular microsurgical applications.," *Investigative Ophthalmology & Visual Science*, vol. 42, pp. S717-S717, 2001.

[8] J. Chen and C. Liu, "Development and characterization of surface micromachined, out-of-plane Hot-wire anemometer," *Journal of Microelectromechanical Systems*, vol. 12, pp. 979-988, 2003.

[9] T. Nishimoto, S. Shoji, and M. Esashi, "Buried piezoresistive sensors by means of Mev Ion Implantation," *Sensors and Actuators, A*, vol. 43, pp. 249-253, 1994.

[10] V. Gass, B. H. Van der Schoot, and N. F. De Rooij, "Nanofluid handling by micro-flow sensor based on drag force measurement," *presented at IEEE Proc. MEMS*, NY, USA, 1993.

[11] Y. Su, A. G. R. Evans, A. Brunnschweiler, and G. Ensell, "Characterization of a highly sensitive ultra-thin piezoresistive silicon cantilever probe and its application in gas flow velocity sensing," *Journal of Micromechanics and Microengineering*, vol. 12, pp. 780-785, 2002.

[12] J. E. Sader, "Frequency response of cantilever beams immersed in viscous fluids with applications to the atomic force microscopy," *Journal of Applied Physics*, vol. 84, pp. 64-76, 1998.

[13] P. I. Oden, G. Y. Chen, R. A. Steele, R. J. Warmack, and T. Thundat, "Viscous drag measurements utilizing microfabricated cantilevers," *Applied Physics Letters*, vol. 68, pp. 3814-3816, 1996.

[14] S. Barth, H. Koch, A. Kittel, J. Peinke, J. Burgold, and H. Wurmus, "Laser-cantilever anemometer: A new high-resolution sensor for air and liquid flows," *Review of Scientific Instruments*, vol. 76, pp. 075110, 2005.

[15] N. Naik, C. Courcimault, H. Hunter, J. Berg, J. Lee, K. Naeli, T. Wright, M. Allen, O. Brand, A. Glezer, and W. King, "Microfludics for generation and characterization of liquid and gaseous micro- and nanojets," *Sensors and Actuators, A*, vol. 134, pp. 119-127, 2007.

[16] S. H. Crandall, N. C. Dahl, and T. J. Lardner, *An Introduction to the Mechanics of Solids*, 2nd ed.

[17] B. R. Munson, D. F. Young, and T. H. Okiishi, *Fundamentals of Fluid Mechanics*, 4th ed.: Wiley, 2002.

[18] M. Despont, J. Brugger, U. Drechsler, U. Dürig, W. Häberle, M. Lutwyche, H. Rothuizen, R. Stutz, R. Widmer, G. Binnig, H. Rohrer, and P. Vettiger, "VLSI-NEMS chip for parallel AFM data storage," *Sensors and Actuators, A*, vol. 80, pp. 100-107, 2000.

[19] W. P. King, T. W. Kenny, K. E. Goodson, G. L. W. Cross, M. Despont, U. Dürig, H. Rothuizen, G. Binnig, and P. Vettiger, "Atomic force microscope cantilevers for combined thermomechanical data writing and reading," *Applied Physics Letters*, vol. 78, pp. 1300-1302, 2001.

[20] W. P. King, T. W. Kenny, K. E. Goodson, G. L. W. Cross, M. Despont, U. T. Dürig, H. Rothuizen, G. Binnig, and P. Vettiger, "Design of atomic force microscope cantilevers for combined thermomechanical writing and thermal reading in array operation," *Journal of Microelectromechanical Systems*, vol. 11, pp. 765-774, 2002.

[21] W. P. King, "Design analysis of heated atomic force microscope cantilevers for nanotopography measurements," *Journal of Micromechanics and Microengineering*, vol. 15, pp. 2441-2448, 2005.

[22] F. P. Incropera and D. P. DeWitt, *Fundamentals of heat and mass transfer*, 4th ed., New York: Wiley, 2002.

# CHAPTER 7

# MEASUREMENTS OF MICROJET BREAKUP AND PHASE CHANGE CHARACTERISTICS USING MICROCANTILEVER SENSORS

## 7.1 Introduction

Microcantilever sensors have shown promising results for microjet flow characterization in terms of thrust, velocity, and cooling capacity in chapter 6. This chapter describes advancement of the microcantilever metrology for micro / nanojets regarding the measurement of jet breakup distance and boiling phenomena. New piezoresistive cantilevers have been used to detect two flow regimes before and after liquid microjet break up. Heated cantilevers investigated phase change characteristics associated with liquid microjet impingement on the resistive micro heater.

After a liquid jet is ejected from a nozzle into a quiescent ambient environment, the jet eventually breaks up into droplets. Figure 7.1 shows a microjet emanating from a micro nozzle and two flow regimes distinguished by the jet breakup. The distance from the nozzle exit to the position at which the jet starts to break is well known as the "breakup distance." Jet breakup phenomena have been studied theoretically and experimentally for more than a century since Rayleigh's early work on jet instability [1]. Most reported experimental approaches employed optical microscopy with a laser to measure jet flow. In one study, shadowgraphy was used to capture shadow images of the

jet instability and evolution in the laser sheet [2]. The jet breakup depending on the driving pressure was measured and the existence of multiple droplet frequencies was confirmed from the unequal streamwise droplet spacing [3]. More recently, a new technique was reported for the breakup visualization of high speed liquid microjets, in which a focused He-Ne laser was injected and coupled into a water microjet acting as a wave guide using total internal reflection [4]. Initially, the injected laser traveled through and was guided by the water jet, but it eventually scattered out near the breakup. A CCD camera captured this scattered light and this technique was referred to as "the light-guided method" [4].

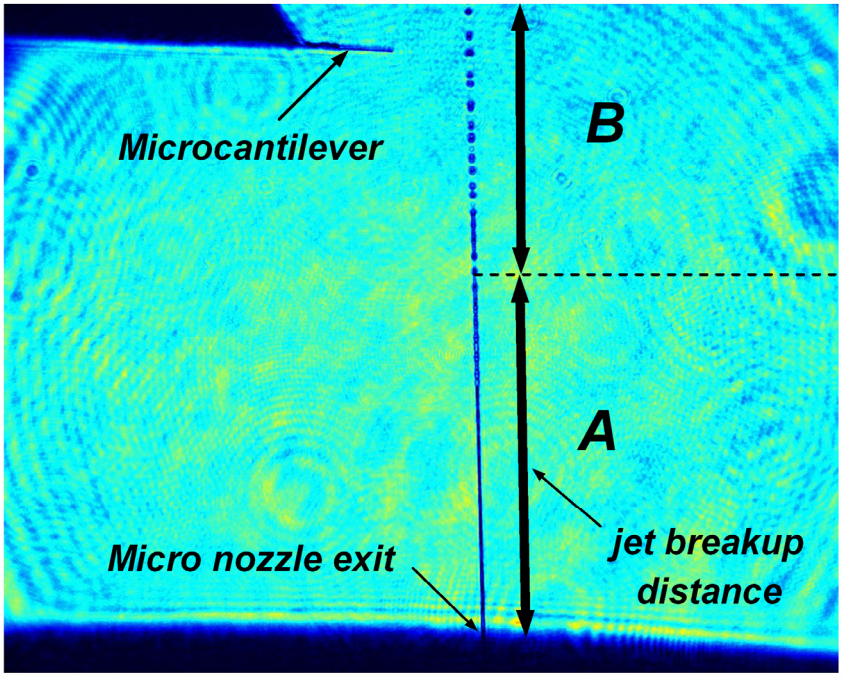


Figure 7.1 Shadowgraph image showing a microcantilever and a microjet emanating from a micromachined nozzle. '***A***' and '***B***' show two different flow regimes.

Optical methods are well-suited to investigate the jet instability and evolution from the nozzle exit and to the downstream. However, they require complex optics and extensive image processing. As an alternative approach, piezoresistive microcantilevers

are proposed to detect the microjet breakup distance since it is expected that the piezoresistive cantilevers show characteristic frequency responses before and after the microjet breaks up. While microcantilever measurements disrupt the fluid flow, they allow the measurement of jets that are too small to observe with diffraction-limited optical microscopy. Heated microcantilevers offer the additional capability of studying the boiling hysteresis associated with the microjet impingement on a micro heater.

## 7.2 Experimental Setup

The main components for the experiments were nearly identical to the setup described in chapter 6. Compared to the previous setup having three-axis microstages, a high pressure jet driving system, and a laser optical system, a real time spectrum analyzer (RSA3303A, Tektronix) was added to examine characteristic resonance excitation. A proportional-integral-differential (PID) control was constructed to control the heated cantilever resistance/temperature rather power/voltage using a data acquisition board which has both analog input and output (PCI-6052E, National Instruments). Heated cantilevers, as introduced in chapter 2, were interfaced with the PID control to investigate phase change characteristics upon microjet impingement. A second microcantilever having integrated piezoresistors was used to examine characteristic resonance excitation upon micro droplet impingement. The piezoresistive microcantilevers shown in Figure 7.2 were originally developed for bio/chemical sensing based on the induced surface stress upon analyte absorption. These cantilevers have simple geometry facilitating mechanical modeling and analysis. Most of all, the fabricated cantilevers show sensitive resistance changes to a point load excitation as well as a surface stress. Before the

experiments, mechanical characterization for the piezoresistive microcantilevers and thermal characterization for the heated microcantilevers were performed using characterization techniques reported in [5]. The characterized resonance frequencies and quality factors of the two piezoresistive cantilevers are summarized in Table 7.1.

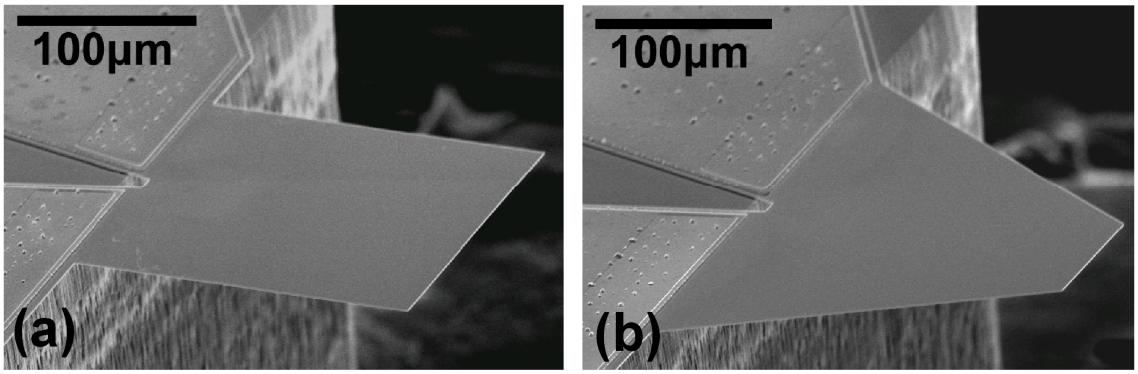


Figure 7.2. Scanning electron micrographs of (a) a square piezoresistive microcantilever and (b) a trapezoid piezoresistive microcantilever.

Table 7.1 Mechanical properties of the two piezoresistive cantilevers

| | Cantilever (a) | Cantilever (b) |
|---|---|---|
| $f_0$ (kHz) | 32.97 | 42.28 |
| $Q_0$ | 32.83 | 34.74 |

## 7.3 Results and Discussion

### 7.3.1 Breakup distance

The square piezoresistive cantilever was aligned to and impinged upon by a hexane ($C_6H_{14}$) microjet and the initial vertical position was referenced to the nozzle exit using the auxiliary laser optical system. The lateral position of the jet impingement was 150 μm from the cantilever base and this position was fixed during the measurement.

While the gap distance between the cantilever and the nozzle exit was varied, the spectrum analyzer output was recorded and analyzed.

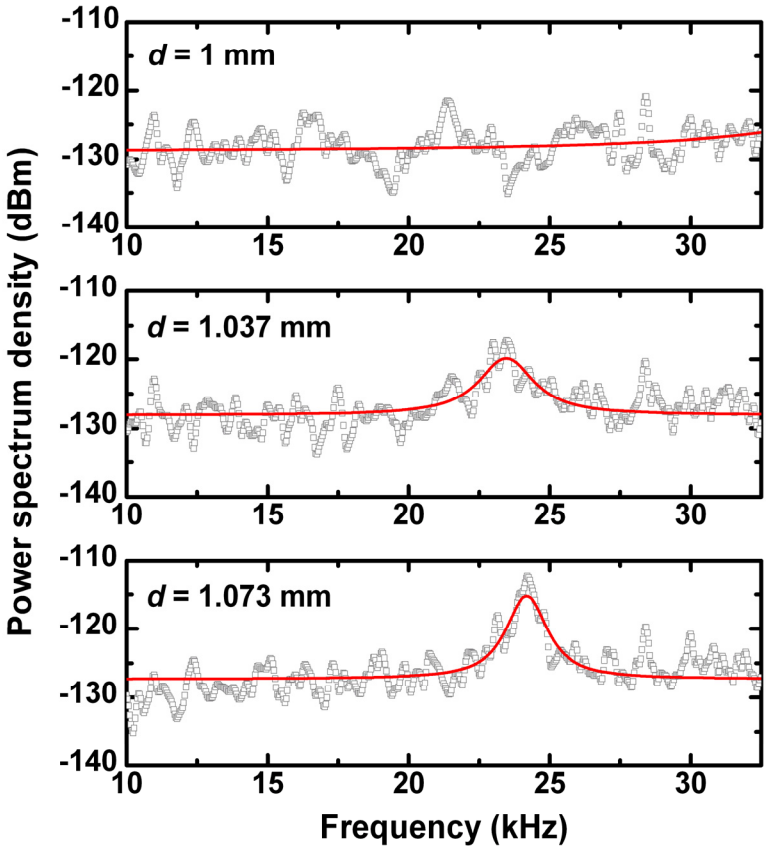


Figure 7.3. Power spectrum density from a real-time spectrum analyzer and corresponding Lorentzian curve fit at three different gap distances 1.000 mm, 1.037mm and 1.073 mm, respectively. The hexane jet velocity is 27 m/s.

Figure 7.3 shows the power spectrum densities (PSD) from the spectrum analyzer and corresponding Lorentzian curve fits at three different gap distances – 1.000 mm, 1.037 mm, and 1.073 mm, respectively. The hexane jet velocity is 27 m/s. When the gap distance is less than 1.037 mm, the fitted Lorentzian peak becomes less pronounced or negligible. When the gap distance is greater than 1.037 mm, the peak becomes intense enough to be observed. Therefore, it can be clearly seen that there are two different flow regimes from Figure 7.3. When the piezoresistive microcantilever is located close to the nozzle exit (region '***A***' in Figure 7.1), static deflection is dominant and any vibration will

be highly damped such that no observable peak exists in the frequency domain. However, when the cantilever is impinged on by discrete droplets (region '***B***' in Figure 7.1), the PSD shows a distinctive peak in the bandwidth of interest. Therefore, the breakup distance of the microjet can be determined by applying an appropriate threshold in the PSD.

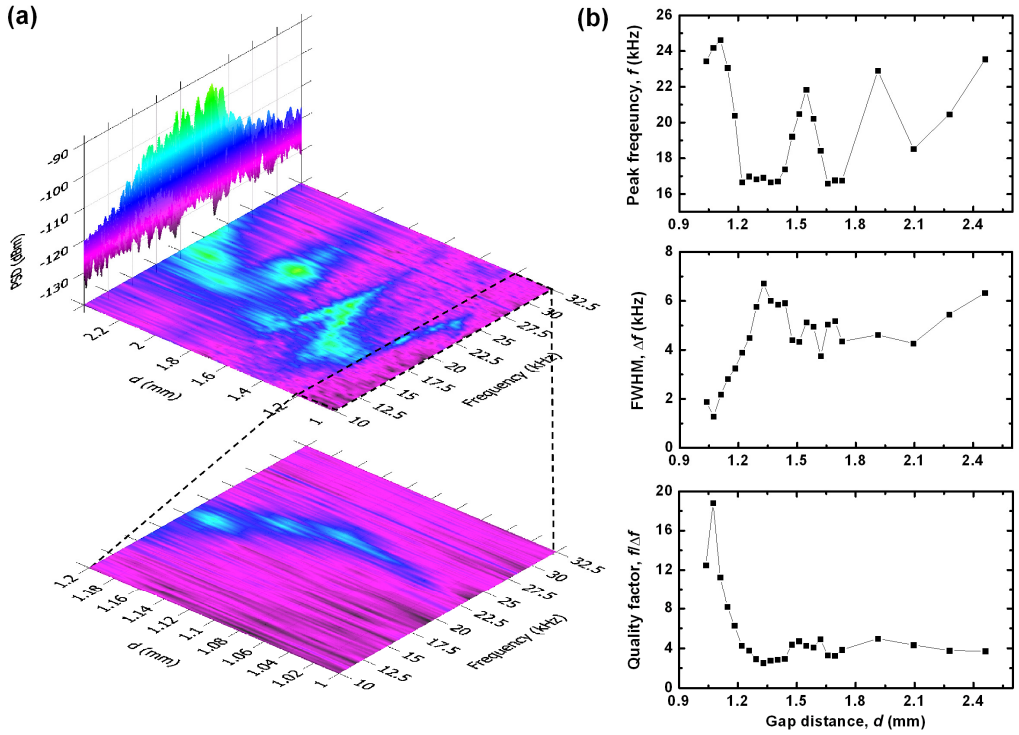


Figure 7.4. (a) Contour and projection plots showing characteristic behaviors in the frequency domain before and after jet breaks up into droplets. (b) Peak frequency, FWHM, and quality factor as a function of gap distance.

Figure 7.4(a) shows contour and projection plots of the PSD in a wide range of gap distances. The peak disappears around 1.03 mm which is the breakup distance. Figure 7.4(b) shows the peak frequency, FWHM, and quality factor as a function of the gap distance. The peak frequency changes periodically between 16 and 25 kHz in the direction of the jet flow. The shape of the peak characterized by the peak intensity and the quality factor also changes with the gap distance. The peak intensity also oscillates a

somewhat but shows a slight overall increase with the gap distance. The quality factor shows strong dependence on the gap distance or breakup. The quality factor becomes maximized around at 1.073 mm then decreases drastically and becomes insensitive to further gap change when the gap distance is greater than 1.073 mm. Figure 7.3 and Figure 7.4 show that both the peak intensity and the quality factor can be a measure of the microjet breakup.

The observed peak is expected to be the fundamental resonance frequency of the tested cantilever. Any frequency associated with the droplet impingement needs to be investigated. In the hexane jet impingement, the averaged droplet spacing was 37 um and jet velocity was 27 m/s. Thus, the calculated main droplet impinging frequency was approximately 730 kHz. Multiple frequency components can exist after jet breakup but they are expected to be near the main impinging frequency. Therefore, any frequency associated with the droplet is at least one order of magnitude larger than the observed characteristic peaks in the measurements. Moreover, the tested cantilever can not measure frequencies of that magnitude due to its much lower resonance frequency.

The droplet impingement can be modeled as a periodic impulse of which the Fourier transform is similar to white noise. Thus, droplet impingement actually excited the microcantilever while the cantilever vibration was damped by the possible liquid uptake after impingement. When the liquid stuck to the cantilever, it increased the effective mass of the oscillating system and changed the damping condition. These two effects combined modulated the resonance of the cantilever. Since liquid mass uptake and associated damping possibly depend on the position of jet impingement, this lateral position can change the measurement sensitivity.

Another experiment was performed using a different piezoresistive microcantilever as shown in Figure 7.2(b). Except for the cantilever type, all other conditions, mainly the jet driving pressure, were maintained to generate a hexane microjet with velocity and impinging frequency similar to the previous experiment. In addition, the gap distance was fixed at 2 mm from the nozzle exit and the microjet was aligned to the cantilever free end. The lateral position of the microcantilever was controlled within a few μm so that the liquid uptake during droplet impingement was modulated periodically over time. A video clip was recorded to examine the liquid mass uptake. Due to the difference in the cantilever shape and the lateral position of jet impingement, the characteristic peak is expected to be observed at a different frequency band.

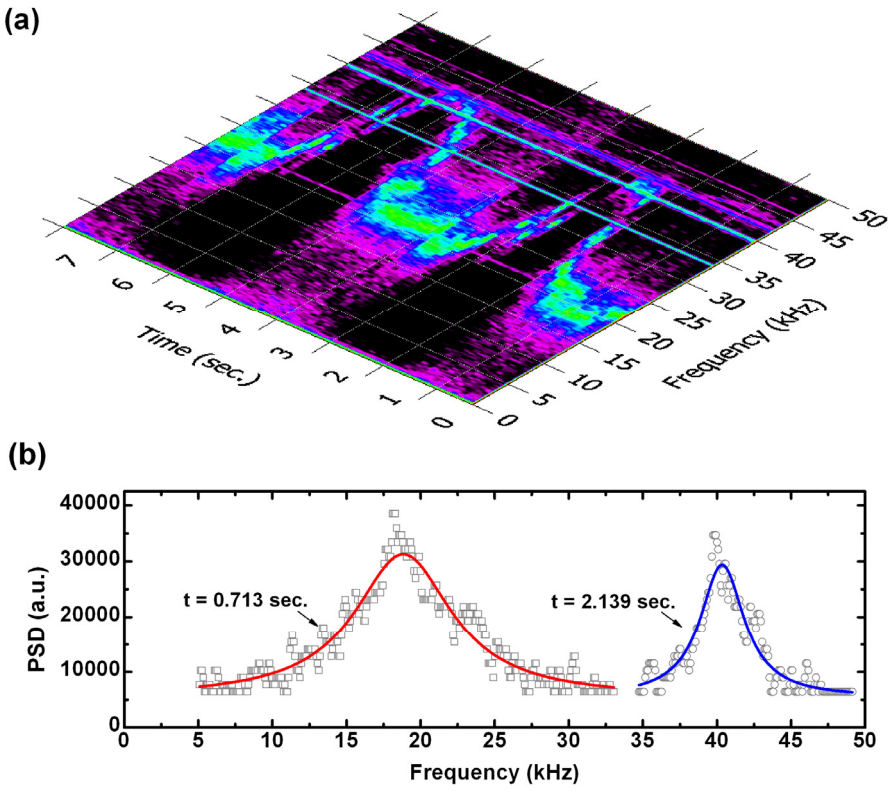


Figure 7.5 (a) Spectrogram of the frequency response for the piezoresistive microcantilever upon droplet impingement. (b) PSD from the Wheatstone bridge. The position of the microcantilever was controlled such that the liquid uptake during droplet impingement was modulated periodically over time.

Figure 7.5(a) shows the spectrogram of the frequency response for the piezoresistive microcantilever upon droplet impingement while the video clip captures changes in the liquid mass surrounding the microcantilever qualitatively. The characteristic peaks are observed between 18 and 41 kHz. When the peak frequency is low (~ 18 kHz), the video confirmed that a significant amount of the liquid hexane stuck to both sides of the cantilever. In contrast, when the peak frequency was high (~ 41 kHz), the amount of liquid hexane uptake was negligible. As more liquid covers the cantilever, the peak frequency decreases and its shape also gets wider since the liquid uptake increases the effective mass of the simple harmonic oscillator system and causes more damping as mentioned previously. Since the characteristic peak was modulated by the liquid mass uptake, the previously observed characteristic peaks were confirmed to be the fundamental resonance frequency of the microcantilever. Figure 7.5(b) clearly shows the modulated peak shape and shift at $t$ = 0.713 and $t$ = 2.139 sec. The corresponding peak frequencies are 18.83 and 40.35 kHz and the quality factors are 2.41 and 11.34, respectively. In contrast to the previous results using the square cantilever, there was an order of magnitude change in the quality factor even though the cantilever stayed at the discrete droplet impinging regime. This could be explained with the instantaneous liquid film thickness around the cantilever. Since the lateral position of the cantilever was changed in a periodic fashion, there was significant modulation in the amount of liquid on the cantilever. Only when the hexane jet barely hit the cantilever near the free end, the jet still excited the cantilever vibration with the damping greatly suppressed. As soon as the liquid stuck to the cantilever, the cantilever motion was highly damped.

### 7.3.2 Boiling hysteresis

To investigate cooling and phase change characteristics of microjets, a heated microcantilever was aligned to and impinged upon by a butane ($C_4H_{10}$) microjet having a velocity of 24 m/s. In chapter 6, cantilever power dissipation was monitored and recorded only while the input voltage was ramped up. In this chapter, cantilever power was measured during both heating and cooling cycles.

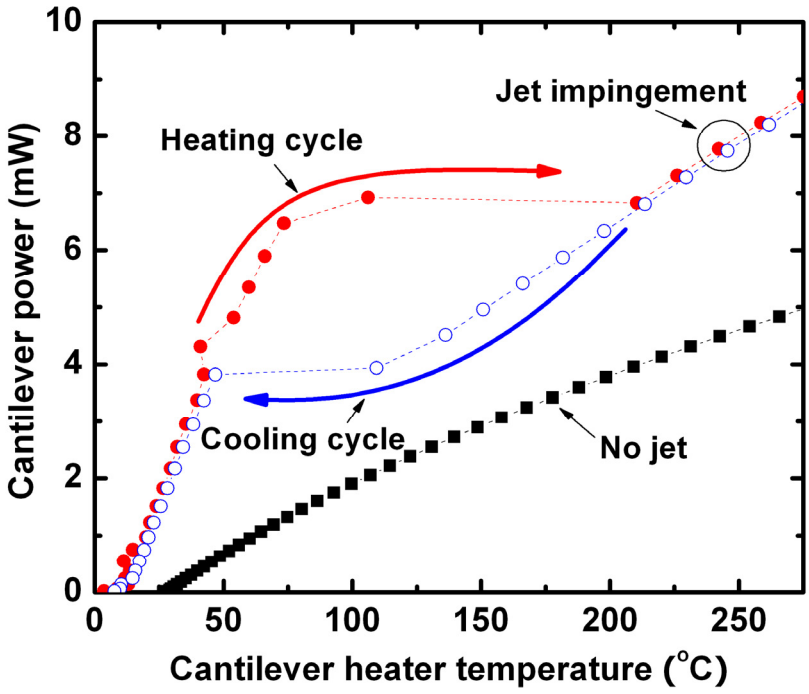


Figure 7.6. Cantilever power dissipation in ambient air and upon butane microjet impingement. Hysteresis exists during heating and cooling cycles. The butane jet velocity is 24 m/s.

Figure 7.6 shows the cantilever power dissipation during butane microjet impingement and also includes the power dissipation in ambient air for comparison. When the power dissipation was less than 4 mW or greater than 7 mW, heating and cooling curves were identical. In contrast, the heating and cooling curves started to deviate and showed hysteresis when the power dissipation ranges from 4 to 7 mW. Based on the similarity to the conventional boiling curve, the observed hysteresis is

possibly due to the boiling on the heater surface of the microcantilever. It should be noted that voltage or power rather than cantilever heater temperature were controlled herein. Therefore, temperature information inside the hysteresis loop could not be obtained. Due to this hysteresis loop, the heated cantilever can have different resistance and temperature at given power dissipation. In a voltage or power control mode, the cantilever temperature can change dramatically and the control system will become unstable.

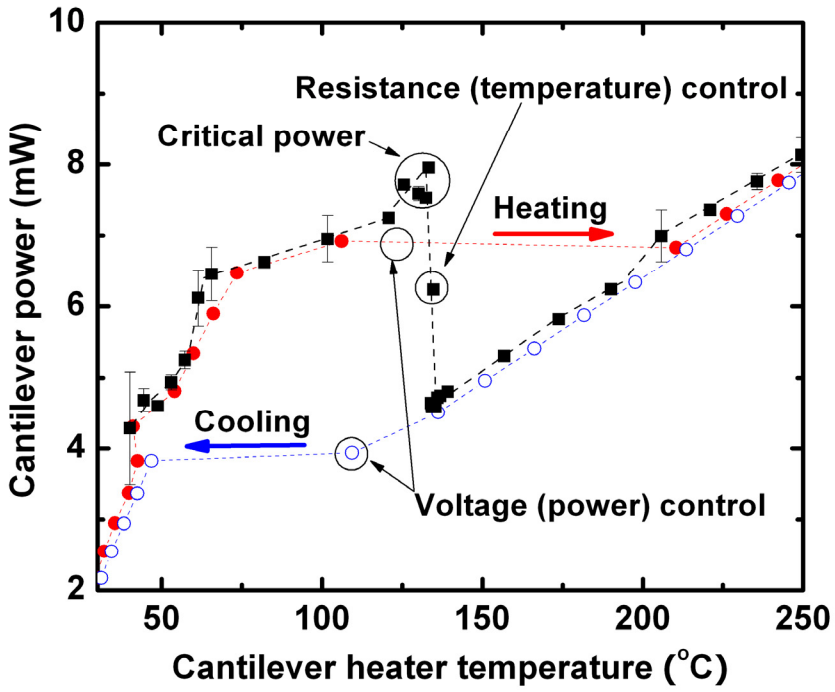


Figure 7.7. Boiling curve of the butane microjet impinging on the heated microcantilever constructed with a PID resistance (temperature) control.

To fully construct a boiling curve, a proportional-integral-derivative (PID) controller was interfaced with the heated cantilever and electrical resistance of the cantilever was controlled. Figure 7.7 shows the full boiling curve of the butane microjet impinging on the resistive heater of the microcantilever. Heating and cooling curves from Figure 7.6 are included for comparison. In conventional boiling curves, the excess

temperature, $\Delta T_e = T_s - T_{sat}$ , is usually given on the x-axis where $T_s$ is temperature of the heater surface and $T_{sat}$ is the saturation temperature at given pressure [6]. Due to the difficulty in measuring the temperature of the liquid microjet from a 10 μm diameter nozzle, cantilever heater temperature replaces excess temperature hereinafter. From this full boiling curve, the critical power and corresponding cantilever heater temperature were obtained. It should be noted that the transition from the nucleate boiling to the film boiling occurred within a few degrees change in the cantilever heater temperature. Without the PID control, the cantilever heater temperature suddenly increased beyond the critical power when the vapor blanket surrounded the cantilever heater completely. Microjet cooling will be very effective near the critical power before the sudden temperature jump.

### 7.3.3 Critical power and heat flux

Different hydrocarbon (Butane, Hexane, and Octane) microjets were tested, characterized, and compared in terms of critical power. Figure 7.8(a)-(c) show the cantilever power as a function of the cantilever heater temperature at various Reynolds (Re) numbers ranging from 570 to 1230. The power dissipation in ambient air is also shown for comparison. Both heating and cooling curves were taken at each *Re* number. Except for the hysteresis loop, the power dissipation in the cantilever is nearly identical in the heating and cooling cycles. For each hydrocarbon microjet, the cantilever power is somewhat less sensitive to the jet velocity and *Re* number at lower cantilever temperatures except for the hexane microjets, which showed deviating power dissipation at low temperatures. The anomaly of the hexane microjet is mainly attributed to the misalignment of the jet to the cantilever heater. However, increased *Re* number extends

the nucleate boiling regime and increases the critical power. After the transition from nucleate boiling to film boiling, higher power dissipation is observed at higher *Re* number since the heat transfer coefficient increases with *Re* number. At a given *Re* number, cantilever heater temperature corresponding to the boiling transition increases with the molecular weight of the hydrocarbon since heavier hydrocarbons (alkanes) have stronger dispersion forces which in turn increase boiling and melting points [7].

Liquid droplets or film were observed around the microcantilever legs when the cantilever heater temperature was low [8]. Heat transfer around the cantilever legs through this droplet or film is more dominant than heat transfer around the cantilever heater where the microjet impinges. This is due to the fact that phase change occurs on both the heater and the legs and that the surface area of the legs is much larger than that of the heater. The presence of a droplet or film which partially covers the cantilever legs complicates the heat transfer analysis in the nucleate boiling regime because it is difficult to predict how much of the area is covered by the liquid droplet or film. As the cantilever heater temperature increases, the size of the droplet or film decreases and it completely disappears at about the critical power. Therefore, the microjet impingement cooling only affects the cantilever heater around the critical power, at the transition, and in the film boiling regime. In those regimes, the cantilever legs will be exposed to the ambient air.

Measurements at *Re* number higher than 1000 for octane and 1300 for butane and hexane were not available since the microjet impingement deflected the cantilever significantly. A different cantilever orientation could be employed to decrease the impinging angle and minimize the cantilever deflection at a given *Re* number. Otherwise, stiffer cantilevers can be selected to prevent extreme bending.

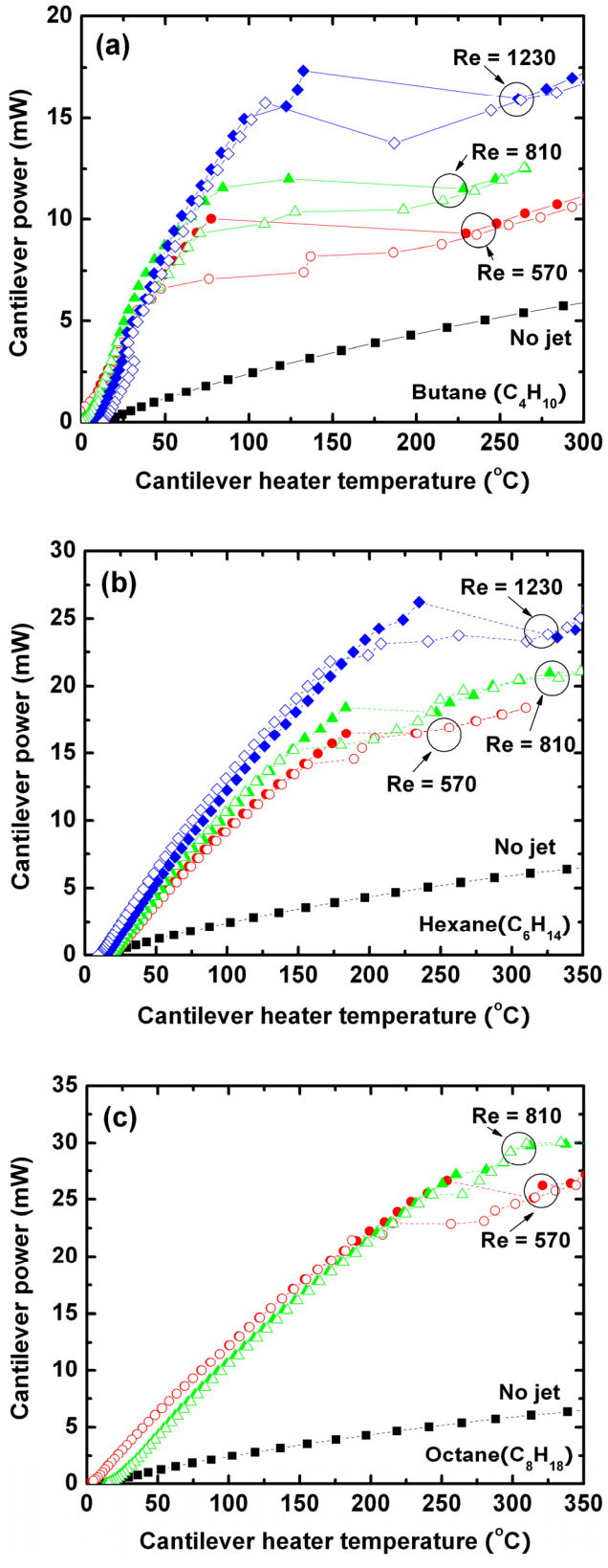


Figure 7.8. Boiling hystereses of (a) butane (b) hexane and (c) octane microjets.

To estimate the heat flux at the critical power (critical heat flux, CHF), a finite difference heat transfer simulation was performed considering temperature dependent thermal conductivity and electrical resistivity [9]. From the cantilever operation without jet impingement, the cantilever-air thermal conductance was extracted. In the actual simulation, the extracted cantilever-air conductance was used for the differential nodes that were not influenced by the microjet impingement and the cantilever-microjet conductance was used as a fitting parameter. The simulation calculated convective heat transfer from the cantilever heater to the microjet and heat fluxes were obtained based on the surface area of the heater.

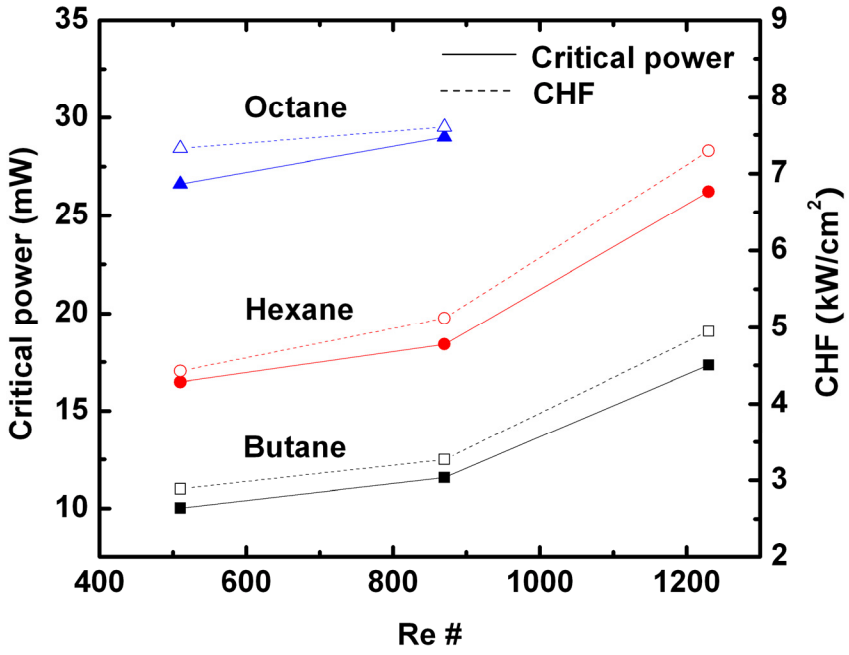


Figure 7.9 Measured critical power and simulated CHF as a function of *Re* number for three hydrocarbon microjets.

Figure 7.9 compares the measured critical power and simulated CHF for butane, hexane, and octane at different *Re* numbers. Both the critical power and CHF increase with *Re* number and octane microjets have the highest critical power and CHF at a given

*Re* number. Due to these similar trends, CHF can be estimated directly from the measured critical power.

## 7.4 Summary and Conclusions

Liquid butane, hexane, and octane microjets from a micromachined nozzle, 10 μm in diameter, have been characterized using microcantilever sensors. Piezoresistive microcantilevers have measured the breakup distance of a hexane microjet via resonance frequency responses excited by the droplet impingement after breakup. To the best of our knowledge, this is the first demonstration of microjet breakup distance detection using a MEMS mechanical sensor.

Heated microcantilevers have been used to study phase change characteristics during the microjet impingement on a micro heater near the cantilever free end. From our experiments, cooling characteristics of hydrocarbon microjets were observed along with the boiling hysteresis and critical power measurement. During successive heating and cooling cycles, a thermal hysteresis possibly indicating boiling phenomena was observed. To confirm this and obtain a full boiling curve, the cantilever was heated with constant temperature using a PID temperature control. The measurements were repeated and several hydrocarbons were compared at *Re* numbers ranging from 570 to 1230. Heat transfer simulations estimate critical heat fluxes by microjet impingement boiling to be between 2.9 and 7.6 $W/cm^2$.

In this chapter, the breakup and cooling characteristics of hydrocarbon microjets were investigated using microcantilever sensors. The new metrology methods discussed

in this chapter will be readily compatible to more common dielectric liquids for microelectronics cooling such as fluorocarbons (FCs) and hydro-fluoro-ethers (HFEs).

## 7.5 References


[1] J. W. S. Rayleigh, "On the instability of jets," *Proceedings of the London Mathematical Society*, vol. 10, pp. 4-13, 1879.

[2] J. B. Blaisot and S. Adeline, "Instabilities on a free falling jet under an internal flow breakup mode regime," *International Journal of Multiphase Flow*, vol. 29, pp. 629-653, 2003.

[3] N. Naik, C. Courcimault, H. Hunter, J. Berg, J. Lee, K. Naeli, T. Wright, M. Allen, O. Brand, A. Glezer, and W. King, "Microfludics for generation and characterization of liquid and gaseous micro- and nanojets," *Sensors and Actuators, A*, vol. 134, pp. 119-127, 2007.

[4] N. Vago, A. Spiegel, P. Couty, F. R. Wagner, and B. Richerzhagen, "New technique for high-speed microjet breakup analysis," *Experiments in Fluids* vol. 35, pp. 303-309, 2003.

[5] J. Lee, T. Beechem, T. L. Wright, B. A. Nelson, S. Graham, and W. P. King, "Electrical, thermal, and mechanical characterization of silicon microcantilever heaters," *Journal of Microelectromechanical Systems*, vol. 15, pp. 1644-1655, 2006.

[6] F. P. Incropera and D. P. DeWitt, *Fundamentals of heat and mass transfer*, 4th ed., New York: Wiley, 2002.

[7] L. G. Wade, *Organic chemistry*, 4th ed.: Prentice Hall, 1999.

[8] J. Lee, K. Naeli, H. Hunter, J. Berg, T. Wright, C. Courcimault, N. Naik, M. Allen, O. Brand, A. Glezer, and W. P. King, "Characterization of liquid and gaseous micro- and nanojets using microcantilever sensors," *Sensors and Actuators, A*, vol. 134, pp. 128-139, 2007.

[9] J. Lee, T. L. Wright, M. R. Abel, E. O. Sunden, A. Marchenkov, S. Graham, and W. P. King, "Thermal conduction from microcantilever heaters in partial vacuum," *Journal of Applied Physics*, vol. 101, pp. 014906, 2007.

# CHAPTER 8

# SUMMARY AND RECOMMENDATIONS

## 8.1 Summary

This work presented design, fabrication, characterization, and application of heated cantilevers, piezoresisitve cantilevers and hybrid types which have both heaters and piezoresistors. Major contributions of this work are as follows.

- Better understanding of heated cantilevers which extends their uses beyond thermomechanical data storage (Chapter 2)
- Development of new characterization techniques for microcantilever devices (Chapter 2, Chapter 4, and Chapter 6)
- Successful fabrication of unconventional micro hotplate cantilevers and small arrays of microcantilever heaters with integrated piezoresistors (Chapter 3 and Chapter 4)
- Novel engineering and scientific applications employing microcantilevers (Chapter 5, Chapter 6, and Chapter 7)

To characterize the heated cantilever heating, the cantilever electrical response was first examined with DC, square pulse, and AC excitation. Following basic electrical testing, thermal and mechanical behaviors of the cantilevers were investigated using Raman spectroscopy and commercial AFM. Raman spectroscopy simultaneously measured local temperature and stress in the heated cantilever with 1 μm resolution and

AFM investigated mechanical properties such as spring constant, resonance frequency, and quality factor and their dependence on electrothermal excitation. The detailed characterization of the heated cantilevers performed in electrical, thermal, and mechanical domains offers better understanding and facilitates further applications demanding strict requirements for precise temperature calibration and thermoelastic behavior.

Various designs for the cantilever type micro hotplate were suggested and fabricated to realize fast response time and uniform temperature. Parallel or series resistor networks made of doped silicon were employed to increase temperature uniformity by spreading heat generation and the major current carrying resistor was offset from the free end to improve response time by reducing thermal diffusion length. The fabricated microcantilever hotplates have shown time constants smaller than 1 ms and maximum operation temperatures greater than 1000 °C. Though none of the proposed designs were optimized, our comparative studies offer an important guideline for cantilever type micro hotplates made of silicon.

Following individual device fabrication and characterization, arrays of microcantilever heaters were designed and fabricated to meet strong requirements for improved speed and high throughput applications. In addition to array parallelization, a resistive heater and a piezoresistor were integrated into a microcantilever so that this cantilever array will be applicable to parallel SPL and force spectroscopy without incorporating laser and photo-detector array. The fabricated cantilever arrays showed improvement over previous designs by suppressing parasitic bending and preventing electromigration upon high temperature operation. In terms of characterization, thermal

and electrical cross-talks were of main interest. IR microscopy confirmed that the piezoresistor operation did not affect the heater temperature since the majority of input power was dissipated towards the silicon handle. In contrast, the heater operation, which often needs to be at high temperatures, increased the average temperature of the piezoresistor thus affecting the deflection sensitivity. Therefore, the effect of heating on the piezoresistor sensitivity was quantified using a custom built characterization setup and the results showed good agreement with the theoretical estimation. The deflection sensitivity of the resistive heater (mostly high doped legs) was also measured and the heater showed non-negligible deflection sensitivity. This possibly limits the sensitivity of the heater as a resistive thermometer but can be compensated by comparing the heater signal with the piezoresistor signal. Both the piezoresistive reading and the thermal reading for four cantilevers in a single array chip were performed simultaneously. Then, the sensitivites of the thermal and piezoresistive readings were measured and cross-talks between the two doped resistors in each cantilever were investigated. Overall, successful array integration of the micro heater and the piezoresistive sensor is the first step towards massive multifunctional microcantilever arrays.

Finally, novel metrology tools using the fabricated and characterized microcantilever sensors were demonstrated. First demonstration utilized heated cantilevers to measure heat transfer characteristics in a micro heater subject to a wide range of pressure variation. The results showed that the size of the micro heater modulated thermal conductance between the cantilever and its gaseous surroundings which is characterized by the Knudsen number, $Kn$. When $Kn < 1$, thermal transport from the cantilever heater depended upon the gas pressure, and when $Kn > 1$, thermal transport

from the cantilever heater remained constant. The change in the thermal conductance regime associated with a microcantilever heater could be universally described by the Knudsen number for different gas species. Our measurement of thermal conductance around $Kn = 1$ may aid the design of future micro Pirani and other thermal MEMS sensors.

The second demonstration employed both piezoresistive cantilevers and heated cantilevers for micro/nanojets characterization. Piezoresistive cantilevers measured jet thrust, velocity, and breakup of the liquid microjets and spray angle of the gaseous microjets. The measured microjet velocities extracted from the jet thrust showed good agreement with shadowgraphy results within 12.5%. Piezoresistive cantilever sensors investigated the effective flow field, estimated spray angle of the gaseous jet, and inspected nozzle clogging. Breakup distance of a microjet was also measured via resonance frequency responses excited by the droplet impingement after breakup. This was the first demonstration of a microjet breakup measurement using a MEMS mechanical sensor. Heated cantilevers mainly investigated phase change and cooling characteristics upon liquid jet impingement on the resistive heater. Cooling characteristics of hydrocarbon microjets were observed along with the boiling hysteresis and critical power measurement. During successive heating and cooling cycles, a thermal hysteresis possibly indicating boiling phenomena was observed. Measurements were repeated and compared for several hydrocarbons at *Re* numbers ranging from 570 to 1230. Heat transfer simulation estimates critical heat fluxes by microjet impingement boiling between 2.9 and 7.6 kW/cm$^2$. Our novel microcantilever metrology will be more

viable for further miniaturized jets where the diffraction limited optical techniques are not applicable.

## 8.2 Recommendations and Future Research

This work presented extensive understanding of fabrication, characterization, and application of a single microcantilever. However, more efforts are still required for microcantilever array devices. Major target applications of our multi-functional microcantilever arrays are parallel nanolithography on polymeric substrates and high throughput force spectroscopy on biological samples. These applications strongly demand improvements in fabrication, characterization, and system integration.

### 8.2.1 Fabrication

Two suggestions can be made in terms of fabrication. First, the fabricated multifunctional cantilevers can be empowered by integrating thermal bimorph actuation. The fabricated arrays have resistive heaters and deflection sensors but no actuation mechanism. Therefore, not all cantilevers may come into contact with a substrate of interest or may hover around without applying enough contact forces during SPM operation. Required contact forces are expected to be appreciably higher that those in normal contact mode scanning. Moreover, silicon is not a highly compliant material so that the life cycle of cantilever probe tips will be compromised. Once bimorph actuation is integrated on top of our multifunctional microcantilever array, each cantilever can be individually actuated and controlled. Bimorph actuation is suggested over piezoelectric actuation mainly because of the material selection and fabrication feasibility. Second, the

fabricated small 1D microcantilever arrays need to be expanded to larger 1D or 2D arrays. To realize massive microcantilever arrays, better fabrication process control is indispensable. Probe tip height and stress level in each microcantilever need to be well maintained. Improvements on previous fabrication steps are recommended and it is also important to select high quality materials and research alternative fabrication techniques if available. For instance, more uniform tips can be fabricated for large microcantilever arrays by wet chemical etching rather than dry plasma etching.

### 8.2.2 Array characterization

The larger the array size is, the more time for characterization is required. Therefore, cost and time effective ways to characterize array devices need to be developed along with the large array fabrication process. Among various characteristics, the deflection sensitivity and temperature sensitivity of the doped resistors are of great concern. When a cantilever array is brought into contact with a substrate, deflection and temperature sensitivity of both the piezoresistor and the heater in each cantilever can be measured simultaneously by moving the substrate located on top of a vertical piezo drive. To compensate tilt angle during the array engagement, a Wheatstone bridge having four piezoresistors from four cantilevers may be a possible solution. The voltage output from the constructed Wheatstone bridge can be monitored as a measure of tilt angle then manual or motorized goniometric stages can compensate tilt to achieve similar initial deflection for all cantilevers. In addition to static array characterization, the deflection and temperature sensitivity of all cantilevers can be characterized under a dynamic loading. AC voltage injected to the vertical piezo drive moves the substrate in a periodic

fashion which modulates the cantilever array in both the mechanical and the thermal domain. Cantilever arrays can be characterized during the dynamic modulation.

### 8.2.3 Feedback control

Most measurements using cantilevers as scanning probes in this work were assisted by the optical lever or performed without any feedback. Surface scanning without a feedback mechanism could result in serious wear of the probe tip and auxiliary optical lever prevents miniaturization of the AFM system. Since both the piezoresistor and the resistive heater can generate signals translating cantilever deflection or displacement, their signals can be used for a feedback loop. By the use of these new feedback mechanisms, compact and portable AFM systems can be realized. Once the aforementioned bimorph actuation is incorporated into all cantilevers of an array, each cantilever can be independently controlled without laser, photodiode, and vertical piezo drive.

# APPENDIX A

# FABRICATION PROCESS FOR MICRO HOTPLATE CANTILEVER

| | Process description | Material / equipment | Recipe |
|---|---|---|---|
| **1** | SOI wafer preparation | 4" SOI wafer <100> | 5 μm – 1μm – 500μm |
| **2** | Wafer thickness measurement | Nanospec 3000 refractometer | Check the thickness of the device layer and buried oxide |
| **3** | Device layer planarization | STS-ICP | m1_jay.prc<br>etch depth required = 1000 Å<br>Etch cycle = 3cycles |
| **4** | Wafer thickness measurement | Nanospec 3000 refractometer | Check the thickness of the device layer after ICP |
| **5** | PR spin coating | CEE 100CB spinner | Dehydration bake : 160 °C(oven)/ 5 min<br>Shipley 1813<br>2500 rpm – 500 rpm/sec – 33 sec<br>Soft bake : 115 °C (HP) / 3 min |
| **6** | Photolithography #1 (Mask 1) Define anchor and beam thickness | Karl Suss MA-6 Mask aligner | Exposure<br>Ch.2 (405 nm), Lo VAC, 20 μm separation<br>Dose= 120 mJ<br>Development<br>MF319 (1:20)<br>Post bake : 120 °C(HP) / 10 min |
| **7** | Define beam thickness | STS-ICP | m1_jay.prc<br>etch depth required = 2500 Å<br>Etch cycle = 8cycles |
| **8** | Wafer thickness measurement | Nanospec 3000 refractometer | Check the thickness of the device layer after ICP |
| **9** | Remove PR | Wet bench | $H_2SO_4$ : $H_2O_2$ = 7:3 in volume ratio<br>120 °C(HP) / 10 min |
| **10** | PR spin coating | CEE 100CB spinner | Dehydration bake : 160 °C(oven)/ 5 min<br>Shipley 1827<br>3000 rpm -500 rpm/sec – 35 sec<br>Soft bake : 115 °C(HP) / 3 min |

| | | | |
|---|---|---|---|
| **11** | Photolithography #2 (Mask 2) Define anchor and beam thickness | Karl Suss MA-6 Mask aligner | Exposure<br>Ch.2 (405 nm), LoVAC, 20 μm separation<br>Dose= 210 mJ<br>Development<br>MF354 (40 sec)<br>Post bake : 120 °C(HP) / 10 min |
| **12** | Define beam structure | STS-ICP | m1_jay.prc<br>etch depth required = 1500 Å<br>Etch cycle = 7cycles (over etch) |
| **13** | Remove PR | Wet bench | $H_2SO_4$ : $H_2O_2$ = 7:3<br>120 °C(HP) / 10 min |
| **14** | PR spin coating | CEE 100CB spinner | Dehydration bake : 160 °C(oven)/ 5 min<br>Shipley 1827<br>3000 rpm – 500 rpm/sec – 35 sec<br>Soft bake : 115 °C(HP) / 3 min |
| **15** | Photolithography #3 (Mask 3) PR masking for high dosage implantation | Karl Suss MA-6 Mask aligner | Exposure<br>Ch.2 (405 nm), LoVAC, 20 μm separation<br>Dose= 210 mJ<br>Development<br>MF354 (40 sec)<br>Post bake : 120 °C(HP) / 35 min |
| **16** | Implantation | Outside vendor CORE systems, CA | $2.51 \times 10^{16}$ atoms/$cm^3$, Phosphorus, 200 keV, 45 ° tilt,<br>Maximum current = 600 μA |
| **17** | Remove PR | Bransonic ultra sonic cleaner 5510,<br>Wet bench,<br>Gasonics Asher | Bransonic 5510, 20 min with acetone<br>$H_2SO_4$ : $H_2O_2$ = 7:3<br>120 °C(HP) / 10 min,<br>Asher, recipe A (1 min) |
| **18** | Covering doped area for diffusion | Unaxis PECVD | LJCSIO2.prc, 2 min 45 sec.<br>Deposited oxide thickness ~ 0.19 μm |
| **19** | Diffusion | Lindberg furnace tube 3 (oxidation) | 20 / 1000 / 2hrs / sleep / 25 / end |
| **20** | PR spin coating | CEE 100CB spinner | Dehydration bake : 160 °C(oven)/ 5 min<br>Shipley 1827<br>3000 rpm – 500 rpm/sec – 35 sec<br>Soft bake : 115 °C(HP) / 3 min |
| **21** | Photolithography #4 (Mask 4) Define via | Karl Suss MA-6 Mask aligner | Exposure<br>Ch.2 (405 nm), Hard, 20 μm separation<br>Dose= 210 mJ<br>Development<br>MF354 (40 sec)<br>Post bake : 120 °C(HP) / 10 min |

| | | | |
|---|---|---|---|
| **22** | Etch oxide to make via | Plasma Therm ICP | tlwsio2a.prc, 3.5 min (over etch) |
| **23** | Remove PR | Wet bench | $H_2SO_4$ : $H_2O_2$ = 7:3<br>120 °C(HP) / 10 min |
| **24** | PR spin coating | CEE 100CB spinner | Dehydration bake : 160 °C(oven)/ 5 min<br>Futurrex, NR5-8000<br>3000 rpm – 500 rpm/sec – 35 sec<br>150 °C(HP) / 1.5 min |
| **25** | Photolithography #5 (Mask 5) Metallization | Karl Suss MA-6 Mask aligner | Exposure<br>Ch.1 (365 nm), Hard, 20 μm separation<br>Dose= 700 mJ<br>Post exposure bake : 100 °C(HP)/ 2 min<br>Development<br>RD6 (50 sec) |
| **26** | Remove native oxide | Wet bench | BOE, 25 sec. |
| **26** | Metallization | CVC E-beam evaporator | Aluminum, 8000 Å, 3 Å/sec |
| **27** | Lift off | Wet bench | 1165, 80 °C (HP) / 1hr |
| **28** | Sintering | Lindberg furnace tube 4 (CMOS sintering) | Forming gas ~ 3<br>20 / 400 / 0.5 / sleep / 25 / end |
| **29** | PR spin coating | CEE 100CB spinner | Dehydration bake : 160 °C(oven)/ 5 min<br>Futurrex, NR5-8000<br>3000 rpm – 500 rpm/sec – 35 sec<br>Soft bake : 150 °C (HP) / 1.5 min |
| **30** | Photolithography #6 (Mask 6) Metallization | Karl Suss MA-6 Mask aligner, BSA | Exposure<br>Ch.1 (365 nm), Hard, 20 μm separation<br>Dose= 700 mJ<br>Post exposure bake : 100 °C(HP)/ 2 min<br>Development<br>RD6 / 1 min |
| **31** | Wafer cleaving | Diamond scribe | Cleave 4” wafer into 4 quadrants |
| **32** | Wafer mount on carrier wafer | CEE 100CB spinner, Single side polished wafer | Dehydration bake : 160 °C(oven)/ 5 min<br>Futurrex, NR5-8000<br>900 rpm – 200 rpm/sec – 40 sec<br>Attach the cleaved quadrant on the PR coated carrier wafer<br>Post bake : 120 °C(HP) / 25 min,<br>140 °C(HP) / 15 min |

| | | | |
|---|---|---|---|
| **33** | Backside thru wafer etch (ICP-DRIE) | Plasma Therm ICP | FTGSI2.prc, ~ 800 cycles |
| **34** | Detach a quadrant from the carrier wafer | Wet bench | 1165, 80 °C (HP) / overnight (at least 8 hrs) |
| **35** | Oxygen plasma clean | Plasma Therm RIE | HSHO2.prc / 30 min |
| **36** | Device release | Wet bench | HF, 15 ~ 25 sec. |

# APPENDIX B

# FABRICATION PROCESS FOR MICROCANTILEVER HEATERS ARRAY WITH INTEGRATED PIEZORESISTORS

| | Process description | Material / equipment | Recipe |
|---|---|---|---|
| **1** | SOI wafer preparation | 4" SOI wafer <100> | 5 μm – 1μm – 500μm |
| **2** | Wafer thickness measurement | Nanospec 3000 refractometer | Check the thickness of the device layer and buried oxide |
| **3** | Device layer planarization | Plasma Therm ICP | HJ_SI_02.prc (Etch B only), 40 sec |
| **4** | Wafer thickness measurement | Nanospec 3000 refractometer | Check the thickness of the device layer after ICP |
| **5** | PR spin coating | CEE 100CB spinner | Dehydration bake : 160 °C(oven)/ 5 min<br>Futurrex, NR7-1500<br>5000 rpm – 500 rpm/sec – 40 sec<br>Soft bake : 150 °C (HP) / 1 min |
| **6** | Photolithography #1 (Mask 1)<br>Tip fabrication | Karl Suss MA-6<br>Mask aligner | Exposure<br>Ch.1 (365 nm), Hard, 20 μm separation<br>Dose= 45 mJ<br>Post exposure bake : 100 °C(HP)/ 1 min<br>Development<br>RD6 (12 ~ 14 sec)<br>Hard bake : 120 °C(HP)/ 10 min |
| **7** | Tip fabrication | Plasma Therm ICP | HJ_SI_02.prc (Etch B only), 55 ~ 68 sec |
| **8** | Remove PR | Wet bench,<br>Gasonics Asher | Piranah, $H_2SO_4$ : $H_2O_2$ = 7:3<br>120 °C(HP) / 10 min,<br>Asher, recipe A (1 min) |
| **9** | Structure inspection | Hitachi 3500H SEM,<br>Tencor P-15 profilometer | Measure tip shape, width<br>Measure step height |
| **9** | Tip sharpening | Lindberg furnace tube 3 (oxidation) | Wet oxidation, $O_2$ flow rate = 8 L/min<br>20 / 1000 / 3hrs / sleep / 25 / end |
| **10** | Remove oxide | Wet bench | BOE, 5 min |

| | | | |
|---|---|---|---|
| **11** | Structure inspection | Hitachi 3500H SEM | Measure tip shape, width<br>Measure step height |
| **12** | Tip sharpening | Lindberg furnace tube 3 (oxidation) | Dry oxidation, $O_2$ flow rate = 8 L/min<br>20 / 1000 / 5hrs / sleep / 25 / end |
| **12** | Remove oxide | Wet bench | BOE, 2 ~ 3 min |
| **13** | Structure inspection | Hitachi 3500H SEM | Measure tip shape, width<br>Measure step height |
| **14** | PR spin coating | CEE 100CB spinner | Dehydration bake : 160 °C(oven)/ 5 min<br>Futurrex, NR5-8000<br>3000 rpm – 500 rpm/sec – 35 sec<br>Soft bake : 150 °C (HP) / 1.5 min |
| **15** | Photolithography #2 (Mask 2)<br>Define cantilever beam structure | Karl Suss MA-6<br>Mask aligner | Exposure<br>Ch.1 (365 nm), Hard, 20 μm separation<br>Dose= 170 mJ<br>Post exposure bake : 100 °C(HP)/ 2 min<br>Development<br>RD6 (50 sec)<br>Hard bake : 120 °C(HP)/ 10 min |
| **16** | Define cantilever beam structure | Plasma Therm ICP | JAY_SI.prc<br>Etch cycle = 15 ~ 16 cycles (over etch) |
| **17** | BOX layer thickness measurement | Nanospec 3000 refractometer | Check the thickness of the buried thermal oxide layer after ICP |
| **18** | Remove PR | Wet bench,<br>Gasonics Asher | 1165, 80 °C(HP) / 20 min<br>Asher, recipe A (1 min) |
| **19** | PR spin coating | CEE 100CB spinner | Dehydration bake : 160 °C(oven)/ 5 min<br>Shipley 1827<br>3000 rpm – 500 rpm/sec – 35 sec<br>Soft bake : 115 °C(HP) / 3 min |
| **20** | Photolithography #3 (Mask 3)<br>PR masking for low dosage implantation (heater) | Karl Suss MA-6<br>Mask aligner | Exposure<br>Ch.2 (405 nm), LoVAC, 20 μm separation<br>Dose= 210 mJ<br>Development<br>MF354 (40 sec)<br>Post bake : 120 °C(HP) / 35 min |
| **21** | Implantation | Outside vendor<br>CORE systems, CA | $2.51 \times 10^{13}$ atoms/cm$^3$, Phosphorus,<br>200 keV, offset 7 ° tilt,<br>current ≤40 μA |
| **22** | Remove PR | Bransonic ultra sonic cleaner 5510,<br>Wet bench, | Bransonic 5510, 10 min with acetone<br>Piranah, $H_2SO_4$ : $H_2O_2$ = 7:3<br>120 °C(HP) / 10 min, |

| | | | |
|---|---|---|---|
| | | Gasonics Asher | Asher, recipe A (1 min) |
| **23** | Covering doped area for diffusion | Unaxis PECVD | LJCSIO2.prc, 2 min 45 sec.<br>Deposited oxide thickness ~ 0.19 μm |
| **24** | Heater Diffusion | Lindberg furnace tube 3 (oxidation) | 20 / 1000 / 5.5hrs / sleep / 25 / end |
| **25** | Remove oxide | Wet bench | BOE, 2.5 min |
| **26** | PR spin coating | CEE 100CB spinner | Dehydration bake : 160 °C(oven)/ 5 min<br>Shipley 1827<br>3000 rpm – 500 rpm/sec – 35 sec<br>Soft bake : 115 °C(HP) / 3 min |
| **27** | Photolithography #4 (Mask 4)<br>PR masking for high dosage implantation (heater) | Karl Suss MA-6<br>Mask aligner | Exposure<br>Ch.2 (405 nm), LoVAC, 20 μm separation<br>Dose= 210 mJ<br>Development<br>MF354 (40 sec)<br>Post bake : 120 °C(HP) / 35 min |
| **28** | Implantation | Outside vendor<br>CORE systems, CA | $2.51 \times 10^{16}$ atoms/cm$^3$, Phosphorus,<br>200 keV, offset 7 ° tilt,<br>Maximum current = 600 μA |
| **29** | Remove PR | Bransonic ultra sonic cleaner 5510,<br>Wet bench,<br>Gasonics Asher | Bransonic 5510, 20 min with acetone<br>Piranah, $H_2SO_4$ : $H_2O_2$ = 7:3<br>120 °C(HP) / 10 min,<br>Asher, recipe A (1 min) |
| **30** | Covering doped area for diffusion | Unaxis PECVD | LJCSIO2.prc, 2 min 45 sec.<br>Deposited oxide thickness ~ 0.19 μm |
| **31** | Legs Diffusion | Lindberg furnace tube 3 (oxidation) | 20 / 1000 / 2hrs / sleep / 25 / end |
| **32** | Remove oxide | Wet bench | BOE, 2.5 min |
| **33** | PR spin coating | CEE 100CB spinner | Dehydration bake : 160 °C(oven)/ 5 min<br>Shipley 1827<br>3000 rpm – 500 rpm/sec – 35 sec<br>Soft bake : 115 °C(HP) / 3 min |
| **34** | Photolithography #5 (Mask 5)<br>PR masking for intermediate dosage implantation (piezoresistor) | Karl Suss MA-6<br>Mask aligner | Exposure<br>Ch.2 (405 nm), LoVAC, 20 μm separation<br>Dose= 210 mJ<br>Development<br>MF354 (40 sec)<br>Post bake : 120 °C(HP) / 35 min |

| | | | |
|---|---|---|---|
| **35** | Implantation | Outside vendor<br>CORE systems, CA | $2 \times 10^{14}$ atoms/cm$^3$, Boron<br>30 keV, offset 7 ° tilt |
| **36** | Remove PR | Bransonic ultra sonic cleaner 5510,<br>Wet bench,<br>Gasonics Asher | Bransonic 5510, 20 min with acetone<br>Piranah, $H_2SO_4$ : $H_2O_2$ = 7:3<br>120 °C(HP) / 10 min,<br>Asher, recipe A (1 min) |
| **37** | Covering doped area for diffusion | Unaxis PECVD | LJCSIO2.prc, 2 min 45 sec.<br>Deposited oxide thickness ~ 0.19 μm |
| **38** | Rapid thermal anneal | AET RTP | 1000 °C / 20 min |
| **39** | PR spin coating | CEE 100CB spinner | Dehydration bake : 160 °C(oven)/ 5 min<br>Shipley 1827<br>3000 rpm – 500 rpm/sec – 35 sec<br>Soft bake : 115 °C(HP) / 3 min |
| **40** | Photolithography #6 (Mask 6)<br>Define via | Karl Suss MA-6<br>Mask aligner | Exposure<br>Ch.2 (405 nm), Hard, 20 μm separation<br>Dose= 210 mJ<br>Development<br>MF354 (40 sec)<br>Post bake : 120 °C(HP) / 10 min |
| **41** | Etch oxide to make via | Plasma Therm ICP | tlwsio2a.prc, 3.5 min (over etch) |
| **42** | Remove PR | Wet bench | Piranah, $H_2SO_4$ : $H_2O_2$ = 7:3<br>120 °C(HP) / 10 min |
| **43** | PR spin coating | CEE 100CB spinner | Dehydration bake : 160 °C(oven)/ 5 min<br>Futurrex, NR5-8000<br>3000 rpm – 500 rpm/sec – 35 sec<br>Soft bake : 150 °C (HP) / 1.5 min |
| **44** | Photolithography #7 (Mask 7)<br>Metallization | Karl Suss MA-6<br>Mask aligner | Exposure<br>Ch.1 (365 nm), Hard, 20 μm separation<br>Dose= 700 mJ<br>Post exposure bake : 100 °C(HP)/ 2 min<br>Development<br>RD6 (50 sec) |
| **45** | Remove native oxide | Wet bench | BOE, 25 sec. |
| **46** | Metallization | CVC E-beam evaporator | Aluminum, 8000 Å, 3 Å/sec |
| **47** | Lift off | Wet bench | 1165, 80 °C (HP) / 1hr |
| **48** | Sintering | Lindberg furnace tube 4<br>(CMOS sintering) | Forming gas ~ 3<br>20 / 400 / 0.5 / sleep / 25 / end |

| | | | |
|---|---|---|---|
| **49** | PR spin coating | CEE 100CB spinner | Dehydration bake : 160 °C(oven)/ 5 min<br>Futurrex, NR5-8000<br>900 rpm – 200 rpm/sec – 40 sec<br>150 °C(HP) / 1.5 min |
| **50** | Photolithography #8 (Mask 8) Metallization | Karl Suss MA-6<br>Mask aligner, BSA | Exposure<br>Ch.1 (365 nm), Hard, 20 μm separation<br>Dose= 700 mJ<br>Post exposure bake : 100 °C(HP)/ 2 min<br>Development<br>RD6 / 1 min |
| **51** | Wafer cleaving | Diamond scribe | Cleave 4” wafer into 4 quadrants |
| **52** | Wafer mount on carrier wafer | CEE 100CB spinner,<br>Single side polished wafer | Dehydration bake : 160 °C(oven)/ 5 min<br>Futurrex, NR5-8000<br>900 rpm – 200 rpm/sec – 40 sec<br>Attach the cleaved quadrant on the PR coated carrier wafer<br>Post bake : 120 °C(HP) / 25 min,<br>140 °C(HP) / 15 min |
| **53** | Backside thru wafer etch (ICP-DRIE) | Plasma Therm ICP | FTGSI2.prc, ~ 800 cycles |
| **54** | Detach a quadrant from the carrier wafer | Wet bench | 1165, 80 °C (HP) /<br>overnight (at least 8 hrs) |
| **55** | Oxygen plasma clean | Plasma Therm RIE | HSHO2.prc / 30 min |
| **56** | Device release | Wet bench | HF, 15 ~ 25 sec. |